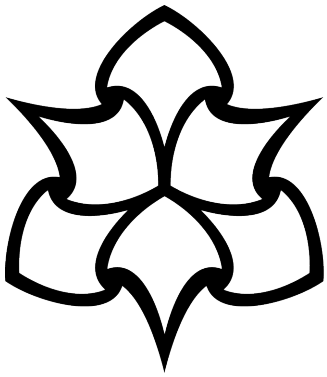

AUTOMATIC EXTRACTION OF RETINAL FEATURES TO ASSIST DIAGNOSIS OF GLAUCOMA DISEASE

MUHAMMAD SALMAN HALEEM

A thesis submitted in partial fulfillment of the requirements
of the
Manchester Metropolitan University for the degree of
Doctor of Philosophy

School of School of Computing, Mathematics and Digital Technology
the Manchester Metropolitan University
in collaboration with Optos plc

2015

Contents

Abstract i

Declaration iv

Copyright Statement v

Acknowledgements vi

1 Introduction 1

1.1 Background 1

1.2 Research Problems 2

1.3 Thesis Contributions 3

1.4 Thesis Outline 5

2 Glaucoma Disease and its Clinical Diagnosis 8

2.1 Introduction 8

2.2 Structure and Function of the Eye 8

2.3 Glaucoma and its Clinical Methods for Diagnosis 10

2.4 Glaucoma Assessment by Ophthalmoscopy 12

2.4.1 Fundus Camera 12

2.4.2 Scanning Laser Ophthalmoscopy 14

2.5 Retinal Symptoms of Glaucoma 14

2.5.1 Optic Nerve Head Variance 15

2.5.2 Neuroretinal Rim Loss 15

2.5.3 Vasculature Shift 16

2.5.4 Peripapillary Atrophy 17

2.6 Conclusion 17

3 Automatic Detection of Glaucoma Related Features - Survey 19

3.1 Introduction . . . 19

3.2 Segmentation based Automatic Feature Detection Methods . . . 20

3.2.1 Localization of ONH . . . 20

3.2.2 Optic Disc Extraction . . . 27

3.2.3 Optic Cup Extraction . . . 34

3.2.4 Peripapillary Atrophy . . . 36

3.3 Non-segmentation based Classification between Normal and Glaucomatous Retinal Images . . . 38

3.4 Automatic Retinal Disease Analysis on SLO Images . . . 39

3.5 Discussion and Conclusion . . . 40

4 Glaucoma Detection Framework - Rationale and Principles 42

4.1 Introduction . . . 42

4.2 Benchmark Retinal Image Database . . . 42

4.2.1 Pattern Recognition Lab, Erlangen Germany . . . 43

4.2.2 RIM-ONE (An Open Retinal Image Database for Optic Nerve Evaluation) . . . 45

4.2.3 Drishti-GS . . . 46

4.2.4 Optomaps . . . 46

4.3 The Glaucoma Detection Framework . . . 47

4.4 Analysis and Evaluation of the GDF . . . 48

4.4.1 Generation of Image-based Features . . . 49

4.4.2 Feature Selection Method . . . 54

4.4.3 Evaluation Metrics . . . 54

4.4.4 Machine Used for Experimentation . . . 55

4.5 Conclusion . . . 56

5 Retinal Image Pre-Processing 57

5.1 Introduction . . . 57

5.2 Retinal Area Detection . . . 57

5.2.1 Background . . . 59

5.2.2 Retinal Area Detection Method . . . 59

5.2.3 Gamma Adjustment 60
5.2.4 Generation of Superpixels 61
5.2.5 Ground Truth Determination 62
5.2.6 Feature Extraction 63
5.2.7 Feature Selection 64
5.2.8 Classifier Construction 68
5.2.9 Experimental Evaluation 69
5.3 The ONH Localization 72
5.3.1 Weighted Feature maps based ONH Localization Method 72
5.3.2 Ground Truth 74
5.3.3 Experimental Evaluation 75
5.4 Vasculature Segmentation 77
5.4.1 Ground Truth 77
5.4.2 Feature Generation and Selection 78
5.4.3 Experimental Evaluation 79
5.5 Conclusion 82

6 Optic Disc Segmentation **83**
6.1 Introduction 83
6.2 Ground Truth 84
6.3 Point Edge and Region Classification Model 85
6.3.1 Generation and Selection of Feature maps 86
6.3.2 Region Classification Model 89
6.3.3 Point Edge Modeling 91
6.3.4 The PERCM Algorithm 96
6.4 Experimental Evaluation 99
6.5 Conclusion 102

7 Optic Cup Segmentation **104**
7.1 Introduction 104
7.2 Ground Truth 104
7.3 Weighted Point Edge and Region Classification Model 105
7.3.1 Generation and Selection of Feature Maps 106

7.3.2 Region Force Calculation . . . 107
7.3.3 The WPERCM Algorithm . . . 111
7.4 Experimental Evaluation . . . 111
7.5 Conclusion . . . 113

8 Regional Image Features Model for Glaucoma Detection 115
8.1 Introduction . . . 115
8.2 Ground Truth . . . 116
8.3 Regional Image Features . . . 117
8.3.1 Feature Generation and Selection . . . 118
8.4 Experimental Evaluation . . . 120
8.5 Conclusion . . . 122

9 Diagnosis of Glaucoma 124
9.1 Introduction . . . 124
9.2 Automatic Determination of Clinical Indications of Glaucoma . . . 124
9.2.1 Cup to Disc Ratio . . . 124
9.2.2 Vasculature Shift . . . 127
9.2.3 Neuroretinal Rim Loss (ISNT Rule) Calculation . . . 127
9.3 Ground Truth . . . 129
9.4 Experimental Evaluation . . . 129
9.5 Conclusion . . . 130

10 Discussion and Conclusion 132

A Publications 137

B Academic Activities 139

Bibliography 141

List of Tables

3.1 Accuracy of several methods of optic disc detection / center localization 23
3.2 Results of different methods of optic disc extraction 29
3.3 Results of different methods of optic cup extraction 34
3.4 Results of different methods of the PPA localization / extraction 36
3.5 Results of different methods of non-segmentation based classification between normal and glaucomatous retinal images 38

4.1 Annotation of retinal image datasets 44
4.2 Inter-observer variability in the dataset 45
4.3 Inter-observer variability of optic disc and optic cup 46
4.4 Textural features extracted using GLCM 50
4.5 Gaussian based features 52
4.6 Regional features 53

5.1 Feature sets obtained usung different feature selection approaches. 'Feature Index' represents the order of highest independent evaluation criterion measure. 'Number of Selected Features' represent the sequence of feature selection in the feature set. R and G subscripts represent Red and Green channel respectively. The detail of feature symbols can be found in Section 4.4.1 67
5.2 Percentage of different types of features across different feature set . . 67
5.3 Comparison of framework output performance using different classifiers. The performance is compared with respect to computational time taken during training and testing and average accuracy. The training time is calculated for 28 images. Testing time shows the average time taken by the framework 71

5.4 Accuracy and execution time of ONH localization in different datasets . 75
5.5 Feature sets obtained using SFS approach for vasculature segmentation. The detail of feature symbols can be found in Section 4.4.1 79
5.6 Accuracy and execution time of vasculature segmentation in different datasets. 80

6.1 Feature symbols for each feature set obtained using the SFS and Filter approaches for optic disc region determination. The detail of feature symbols can be found in Section 4.4.1 87
6.2 Comparison of results of PERCM among different experts and mean of annotation of all experts 99
6.3 Comparison of results of PERCM with freeform and statistical shape models 100
6.4 Comparison of results of PERCM with freeform and statistical shape models in terms of healthy and glaucomatous images 100

7.1 Feature sets obtained using the SFS and Filter approaches for optic cup region determination. The detail of feature symbols can be found in Section 4.4.1. 106
7.2 Optic cup segmentation performance comparison in Drishti-GS by WPERCM across different experts and mean of annotations of all experts 112
7.3 Comparison of results of the WPERCM with freeform and statistical shape models. The results show the accuracy in terms of dice coefficient 112

8.1 Feature sets obtained using the SFS approach for classification between normal and glaucomatous images 120
8.2 Comparison of the results of regional image feature set with other feature sets 122
8.3 Comparison of the results of different classifiers on the RIF set 122

9.1 Mean(μ) and standard deviation(σ) of horizontal and vertical CDR of both normal and glaucoma images 126
9.2 Mean(μ) and standard deviation(σ) of vasculature shift of both normal and glaucoma images 128

9.3 Classification power of the features used for glaucoma diagnosis 131

List of Figures

2.1 Cross-sectional view of human eye [2] 9

2.2 The retinal image with labeled retinal structures 10

2.3 Normal vision vs glaucoma vision [5] 11

2.4 Tonometry as clinical example to suspect glaucoma using IOP [5] . . . 11

2.5 Example of (a) fundus image and (b) fundus camera [7] 13

2.6 Example of (a) SLO image and (b) SLO device from Optos [8] 13

2.7 Comparison of CDR in (a) normal image and (b) glaucoma image [1]. The glaucoma image has higher CDR 16

2.8 Clinical assessment based on the ISNT rule obtained from normal optic nerves. I,S,N and T represent inferior, superior, nasal and temporal regions respectively. The image is taken from the right eye 16

2.9 Comparison of vasculature shift in (a) normal image and (b) glaucoma image. The glaucoma image has vasculature shifted towards nasal area 17

2.10 PPA with α-zone and β-zone [125]. β-zone occurs more frequently in the temporal region of the right eye 18

3.1 A hierarchy of methodologies for automatic feature extraction from digital retinal images 20

3.2 Example of optic disc localization as brightest region (a) fundus image (b) determination of 2% brightest region and (c) optic disc localization [54, 131] 21

3.3 Example of optic disc localization using template matching (a) fundus image (b) optic disc localization (c) the template [54, 79] 22

3.4 Example of optic disc localization using vasculature convergence point detection (a) fundus image (b) detection of vasculature convergence point (c) optic disc localization [60] 26

3.5 Example of optic disc segmentation using morphological operation (a) fundus image (b) optic disc segmentation (c) optic disc segmentation [99] 28

3.6 Example of PPA extraction [97, 98] 37

4.1 Examples of retinal images from each dataset (a) Pattern Recognition Lab, Erlangen(b) Drishti-GS (c) RIM-ONE and (d) Optomaps. RIM-ONE is the only dataset with the ONH images 43

4.2 Examples of ground truth from (a) Pattern Recognition Lab, Erlangen on vasculature area (b) RIM-ONE around optic disc (c) Drishti-GS around optic disc and (d) Drishti-GS around optic cup. The annotation with different colours represent the annotations from differennt experts. 44

4.3 Block diagram of the Glaucoma Detection Framework (GDF) 48

4.4 (a) GLCM directions and offset (b) GLCM process using image **I** [57]. 51

5.1 An example of (a) a fundus image and (b) an SLO image annotated with true retinal area and the ONH 58

5.2 Block diagram of retina detector framework 60

5.3 Retinal image divided into superpixels 62

5.4 Determination of ground truth using superpixels and clinical annotations 63

5.5 (a) Receiver Operating Characteristics on the test sets (b) magnified version of (a) 65

5.6 (a),(b) Plot of independent evaluation criterion. The axis of 'Feature Index' in Figure. 5.6 (a) and (b) is ordered according to descending independent evaluation criterion. The features represented by 'Feature Index' and 'Number of Selected Features' are shown in Table 5.1. The features are ranked in descending order of independent evaluation criterion value. (a) shows Red dots for 'Filter and SFS approach' represent the 10 features selected by applying SFS on 'Filter approach' set. By applying the SFS on complete feature set, 10 out of 295 features have been selected as shown in (b) 'SFS approach'. (c) shows plot of increasing classification power (AUC) value by selecting the features one by one in different feature set. The axis of 'Number of Selected Features' in Figure. 5.6 (c) represents the order with which the features are selected using the SFS approach. 66

5.7 Artificial Neural Networks Diagram 69

5.8 Superpixel classification result of two examples of the SLO images. Columns represent different examples of retinal images. Left column are retinal scans with lesions whereas right column is the retinal scan from healthy subject. Figures (a) to (b) represent superpixel classification results and Figures (c) to (d) represent the final output 70

5.9 Block diagram of deployment stage of retinal area detector alongwith execution time of each block 70

5.10 An example of retinal area detection with higher visibility of eyelids . . 72

5.11 Examples of both feature maps with respective sliders. The feature maps have been enhanced by pixelwise multiplication with matched filter map and FRS transform map. 75

5.12 Fundus image ONH localization example with slider profile 76

5.13 SLO image ONH localization example with slider profile 76

5.14 Results of feature selection procedure with (a) Area Under the Curve of Fundus Images and the SLO images and (b) SFS feature selection procedure. The x-axis symbols are shown in Table 5.5 78

5.15 Examples of segmentation results on fundus images and the SLO images. (a) glaucoma fundus image from RIMONE with PPA around it, (b) segmented output of (a), (c) normal fundus image from RIMONE, (d) segmented output of (c), (e) the SLO image and (f) segmented output of (e) 81

6.1 Block diagram of Point Edge and Region Classification Model for optic disc segmentation 85

6.2 Results of feature selection procedures with (a) ROC curves of both fundus and SLO images for selected features using the SFS, (b) feature selection process using the SFS (c),(d) IEP of both fundus and SLO images respectively 88

6.3 Profile sampling for region determination 89

6.4 Alignment procedure of the optic disc shapes. The shapes are represented (a) in an original image, (b) after translation to the origin, (c) after normalization and (d) after flipping the annotations of left eyes so that the annotation direction of both the eyes would be same 93

6.5 Comparison of GVF and KVF in calculating force field where, (a) colour fundus image, (b) binary edge map obtained using Canny edge detector, (c) force field using KVF and (d) shows force field using GVF. The comparison of (c) and (d) shows f_{kvf} is not misguided by false edge within the optic disc as in case of f_{gvf} in (d). 95

6.6 Examples of optic disc determination (a),(b) are examples from Drishti-GS database, (c),(d) are examples from RIM-ONE and (e),(f) are examples from Optomaps. The red outline shows the original annotation around optic disc whereas the green outline shows the automatic annotations from the PERCM 101

6.7 Visual comparison of the PERCM with other models which were applied on the ONH images with PPA. The images show the result of (a) **PERCM**, (b) ASM, (c) Chan-Vese model and (d) GVF snake contour 102

7.1 Block diagram of the Weighted Point Edge and Region Classification Model for optic cup segmentation 105

7.2 Results of feature selection procedures with (a) ROC curves of both fundus and the SLO images for selected features using the SFS, (b) feature selection process using the SFS (c),(d) IEP of both fundus and the SLO images respectively 107

7.3 An example of determination of classification map and force calculation with (a) original image, (b) classification map of the neural weights, (c) pixels with neural membership value greater than 90%. (d) and (e) shows the comparison of force field calculated for optic cup of (d) feature maps and (e) feature maps multiplied by neural weights. The feature maps multiplied by neural weights have stronger force field around optic cup 109

7.4 Examples of optic cup determination with red outline is the benchmark and blue outline is the automatic annotation. (a),(b) are the examples from Drishti-GS database and (c),(d) are the examples from Optomaps 113

7.5 Visual comparison of WPERCM with other models which were applied for optic cup segmentation. The images show the result of (a) WPERCM, (b) Chan-Vese model and (c) ASM. Red outline is the benchmark and blue outline is the automatic annotation 114

8.1 Comparison of the ONH area of the (a) normal and (b) glaucomatous image. The difference is in terms of higher CDR and PPA indication . 116

8.2 Different regions of the ONH centred image with (a) image of a left eye (b) image divided into different quadrants with the ONH boundary represented with green and centroid with blue colour, (c) vasculature area within the ONH with higher area on the left side (d) ONH centred image divided into different regions 118

8.3 Results of regional image feature selection procedures for classification between normal and glaucomatous images with (a) ROC curves of both fundus and the SLO images for selected features using the SFS and (b) feature selection process using the SFS 120

8.4 Comparison of ROC curves of different feature sets in fundus and the SLO images 121

9.1 Comparison of the cup size with respect to the disc in (a) normal image and (b) glaucoma image. Both optic disc and optic cup boundaries have been automatically obtained by our proposed methods in Chapter 6 and 7. 125
9.2 Comparison of CDR histogram plots between normal and glaucoma images in RIM-ONE and Optomaps (SLO images) with blue representing normal and red representing glaucoma. (a) Vertical CDR and (b) horizontal CDR comparison on RIM-ONE and (c) vertical CDR and (d) horizontal CDR comparison on Optomaps. 126
9.3 Comparison of the vasculature shift in (a) right eye normal image and (b) right eye glaucoma image (c) left eye normal image and (b) left eye glaucoma image. In glaucoma images, the vasculature bundle is shifted towards the N region. Green asterisks represent the centroid of the vasculatrue bundle in I, S and N regions whereas yellow plus sign represent optic cup border point in T region farthest from the ONH center. Noting that N and T regions are at right and left side respectively in case of right eye image. These regions swap their places in case of left eye. 128
9.4 Comparison of vasculature shift histogram plots between normal and glaucoma images in RIM-ONE and Optomaps (SLO images) with blue representing normal and red representing glaucoma. (a) comparison on RIM-ONE and (b) comparison on Optomaps. 129
9.5 Comparison of proposed feature set with different clinical indications of glaucoma and Regional Image Features (RIF) classification results. The comparison has been performed on (a) RIM-ONE and (b) Optomaps 130

Abstract

Glaucoma is a group of eye diseases that have common traits such as high eye pressure, damage to the Optic Nerve Head (ONH) and gradual vision loss. It affects the peripheral vision and eventually leads to blindness if left untreated. The current common methods of diagnosis of glaucoma are performed manually by the clinicians. Clinicians perform manual image operations such as change of contrast, zooming in zooming out etc to observe glaucoma related clinical indications. This type of diagnostic process is time consuming and subjective. With the advancement of image and vision computing, by automating steps in the diagnostic process, more patients can be screened and early treatment can be provided to prevent any or further loss of vision.

The aim of this work is to develop a system called Glaucoma Detection Framework (GDF), which can automatically determine changes in retinal structures and image-based pattern associated with glaucoma so as to assist the eye clinicians for glaucoma diagnosis in a timely and effective manner. In this work, several major contributions have been made towards the development of the automatic GDF consisting of the stages of preprocessing, optic disc and cup segmentation and regional image feature methods for classification between glaucoma and normal images.

Firstly, in the preprocessing step, a retinal area detector based on superpixel classification model has been developed in order to automatically determine true retinal area from a Scanning Laser Ophthalmoscope (SLO) image. The retinal area detector can automatically extract artefacts out from the SLO image while preserving the computational efficiency and avoiding over-segmentation of the artefacts. Localization of the ONH is one of the important steps towards the glaucoma analysis. A new weighted feature map approach has been proposed, which can enhance the region of ONH for accurate localization. For determining vasculature shift, which is one of glaucoma indications, we proposed the ONH cropped image based vasculature classification model to segment out the vasculature from the ONH cropped image. The ONH cropped

image based vasculature classification model is developed in order to avoid misidentification of optic disc boundary and Peripapillary Atrophy (PPA) around the ONH of being a part of the vasculature area.

Secondly, for automatic determination of optic disc and optic cup boundaries, a Point Edge Model (PEM), a Weighted Point Edge Model (WPEM) and a Region Classification Model (RCM) have been proposed. The RCM initially determines the optic disc region using the set of feature maps most suitable for the region classification whereas the PEM updates the contour using the force field of the feature maps with strong edge profile. The combination of PEM and RCM entitled *Point Edge and Region Classification Model* (PERCM) has significantly increased the accuracy of optic disc segmentation with respect to clinical annotations around optic disc. On the other hand, the WPEM determines the force field using the weighted feature maps calculated by the RCM for optic cup in order to enhance the optic cup region compared to rim area in the ONH. The combination of WPEM and RCM entitled *Weighted Point Edge and Region Classification Model* (WPERCM) can significantly enhance the accuracy of optic cup segmentation.

Thirdly, this work proposes a Regional Image Features Model (RIFM) which can automatically perform classification between normal and glaucoma images on the basis of regional information. Different from the existing methods focusing on global features information only, our approach after optic disc localization and segmentation can automatically divide an image into five regions (i.e. optic disc or Optic Nerve Head (ONH) area, inferior (I), superior(S), nasal(N) and temporal(T)). These regions are usually used for diagnosis of glaucoma by clinicians through visual observation only. It then extracts image-based information such as textural, spatial and frequency based information so as to distinguish between normal and glaucoma images. The method provides a new way to identify glaucoma symptoms without determining any geometrical measurement associated with clinical indications glaucoma.

Finally, we have accommodated clinical indications of glaucoma including the CDR, vasculature shift and neuroretinal rim loss with the RIFM classification and performed automatic classification between normal and glaucoma images. Since based on the clinical literature, no geometrical measurement is the guaranteed sign of glaucoma, the accommodation of the RIFM classification results with clinical indications of glaucoma

can lead to more accurate classification between normal and glaucoma images. The proposed methods in this work have been tested against retinal image databases of 208 fundus images and 102 Scanning Laser Ophthalmoscope (SLO) images. These databases have been annotated by the clinicians around different anatomical structures associated with glaucoma as well as annotated with healthy or glaucomatous images. In fundus images, ONH cropped images have resolution varying from 300 to 900 whereas in SLO images, the resolution is 341 x 341. The accuracy of classification between normal and glaucoma images on fundus images and the SLO images is 94.93% and 98.03% respectively.

Declaration

No portion of the work referred to in the thesis has been submitted in support of an application for another degree or qualification of this or any other university or other institute of learning.

Copyright Statement

i. The author of this thesis (including any appendices and/or schedules to this thesis) owns certain copyright or related rights in it (the "Copyright") and s/he has given Manchester Metropolitan University certain rights to use such Copyright, including for administrative purposes.

ii. Copies of this thesis, either in full or in extracts and whether in hard or electronic copy, may be made **only** in accordance with the Copyright, Designs and Patents Act 1988 (as amended) and regulations issued under it or, where appropriate, in accordance with licensing agreements which the University has from time to time. This page must form part of any such copies made.

iii. The ownership of certain Copyright, patents, designs, trade marks and other intellectual property (the "Intellectual Property") and any reproductions of copyright works in the thesis, for example graphs and tables ("Reproductions"), which may be described in this thesis, may not be owned by the author and may be owned by third parties. Such Intellectual Property and Reproductions cannot and must not be made available for use without the prior written permission of the owner(s) of the relevant Intellectual Property and/or Reproductions.

iv. Further information on the conditions under which disclosure, publication and commercialisation of this thesis, the Copyright and any Intellectual Property and/or Reproductions described in it may take place is available in the University IP Policy (see http://www.celt.mmu.ac.uk/resources/copyright.php), in any relevant Thesis restriction declarations deposited in the University Library, The University Library's regulations (see http://libguides.mmu.ac.uk/content.php?pid=539980&sid=4442183) and in The University's Policy on Presentation of Theses.

Acknowledgements

I would like to express my sincere gratitude and appreciation to my director of studies, Dr. Liangxiu Han, for her sustained support throughout the research. Her enthusiasm, insight and guidance were invaluable assets which encouraged me to proceed well throughout the thesis.

I would also like to thank co-supervisor, Dr. Jano van Hemert from Optos by virtue of whom we were able to get the retinal scans from the company which were annotated by the clinicians. I would also like to thank Dr. Alan Fleming from Optos and my ex-co-supervisor, Dr. Baihua Li whose technical guidance during the entire thesis was a valuable asset. I want to thank all of the above for constructive comments during writing the publications and the thesis.

I would also like to thank my honorable parents for their unlimited love, support, and their encouragement which is the key factor in any achievement I have ever made. I would like to thank my friends, lab mates for the inspiring work environment. Special thanks to Jose for proof reading the thesis and Jasim, Ezak and Choon-Ching Ng for the fruitful discussions and the badminton games.

Finally, but not the least, I would like to thank the funding bodies i.e. Engineering and Physical Sciences Research Council (EPSRC) and Optos plc for providing me the studenship and the financial support to carry out the research work.

Above all, I thank God for giving me the perseverance required to ensure that the work I started was completed.

Chapter 1

Introduction

1.1 Background

According to the World Health Organization, 285 million people are estimated to be visually impaired worldwide and half of them are affected by the retinal diseases [110]. These rates are expected to double by year 2020 unless prevention efforts intensify. Since the vision loss has a significant impact on life, therefore early detection and treatment of eye diseases is critical to avoid vision loss. Some of the most common retinal diseases are irrevocable but early diagnosis and subsequent treatment at their earliest stages can prevent blindness. Conventionally, retinal disease identification techniques are based on manual observations from the imaging modalities used to observe the retina. Optometrists and ophthalmologists often rely on image operations such as change of contrast and zooming to interpret these images and diagnose results based on their own experience and domain knowledge. Such type of diagnostic techniques are time consuming and sometimes invasive.

With the advancement of digital imaging techniques, digital retinal imaging has become a promising and effective technology to identify patients with retinal diseases in primary care [133]. Imaging modalities to obtain retinal scan such as fundus camera or Scanning Laser Ophthalmoscope (SLO) have been widely used by the eye clinicians. Retinal imaging with automatic or semi-automatic image analysis algorithms can provide a great potential to cope with challenges associated with the diagnostic process [63, 103]. The automated analysis of the retinal images has the potential to reduce the time which clinicians need to look at the images which implies that more

patients to be screened and more consistent diagnoses can be given time efficiently [55].

In this research, we focus on automating steps for detecting retinal changes associated with one of the most common retinal disease i.e. glaucoma [110]. Glaucoma is a group of eye diseases which is associated with functional failure of the visual field. It is one of the most common and leading cause of blindness [110] among retinal diseases with 13% of the blindness cases being affected [4]. It is estimated that more than 500,000 people suffer from glaucoma in England and Wales alone, with more than 70 million people affected across the world [6]. The changes occur in the retinal structures, which gradually can lead to peripheral vision loss and eventually causes blindness if left untreated. As lost capabilities of the optic nerve cannot be recovered, early detection and subsequent treatment are essential for affected patients to preserve vision.

1.2 Research Problems

Glaucoma can be diagnosed from 2-Dimensional retinal scan taken from fundus camera or the SLO. A retinal scan obtained from the SLO has the artefacts (e.g. eyelids or eyelashes) imaged alongwith the retina. Therefore, it is a challenging task to determine true retinal area in SLO images for disease analysis. Most of the clinical indications associated with glaucoma are related to changes in the Optic Nerve Head (ONH) structure. Hence, the accurate automatic localization of the ONH is quite critical for determining the ONH cropped image (image with the ONH area as the main object). An ONH cropped image is required for the automatic determination of glaucoma related features.

There are several clinical signs associated with glaucoma. These include Cup to Disc Ratio (CDR), vasculature shift, neuroretinal rim loss and occurrence of Peripapillary Atrophy (PPA) around the ONH. The CDR is the ratio of diameter of optic cup to the diameter of optic disc. The value is usually high in case of glaucoma due to large size of optic cup. The increase in optic cup size result in diminishing of the area between optic cup and optic disc boundary known as neuroretinal rim. This phenomenon is called neuroretinal rim loss. Both the CDR and neuroretinal rim loss can be calculated by segmenting out optic disc and optic cup. In case of glaucoma, the

retinal vasculature area which converge at optic disc centre is shifted away from the centre. This phenomenon is called vasculature shift. The PPA is observed as a rough texture around optic disc (refer Chapter 2 for details). These indications reflect the changes in terms of geometry, shape, texture, etc. Also, the accurate segmentation of vasculature is quite critical in determining vasculature shift.

There are several issues associated with determination of geometrical and textural indications associated with glaucoma. Firstly, there are a limited number of public available datasets for glaucoma with limited numbers of annotations around glaucoma related retinal structures. Therefore a benchmark database is required so as to evaluate our algorithms. Secondly, there are little or no clinical annotations for the PPA to determine the segmentation accuracy. The PPA refers to textural change around the ONH due to glaucoma (Chapter 2). Due to this reason we need to find the new method which can represent the presence of PPA due to glaucoma. Thirdly, no clinical indications is the guaranteed sign of glaucoma when observed individually.

The above discussion motivates the following research problems:

1. What is the efficient way of determining the true retinal area while avoiding over-segmentation of artefacts?

2. How to accurately localize and segment out the ONH related structures such as optic disc, optic cup, vasculature structure for determining geometrical indications e.g. Cup to Disc Ratio (CDR), vasculature shift etc?

3. How to detect the PPA with the CDR and vasculature shift for classification between normal and glaucoma images?

4. How can the performance of the algorithms related to glaucoma analysis be evaluated ?

1.3 Thesis Contributions

This project is concerned with the development of an automatic Glaucoma Detection Framework (GDF). The framework involves development of reliable and robust algorithms for automatic determination of changes in retinal structures and image-based

patterns associated with glaucoma which would assist diagnosis in a timely manner and feasibly necessary treatment to prevent blindness. In this work, several major contributions have been made towards the development of the automatic GDF consisting of the stages of preprocessing, optic disc and cup segmentations and regional image feature methods for classification between glaucoma and normal images. These contributions have addressed the research questions mentioned in the previous section. The specific contributions of this project include:

1. Preprocessing Stage

    - Development of a superpixel-based retinal area detector to determine the true retinal area from the SLO images while preserving computational efficiency and avoiding over-segmentation of artefacts.
    - Determination of a new weighted feature map approach which can enhance the ONH region for more accurate localization.
    - Development of the ONH cropped image based vasculature classification model to segment out vasculature while avoiding misidentification of the ONH boundary being a part of vasculature structure.

2. Development of the models for optic disc and optic cup segmentation including:

    - *Region Classification Model* (RCM) which initially determines the optic disc/cup region using selected feature maps.
    - *Point Edge Model* (PEM) which updates the contour using force fields of the selected feature maps.
    - *Weight Point Edge Model* (WPEM) which determines the force field using the weighted feature maps calculated by the RCM for optic cup in order to enhance the optic cup region compared to rim area in the ONH.

    The combination of RCM and PEM is called *Point Edge and Region Classification Model* (PERCM) for optic disc segmentation whereas the combination of WPEM and RCM is called *Weighted Point Edge and Region Classification Model* (WPERCM) for optic cup segmentation.

3. Development of *Regional Image Features Model* (RIFM) for classification between normal and glaucoma images using image-based information from different regions of the ONH image. These regions are clinically observed for analyzing glaucoma related indications especially the PPA. The results of the model can also represent the presence of PPA due to glaucoma.

4. Accommodation of geometrical indication calculated by optic disc, optic cup and vasculature segmentation (e.g. CDR, vasculature shift) with results of the RIFM to perform classification between normal and glaucoma images.

The accuracy and robustness of the methods have been evaluated against the reference image database composed of retinal images annotated by professional ophthalmologists. The performance of the algorithms has been determined by comparing their results with those obtained from clinical annotations. The database includes the SLO images obtained from Optos (also called Optomaps) as well as publicly available fundus retinal images related to glaucoma.

1.4 Thesis Outline

The remainder of the thesis is composed of the following chapters.

Chapter 2: Glaucoma Disease and Its Clinical Diagnosis. This chapter presents the physiological structure of a human eye, gives description of glaucoma as a retinal disease, changes in retinal structures associated with glaucoma and current clinical methods for glaucoma diagnosis.

Chapter 3: Automatic Detection of Glaucoma Related Features - Survey. This chapters reviews reported methods related to automatic detection of features associated with glaucoma. Such methods includes both segmentation and non-segmentation based methods.

Chapter 4: Glaucoma Detection Framework (GDF) - Rationale and Principles. This chapter outlines the proposed framework of glaucoma detection. It describes the rationale and principles of the GDF including a system overview, a description of the reference retinal image database used, image-based feature generation and selection methods, and evaluation metrics used for comparison with the previous

methods. The detailed descriptions of each proposed method and step can be found in Chapter 5,6,7,8 and 9.

Chapter 5: Retinal Image Preprocessing. This chapter discusses the proposed methods for the pre-processing stage. It is composed of three steps:

1. Construction of a novel superpixel-based classification model for determining the true retinal area in the SLO retinal scans.

2. Determination of a weighted feature-map-based ONH localization method.

3. Development of a classification model to segment out the vasculature structure from the ONH cropped image.

The determination of the true retinal area is essential for automatic analysis of retinal diseases. The localization of the ONH is the key step for analysis of the symptoms associated with glaucoma. These symptoms can be analyzed on the ONH image i.e. the part of the retinal image with the ONH as the main object. The vasculature shift is one of the geometrical indications associated with glaucoma which require vasculature segmentation.

Chapter 6: Optic Disc Segmentation. This chapter presents the combination of *Point Edge Model* and *Region Classification Model* called *Point Edge and Region Classification Model* (PERCM) for the determination of an optic disc boundary. It initially determines the optic disc region on the basis of a *Region Classification Model* (RCM). The RCM works on the selected feature set which is best suited for optic disc region determination without being distracted by the PPA around it or vasculature occlusion. It then updates the optic disc contour using force-field-based *Point Edge Model* (PEM). The a force field is calculated on the feature maps with the strongest gradient at optic disc boundary. The accurate boundary detection of optic disc together with optic cup segmentation can be used for automatic determination of geometrical symptoms associated with glaucoma such as Cup-to-disc ratio (CDR), neuroretinal rim loss etc.

Chapter 7: Optic Cup Segmentation. This chapter presents the combination of *Weighted Point Edge Model* and *Region Classification Model* called *Weighted Point Edge and Region Classification Model* (WPERCM) for the accurate segmentation of another geometrical structure associated with glaucoma analysis i.e. optic cup. In

contrast to the PERCM, the WPERCM addresses the issue of weak gradient between optic cup and the ONH rim area. The PEM model determines the force field using the weighted feature maps whose weights are obtained from the RCM. These classification weights represent the membership value of belonging to either optic cup or the ONH rim area.

Chapter 8: Regional Image Features Model for Glaucoma Detection. In this chapter, we present our *Regional Image Features Model* (RIFM) for classification between normal and glaucoma images. We divide the ONH centered image into different regions i.e. the ONH area, inferior (I), superior(S), nasal(N) and temporal(T). These regions are usually established by the clinicians for the diagnosis of glaucoma. We perform the classification between normal and glaucoma images using regional image features.

Chapter 9: Diagnosis of Glaucoma. In this chapter, we develop the classification model between normal and glaucoma images using RIFM classification results and geometrical symptoms associated with glaucoma. The geometrical symptoms can be determined by the segmentation methods as discussed in Chapters 5,6,7 and RIFM classification results have been determined in Chapter 8.

Chapter 10: Discussion and Conclusion. This chapter summarizes our contributions in the thesis and proposes future directions.

Chapter 2

Glaucoma Disease and its Clinical Diagnosis

2.1 Introduction

In this chapter we will discuss the physiological structure of a human eye, a description of glaucoma as a retinal disease, changes in retinal structures associated with glaucoma and the current clinical methods which are currently practiced for glaucoma diagnosis. Before carrying out the study of automatic detection of glaucoma related retinal symptoms, we need to discuss them. Also we need to determine the importance of automatic detection methods in current clinical practice.

2.2 Structure and Function of the Eye

In the optical sciences, the working of human eye is often compared to that of camera [130]. Light reflected from an object is focused on the retina after passing through the cornea, pupil and lens, which is similar to the light passing through the camera optics to the film or a sensor. In the retina, the incoming information is received by the photoreceptor cells dedicated for detecting light. From the retina, the information is further transmitted to the brain via the optic nerve, where the sensation of sight is produced. During the transmission, the information is processed in the retinal layers. A cross-section of the eye and the structures involved in the image formation are presented in Figure 2.1. The camera has three main parts which can be analogous to

human eye i.e. aperture, camera lens and camera sensor. The role of retina same as that of camera sensor.

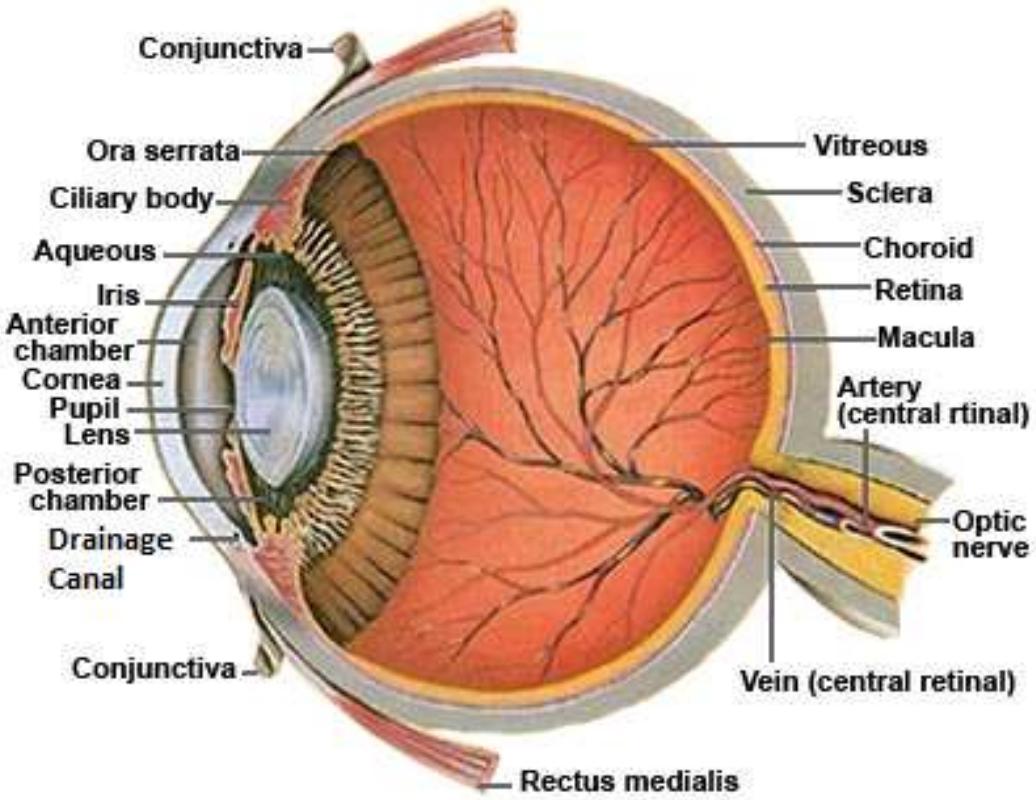

Figure 2.1: Cross-sectional view of human eye [2]

Retina is the inner surface of the eye and consists of transparent tissue of several layers of cells designated to absorb and convert the light into neural signals [53]. The order of the retinal layers is peculiar since the conversion is carried out by the light detecting photoreceptor cells on the layer which is in the back of the retina and furthest from the light. Thus, the light has to travel through the retinal layers before it reaches the photoreceptor cells. Once the light is detected, converted and the neural signals collected to the optic nerve, the impulses are finally transmitted to the brain. During transmission from the photoreceptor cells to the optic nerve the electric impulses are further processed in the inner layers of the retina.

The detailed central vision is formed in the macula (Figure 2.1 and 2.2) which is a highly light sensitive area 5 to 6 mm in diameter in the central region of the retina [46]. In the centre of macula is a round shaped area known as fovea, where the cones are almost exclusively found. The cones are photoreceptor cells selectively sensitive to different wavelengths of light. Next to the macula is the beginning of Optic Nerve

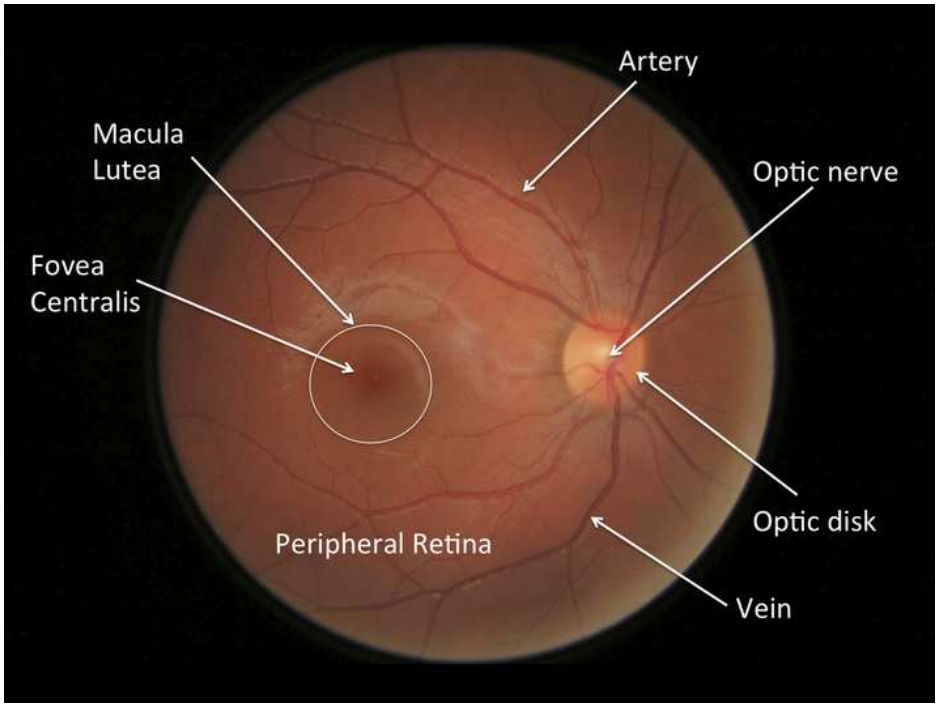

Figure 2.2: The retinal image with labeled retinal structures

Head (ONH), from where the main artery and vein (collectively called vasculature structure) emerge in the retina. The following sections discuss about glaucoma, its clinical methods for diagnosis and retinal symptoms associated with it.

2.3 Glaucoma and its Clinical Methods for Diagnosis

Glaucoma is one of the most common and leading cause of blindness [110] among retinal diseases with 13% of the blindness cases being affected [4]. The changes occur in retinal structures gradually leads to peripheral vision loss (see Figure 2.3). The structural changes are manifested by a slowly diminishing neuroretinal rim indicating a degeneration of the retinal nerves [92]. There is no cure for glaucoma but its early diagnosis and treatment at the earlier stage can prevent the vision loss.

Glaucoma is usually realized by a patient after a long time of disease progression. This is because glaucoma usually damages the outer edge of the eye and works slowly inwards [12]. Therefore, it is important to have regular eye tests so that any symptoms can be detected and treated as early as possible. According to UK's National Institute

Figure 2.3: Normal vision vs glaucoma vision [5]

of Health and Clinical Excellence (NICE) guidelines [11], the tests which should be offered for suspecting glaucoma are briefed as follows:

Figure 2.4: Tonometry as clinical example to suspect glaucoma using IOP [5]

- **Tonometry** uses an instrument called a tonometer to measure Intra Ocular Pressure (IOP) of the eye. Glaucoma is suspected if IOP value exceeds 21Hg. There are several techniques for tonometry [21].
- **Pachymetry** is the test used to determine thickness of cornea.
- **Gonioscopy** is an examination of the front outer edge of the eye, between the cornea and the iris. This is the area where the fluid should drain out of the eye. Gonioscopy can help to determine whether the drainage angle is open or closed (blocked).

- **Perimetry** is a systematic measurement of light sensitivity in the visual field by detection of targets presented on defined background. It checks for missing areas of the peripheral vision glaucoma initially affects the peripheral vision loss.

- **Ophthalmoscopy** involves examination of the retinal area which is the main retinal structure affected by glaucoma. The clinicians use the imaging instruments which can enhance the retinal area for visual examination [3].

Among these common tests, the tonometry is not an effective screening tool for glaucoma as high pressures of IOP are not an accurate indication for glaucoma as different patients have different cornea thickness [9,38] and glaucoma can be present with and without high IOP [26]. Perimetry is likely to miss most patients with early glaucoma damage as these patients do not have many visual symptoms [22]. It may take three examinations before an accurate baseline is obtained and moreover long-term fluctuations in the field tests can often occur. Therefore the accuracy of this method is still questioned [42, 117]. Assessment of the retinal area using ophthalmoscopy is more promising and superior to tonometry or perimetry since the changes in retinal area due to glaucoma precedes vision loss and can be used to detect glaucoma earlier with higher sensitivity [84]. However, the manual assessment of the retinal area is subjective and time consuming. There remains a strong need to automate steps in the ophthalmoscopy so as to diagnose glaucoma in a time efficient manner.

2.4 Glaucoma Assessment by Ophthalmoscopy

Glaucoma can be diagnosed by observing the retinal changes present in the retinal scan. These changes are observed manually by the eye clinicians using the imaging instruments which can enhance the retinal area for visual examination. There are two most common imaging modalities which are used to obtain 2D retinal scan i.e. fundus camera and Scanning Laser Ophthalmoscope.

2.4.1 Fundus Camera

A typical fundus camera [7] (Figure 2.5(b)) views 30 ° to 50 ° of retinal area with a magnification of 2.5 and allows some modification of this relationship through zoom

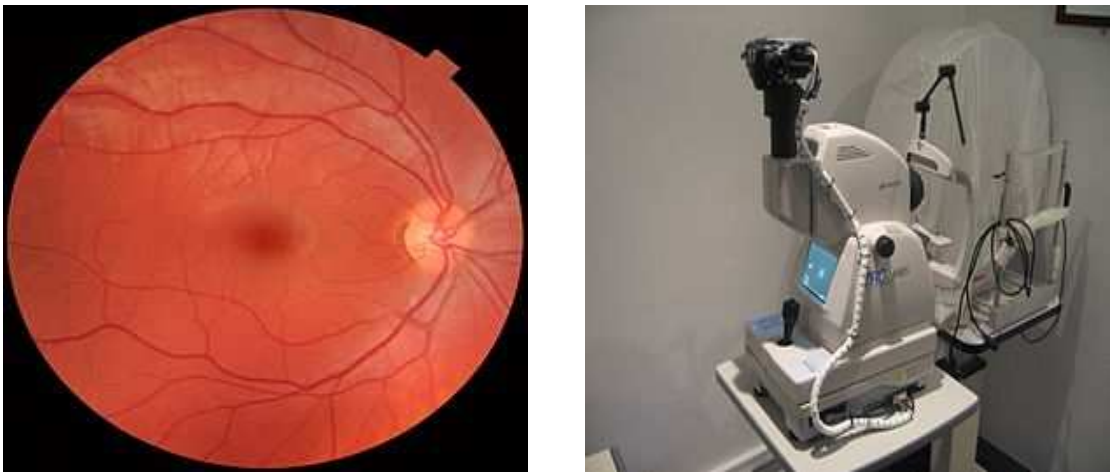

(a) (b)

Figure 2.5: Example of (a) fundus image and (b) fundus camera [7]

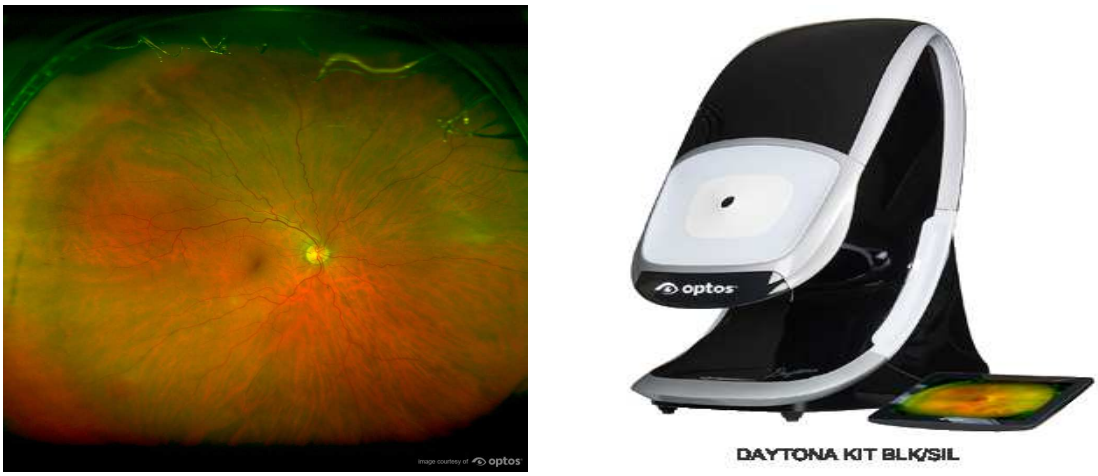

(a) (b)

Figure 2.6: Example of (a) SLO image and (b) SLO device from Optos [8]

or auxiliary lenses from 15° to 140° with a wide angle lens. The optical design of fundus cameras is based on the principle of monocular indirect ophthalmoscopy. The observation light is focused via a series of lenses before passing through the camera objective lens and through the cornea onto the retina. When the button is pressed to take a picture, a mirror interrupts the path of the illumination system allow the light from the flash bulb to pass into the eye. The reflected light from the retina then forms the image as shown in Figure 2.5(a).

2.4.2 Scanning Laser Ophthalmoscopy

The Scanning Laser Ophthalmoscope (SLO) (Figure 2.6(b)) incorporates low-powered laser wavelengths that scan simultaneously. This allows review of the retinal substructures in their individual laser separations. There are several companies which are involved in design and manufacturing of SLO devices [8, 96, 122]. The retinal scan obtained from SLOs of different companies have different specifications in terms of resolution, Field-of-View (FOV) and grayscale values. Among existing SLO devices, the SLOs manufactured by our collaborator, Optos have the largest FOV and becoming popular among retinal imaging devices with one of leading market shares in the USA [8]. In an SLO image obtained from our collaborator Optos, each image has a FOV of up to 200 ° of the retina at resolution 14 μm. The device captures the retinal image without dilation, through a small pupil of 2 mm. The image has two channels: red and green. The green channel (wavelength: 532nm) provides information about the sensory retina to retinal pigment epithelium whereas the red channel (wavelengh: 633nm) shows deeper structures of the retina towards the choroid. An example image is shown in Figure 2.6(a).

2.5 Retinal Symptoms of Glaucoma

There are two main types of glaucoma (i) Primary Open Angle Glaucoma (POAG) and (ii) Angle Closure Glaucoma (ACG). POAG is the most common form of glaucoma accounting for at least 90% of all glaucoma cases [13]. The Intra-Ocular Pressure (IOP), which maintains a permanent shape of the human eye and protects it from deformation, rises because the correct amount of fluid cannot drain out of the eye. With POAG, the entrances to the drainage canals work properly but a clogging problem occurs inside the drainage canals [132]. This type of glaucoma develops slowly and sometimes without noticeable sight loss for many years. It can be treated with medications if diagnosed at the earlier stage. ACG happens when the drainage canals get blocked. The iris is not as wide and open as in the normal case. The outer edge of the iris bunches up over the drainage canals, when the pupil enlarges too much or too quickly. Treatment of this type of glaucoma usually involves surgery to remove a small portion of the outer edge of the iris. Here we are mostly concerned with POAG

and its symptoms.

By observing the retinal scan obtained from fundus camera or SLO, most of the glaucoma related symptoms are observed in the ONH area. These symptoms are enlisted and explained as follows:

- Optic nerve head variance
- Neuroretinal rim loss
- Vasculature shift
- Peripapillary atrophy

2.5.1 Optic Nerve Head Variance

The Optic Nerve Head (ONH) or the optic disc is the location where the optic nerve enters the back of the eye (Figure 2.1). It is also known as blind spot since this area of retina cannot respond to light stimulation due to lack of photoreceptors. In a typical 2D retinal image, the ONH is a bright elliptic region with a distinguishable cup-like area called optic cup surrounded by rest of the area of optic disc, as shown in Figure 2.7. The ratio of cup measurement to the disc measurement is called Cup to Disc Ratio (CDR). There are several ways to quantify the CDR [50]. For instance, the ratio can be defined with respect to area, vertical length and horizontal length of both optic disc and optic cup. The CDR can be used to compare glaucoma patients with normal subjects, and it is an important measurement for the diagnosis of glaucoma [50]. When more optic nerve fibers disappear, the optic cup becomes larger with respect to the optic disc, which corresponds to increase in CDR value as shown in Figure 2.7. In current clinical practice, the CDR is measured manually by an ophthalmologist. This process is time consuming and is subjective to inter-observer variability since the boundary of the optic cup can not be clearly observed in 2-D retinal scan [83].

2.5.2 Neuroretinal Rim Loss

In normal eyes, the neuroretinal rim (area between optic cup and optic disc boundary) usually follows a characteristic pattern as shown in a retinal image taken from the right eye in Figure 2.8. It is the broadest in the inferior(I) region followed by the superior(S),

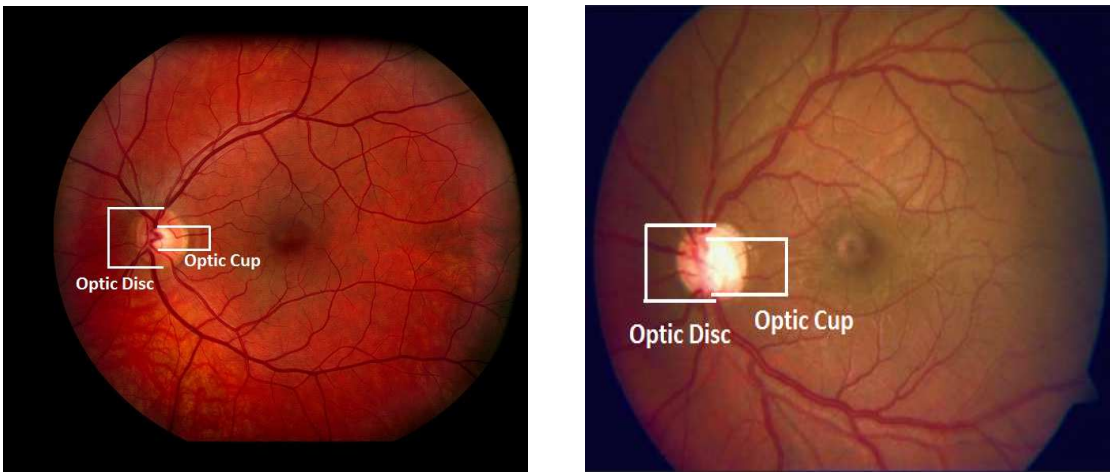

(a) (b)

Figure 2.7: Comparison of CDR in (a) normal image and (b) glaucoma image [1]. The glaucoma image has higher CDR

then nasal(N) and finally the temporal(T) regions, which is called the ISNT rule [67]. In case of glaucoma, the neuroretinal rim disobeys the earlier mentioned rule. Although this is not the case with all glaucoma patients [59], it is still a useful clinical method to aid in diagnosing glaucoma. For the left eye, the position of temporal and nasal region will swap each other.

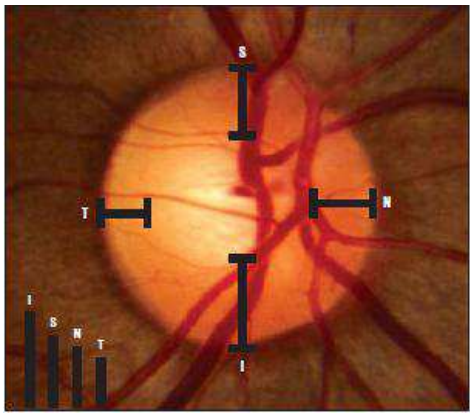

Figure 2.8: Clinical assessment based on the ISNT rule obtained from normal optic nerves. I,S,N and T represent inferior, superior, nasal and temporal regions respectively. The image is taken from the right eye

2.5.3 Vasculature Shift

In the retina, the vasculature area converges towards the ONH area. Therefore, it can also be stated as the convergence point of retinal vasculature structure is the centre of the ONH. In case of glaucoma, the vasculature area is shifted more towards the nasal

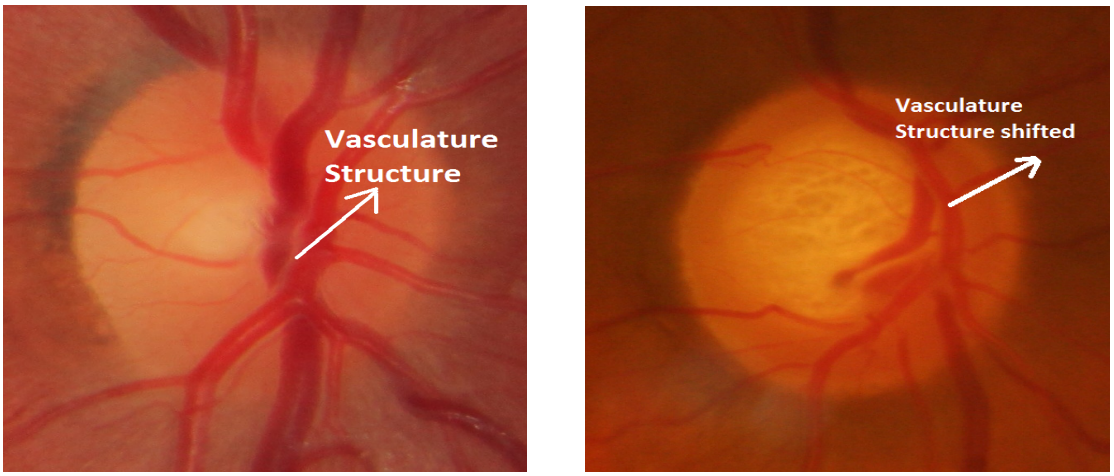

(a) (b)

Figure 2.9: Comparison of vasculature shift in (a) normal image and (b) glaucoma image. The glaucoma image has vasculature shifted towards nasal area

area due to increase in cup size as shown in Figure 2.9. This phenomenon is known as vasculature shift.

2.5.4 Peripapillary Atrophy

Peripapillary Atrophy (PPA) is an important risk factor and its progression can lead to disc haemorrhage and thus glaucoma [64]. It is the degeneration of the retinal pigment epithelial layer and photoreceptors in the region surrounding the ONH [66]. PPA is divided into two zones namely central β-zone and peripheral α-zone as shown in Figure 2.10. α-zone is characterized by irregular hypopigmentation, hyperpigmentation and thinning of tissue layer. On its outer side it is adjacent to retina and on its inner side it is in touch with β-zone characterized by visible crescent like area. In normal eyes, both α-zone and β-zone are frequently located in the temporal region followed by inferior region and superior region. In glaucomatous eyes, β-zone occurs more frequently in the temporal region [41] and its extent correlates with the retinal nerve fibre layer thinning.

2.6 Conclusion

In this chapter, we mainly discuss about retinal symptoms associated with glaucoma and current clinical methods for its diagnosis. Among the recommended tests for

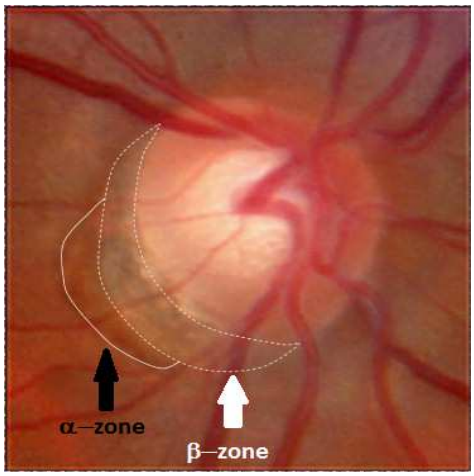

Figure 2.10: PPA with α-zone and β-zone [125]. β-zone occurs more frequently in the temporal region of the right eye

glaucoma diagnosis, the observation of the retinal scan is the promising method for diagnosis and assessment of glaucoma. These retinal scans can be obtained from the imaging modalities such as fundus camera or SLO. From the retinal scan, it can be observed that glaucoma leads to alterations in the ONH, neuroretinal rim loss, vasculature shift and degeneration of tissue layer around the ONH called peripapillary atrophy. These alterations are observed manually using the modalities such as fundus camera or SLO. The observation of these alterations can be made time efficient and subject to less inter-observer variability by automating steps in determination of these alterations. Other symptoms associated with glaucoma require retinal tissue examination from the modalities such as Optical Coherence Tomography, confocal SLO etc which are available in large hospitals. Nevertheless, their role in detecting any glaucomatous progression is uncertain. Therefore, our thesis is primarily based on automatic determination of the glaucoma related symptoms discussed in this chapter and classification between normal and glaucoma images on the basis of these symptoms automatically determined. The next chapter discusses the previous efforts towards this direction; some of them are still at their earlier stage and need to be improved. This thesis addresses the issues associated with previous efforts by proposing new methods for automatic determination of glaucoma related symptoms and classification between normal and glaucoma images on the basis of automatically calculated glaucoma related symptoms.

Chapter 3

Automatic Detection of Glaucoma Related Features - Survey

3.1 Introduction

Since the current clinical methods for the diagnosis of glaucoma are mostly based on manual observations, therefore the use of automatic detection of features related to glaucoma can aid their diagnosis in a time effective and non-invasive manner. There is no cure for glaucoma but its diagnosis and treatment at the earlier stage can slow down the progression of the disease. There are some segmentation (Section 3.2) and non-segmentation (Section 3.3) based automatic methods used to determine features of the retinal structures that reflect changes due to glaucoma. Since most of segmentation based need ONH analysis, therefore, most of the existing methods for analysis of the glaucoma are related to extraction of ONH and its anatomical structures. The methods described in this section are classified in terms of image processing techniques and are mentioned in the form of hierarchy as shown in Figure 3.1. Their results are summarized in Table 3.1 to Table 3.4. The results which were applied on common datasets are grouped together so as to compare different methods on a common benchmark.

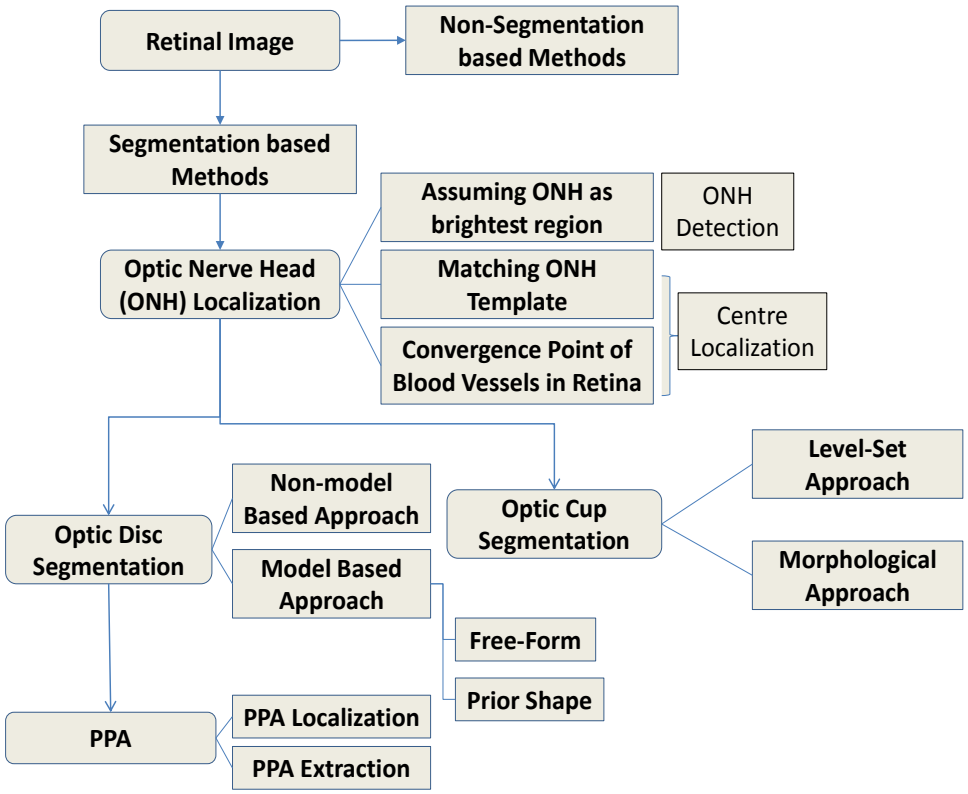

Figure 3.1: A hierarchy of methodologies for automatic feature extraction from digital retinal images

3.2 Segmentation based Automatic Feature Detection Methods

3.2.1 Localization of ONH

The localization of the ONH is the initial step in order to locate other anatomical structures, vessel tracking and registering changes within optic disc region. If any pixel within the optic disc boundary is located, then it can facilitate the extraction of the optic disc boundary. We have divided the localization methods of the optic disc into three categories which are discussed in the following paragraphs and a summary of the methods is shown in Table 3.1. The table presents the comparison of optic disc localization accuracy where the colour space represent the channel where the method was applied. Most of the datasets are publicly available and has been shown with the respective reference [10, 51, 118].

1) Optic Disc Detection as the Brightest Region

The first category is based on calculating the intensity of pixels in coloured and grayscale images. Under normal circumstances, the optic disc region is the brightest region on the retinal image as shown in Figure 3.2. Therefore it can be detected by thresholding out the pixels with the intensity values below the certain level [31].

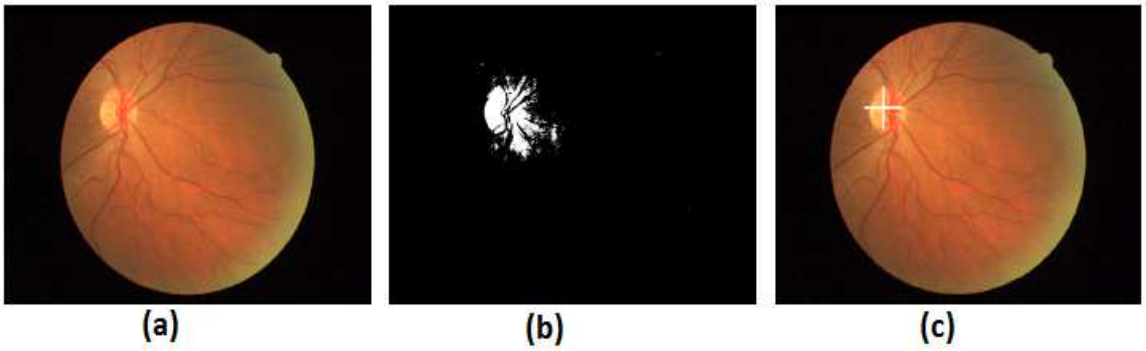

Figure 3.2: Example of optic disc localization as brightest region (a) fundus image (b) determination of 2% brightest region and (c) optic disc localization [54, 131]

Sinthanayothin *et al.* [114] localized the optic disc using local contrast colour enhancement in intensity-hue-saturation space. The variance image after converting back to RGB space will intensify the optic disc as compared to rest of the image. The algorithm resulted in high accuracy in their local dataset however, others have found its high failure rate in the images with a large number of white lesions, bright reflections or strongly visible vessels [85]. The use of pre-processing steps such as image filtering for removing reflections brighter than the optic disc may result in improvement of the results. Walter *et al.* [131] localized the optic disc center with the proposal to select the brightest two percent of the image pixels to determine a threshold (Figure 3.2). After thresholding the image, the region with the largest area is likely to be the optic disc region. The algorithm was applied on a set of 30 retinal images however, it failed on a low contrast image. Sekhar *et al.* [112] improved the method by utilizing mathematical morphology to apply the shade correction on the retinal image. The mathematical morphology is the process of analyzing the geometrical structures present in the image by affecting their shape and form [52]. The largest area of the shape corrected retinal image was considered as optic disc region. The shade correction although improving the localization accuracy as compared to the previous method, its role in locating the

optic disc region is uncertain. In order to locate the optic disc automatically, both methods used a circular Hough transform [107] which aims to find circular patterns within an image.

In spite of assuming the optic disc as the brightest region of the retinal image is the straightforward approach to localize the region, the method is unreliable. The technique usually fails to localize the optic disc in the retinal images having reflections and the bright lesions in the diseased retina. Moreover, this assumption is not a guaranteed way to determine the center of the optic disc.

2) Center Localization by Matching of the Optic Disc Template

The second category is based on formation of template representing the optic disc and matching the template in a test image. The results were comparatively accurate as compared to first category at the expense of the computational time [79]. Later on, the computational time was reduced by introducing efficient algorithmic procedure. An example has been shown in Figure 3.3.

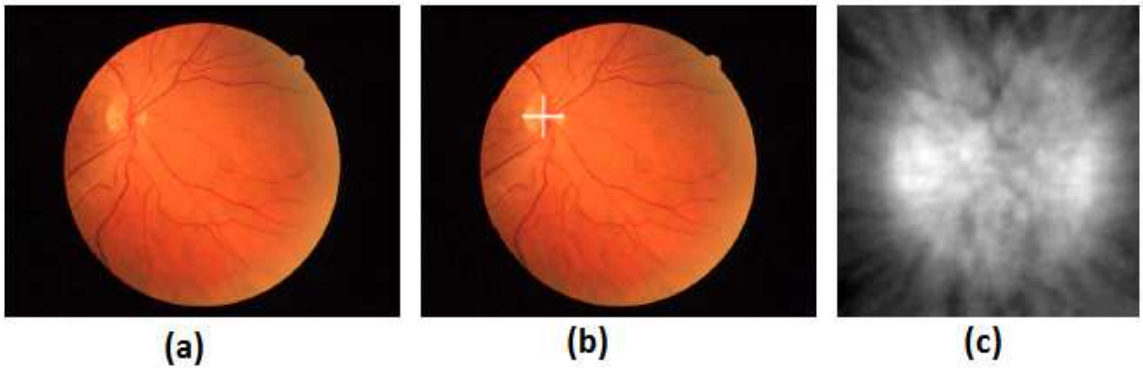

Figure 3.3: Example of optic disc localization using template matching (a) fundus image (b) optic disc localization (c) the template [54, 79]

Li *et al.* [79] modeled the optic disc texture using Principal Component Analysis (PCA). The optic disc in a test image was localized by dividing the test image into square grid with each square equal to size of the optic disc. The Euclidean distance from the PCA-model of optic disc was calculated for each grid element. The grid space with the optic disc at the center will have least Euclidean distance from the PCA model. According to the author, the results were accurate however no accuracy was reported. Computational time may be reduced if the image resolution is reduced as less

Table 3.1: Accuracy of several methods of optic disc detection / center localization

Localization Method	Image Database	Colour Space	Image Dimension	Number of Test Images	Accuracy	Citation
ONH as brightest region						
Local Contrast Colour Enhancement	STARE [51]	24-bit RGB to IHS space	605 x 700	81	42% within ONH	[54, 114]
Thresholding highest Pixel Intensities	STARE [51]	24-bit RGB to HLS space	605 x 700	81	58% within ONH	[54, 131]
Shade Correction using Morphology	STARE [51]	24-bit RGB	605 x 700	17	82.3% within ONH	[112]
Shade Correction using Morphology	DRIVE [118]	8-bit RGB	768 x 584	38	94.7% within ONH	[112]
ONH template matching						
Least Squares Regression Arc Estimation	STARE [51]	24-bit RGB	605 x 700	81	58% within ONH	[54, 101]
Pyramidal Decomposition and Circular Template Matching	STARE [51]	24-bit RGB	605 x 700	81	71.6% within ONH	[54, 76]
Vasculature Detection using matched filter	STARE [51]	24-bit RGB	605 x 700	81	98.7% within 60 pixels	[140]
	DRIVE [118]	8-bit RGB	768 x 584	40	100% within 60 pixels	
Principal Component Analysis	National University Hospital Singapore	24-bit RGB	512 x 512	40	Accuracy not reported	[79]
Averaging Optic Disc Region	Bristol Eye Hospital	24-bit RGB	760 x 570	60	Accuracy not reported	[101]
Vasculature convergence point						
Fuzzy Convergence of Blood Vessels	STARE [51]	24-bit RGB	605 x 700	81	89% within 60 pixels	[60]
Mathematical modeling of Vasculature Structure	STARE [51]	24-bit RGB	605 x 700	81	98% within ONH	[45]
Tensor Voting and Mean-Shift procedure	STARE [51]	24-bit RGB	605 x 700	81	92% within ONH	[102]
Horizontal and Vertical Edge Mapping	STARE [51]	24-bit RGB	605 x 700	81	97% within 60 pixels	[88]
Horizontal and Vertical Edge Mapping	DRIVE [118]	8-bit RGB	768 x 584	40	97% within 60 pixels	[88]
Fractal Dimension Analysis	DRIVE [118]	8-bit RGB	768 x 584	40	Accuracy not reported	[139]
Gabor Filter Vessel Detection	MESSIDOR [10]	8-bit RGB to CIE space	1440 x 960 2240 x 1488 2304 x 1536	1200	98.3% within ONH	[141]

number of pixels will allow to execute the task earlier but consequently, it might skip some of the textural information resulting in decrease in accuracy of the localization. Osareh *et al.* [101] evaluated the normalized correlation coefficient in order to compare the template image with the region of consideration. The template was generated after averaging the 16 colour-normalized retinal images. The method only detected the location based on highest value of normalized correlation coefficient which does not necessarily mean the optic disc center. They further improved their template by dividing the optic disc into smaller segments and selecting the largest segment which is approximate to a half circle and the region is not occluded by blood vessels. The algorithm followed the iterative procedure for minimizing the error between the set of pixels in the arc points and the estimated arc. The center of the circular arc is the approximate location of optic disc center. These template based matching algorithms were less computationally efficient therefore some pre-processing steps were introduced in order to improve the computational time.

Lalonde *et al.* [76] proposed an optic disc center detection method based on Pyramidal Decomposition and circular template matching. Pyramidal Decomposition reduces the image resolution to one-fourth at each iteration level. At the fifth level, bright regions of retina other than optic disc were vanished. The localization of the brightest pixel led to the determination of optic disc area for determining the edges of anatomical structures. The edge map was thresholded based on the strongest edges in the retinal image and the circular template was then compared with the pixels having strong edges. This made the computational time smaller as the template did not need to be compared pixel by pixel in the retinal image. Then pixel with the lowest degree of mismatch (Hausdorff distance) with the circular template and the highest confidence value was regarded as optic disc center. The author reported the failure cases when pyramidal decomposition sometimes localized the brightest pixel very far from optic disc due to bright reflections in the retinal image, and Hausdorff distance based circular template matching was failed when optic disc was highly occluded by blood vessels. As discussed earlier, the use of image filtering e.g. directional Gabor filters as a preprocessing step can improve the results. Yousiff *et al.* [140] applied directional matched filter in order to determine the vasculature structure. Then a window of 9x9 from the test image was compared on the pixels belonging to the vasculature structure

which can be resized based on size of the image. The pixel with least accumulative distance was regarded as optic disc center. Yu *et al.* [141] used binary template to define the search region of the optic disc. They further applied the directional Gabor filters and calculated the standard deviation of the optic disc pixel candidates. These pixel candidates were determined after sorting the pixels of the search region using Pearson's correlation coefficient. The pixel candidates with maximum standard deviation was regarded as the optic disc center.

Center localization of the optic disc using template matching proved to be more accurate as compared to the methods based on assumption of highest pixel intensity values within optic disc region due to non-uniform illumination in the retinal image. PCA and circular arc based template matching were the initial steps towards the optic disc center localization [54,76,79,101]. In spite of they were more accurate as compared to pixel intensity based techniques, they were still not able to distinguish among bright reflections across the retinal image. Moreover, the removal of blood vessel occlusion reduced the quality of template to be compared. Pyramidal decomposition improved the center detection in terms of computational time however, the misguidance by bright reflections remained. The use of directional filters for vasculature segmentation were then introduced which not only reduced the search region for the best candidate of the optic disc center but also improved the detection accuracy. But the use of directional filters may be less applicable to the images diseased with glaucoma as the atrophy around the optic disc would also be segmented out as the part of the vasculature structure which may affect the detection accuracy based on template matching.

3) ONH center as Convergence Point of Retinal Blood Vessels

The third category of the ONH localization can be regarded as the convergence point of blood vessels in retina to be the center of the ONH. This assumption avoided mislocalization of the optic disc as most of the retinal blood vessels converge within the ONH region. Moreover if the retinal vasculature structure is segmented out accurately, it can also avoid the detection failure of optic disc center due to template matching. An example has been shown in Figure 3.4.

Hoover *et al.* [60] segmented out the blood vessels in order to determine the point of intersection. A voting process was introduced in order to find out points where a large

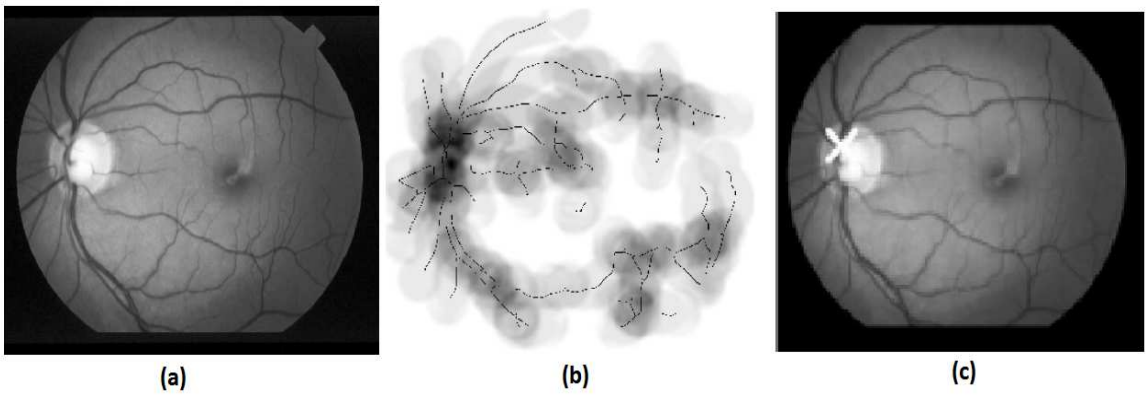

Figure 3.4: Example of optic disc localization using vasculature convergence point detection (a) fundus image (b) detection of vasculature convergence point (c) optic disc localization [60]

number of blood vessels combine and the point with maximum votes was regarded as ONH center. Then, illumination equalization was applied in order to determine the different region in retinal image since the method was also applied to retinal images having diseases such as Diabetic Retinopathy (DR) and Age-Related Macular Degeneration (AMD) which shows different bright spots on retina. Finally, hypothesis was developed based on region size and if only one region was classified out, it was considered as optic disc region. The hypothesis testing might involve parameters other than region size such as region circularity in order to improve the accuracy. Foracchia *et al.* [45] not only localized the ONH center as the main convergence point of blood vessels but also approximated the entire vasculature structure by fitting it with a mathematical model. The algorithm does not require accurate vasculature segmentation although it may not converge in the retinal images with low contrast ONH regions. Ying *et al.* [139] differentiated ONH from other bright regions, including exudates and lesions, based on fractal dimension of blood vessels. A fractal dimension is a ratio providing a statistical index of complexity comparing how detail in a pattern changes with the scale at which it is measured. The fractal dimension of vasculature structure within ONH area is approximately 1.7 and it is higher as compared to fractal dimension of other bright areas. The method was applied on DRIVE database but no overall accuracy of the method was reported. Besides, the authors suspected the algorithm failure on low quality images. Park *et al.* [102] extracted out vasculature structure based on tensor voting. Tensor voting is the voting process of the expected candidates based on geometrical features. The image was initially contrast enhanced

before application of tensor voting process. The optic disc was detected using mean shift procedure which points towards direction of maximum increase in the density (convergence point of blood vessels). The algorithm had higher failure rate on diseased images with white lesions. Mahfouz *et al.* [88] used the horizontal and vertical edge maps to locate the ONH center. These maps can be used to accurately localize the ONH center based upon a simple observation; the central retinal artery and vein emerge from the ONH mainly in the vertical direction and then progressively branch into the main horizontal vessels. The highest projection amplitude along both directions will result in center localization in a computationally efficient manner. The accuracy of the method was highly dependent on horizontal localization process.

The determination of convergence point of vasculature structure is the most efficient way to localize the optic disc in terms of accuracy, robustness and computational time. The methods can be applied to most of the fundus retinal images. The proved the high accuracy in case of healthy images however, the algorithms were misguided due to presence of white lesions. Retinal images diseased with glaucoma may not have white lesions but the presence PPA may misguide the center detection of optic disc which is usually required for optic disc and cup segmentation followed by their measurements for glaucoma diagnosis. Therefore, combining the best features of different vasculature convergence point based algorithms may improve the center detection accuracy in the case of diseased images.

3.2.2 Optic Disc Extraction

In our literature survey, we have divided the different methods of optic disc extraction into non-model-based approaches and model-based approaches. In the non-model-based approaches, the optic disc is extracted using different image processing algorithms such as morphological operations, pixel clustering etc. In the model-based approaches, the optic disc boundary is represented in the form of mathematical model. The model-based approach is further classified into three categories i.e. boundary approximation modeling, freeform modeling and statistical shape modeling. Boundary approximation modeling approximate the optic disc boundary with either circular or elliptical shape. The freeform modeling tend to represent the optic disc boundary while minimizing the energy constraints of its gradient map. The statistical shape

modeling represent the optic disc boundary in the ways which are consistent with the training set. All these approaches have been discussed in the following subsections and the results of the methods under each category have been summarized in Table 3.2.

1) Non-Model-Based Approaches

For a non-model-based approaches, the optic disc was either segmented out using different thresholding techniques or morphological operations. Initially, morphological approach was introduced for optic disc segmentation as it required basic image processing techniques. An example for optic disc and cup segmentation using morphological operation has been shown in Figure 3.5.

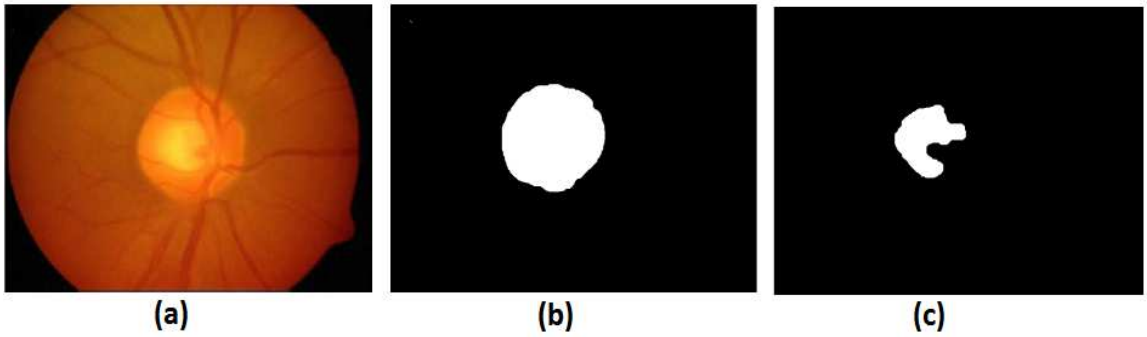

Figure 3.5: Example of optic disc segmentation using morphological operation (a) fundus image (b) optic disc segmentation (c) optic disc segmentation [99]

Walter and Klein [131] described an approach in which the RGB image was converted to Hue-Luminance-Saturation (HLS) space and a thresholding was applied to approximately localize the optic disc center in the luminance channel. Then the precise boundary of the optic disc was determined using the red channel of the RGB image via the watershed transform [109] involving morphological pre-processing of the gradient image and region growing image segmentation. After watershed transform, the image is divided into small regions called superpixels. The red channel was selected as optic disc boundary is more prominent here. To determine the optic disc, the watershed transform is constrained by markers derived from a previously calculated optic disc center. The identification process of the optic disc boundary had some problems due to blood vessels occlusion. This problem might be solved if the superpixels are generated using Simple Linear Iterative Clustering (SLIC) [15]. Nayak *et al.* [99] applied the morphological operations in the red channel of the RGB image in order to segment out

Table 3.2: Results of different methods of optic disc extraction

Localization Method	Image Database	Colour Space	Image Dimension	Number of Test Images	Accuracy	Citation
Non-model-based approach						
Morphological Operation	Kasturba Medical College India	8-bit RGB to Grayscale	560 x 720	24 Normal and 37 Glaucoma	90% Neural Network [116] classification	[99]
Fuzzy Histogram	Kasturba Medical College India	8-bit RGB to 'Lab' space	560 x 720	30 Normal, 31 Retinopathy and 39 Glaucoma	93.4% Overlapping Score	[94]
K-Means Clustering	Aravind Eye Hospital India	YUV space	1504 x 1000	20 Normal and 25 Glaucoma	91.7% CDR Correlation Coefficient	[20]
Watershed Transformation	Mines ParisTech	8-bit RGB to HLS space	640 x 480	30	-	[131]
Thresholding	STARE [51]	24-bit RGB	605 x 700	81	93% of OD diameter	[75]
Boundary approximation modeling						
Circular Hough Transform on gradient map	MESSIDOR [10]	8-bit RGB	1440 x 960 2240 x 1488 2304 x 1536	1200	86% Overlapping Score	[19]
Genetic Algorithm for elliptical approximation	DRIONDB [27]	8-bit RGB	600 x 400	110	96% images have $\leq$ 5 pixel MAD	[27]
Hough Transform on Edge Map	DRIVE [118]	8-bit RGB to Y channel	768 x 584	40	73% Overlapping Score	[147]
Freeform modeling						
Morphological Preprocessing	NewYork Library	8-bit RGB to YIQ space	285 x 400	9	-	[90, 91]
Morphological Preprocessing	Bristol Hospital	24-bit RGB to 'Lab' space	760 x 570	16	90.3% Overlapping Score	[100]
Circular Hough Transform Initialization	National University Hospital Singapore	24-bit RGB	512 x 512	100	93% images have $\leq$ 3 pixel MAD	[137]
Level-set Approach	Aravind Eye Hospital India	8-bit RGB	2896 x 1944	33 Normal and 105 Glaucoma	97% Overlapping Score	[68]
Fast Level-Set Approach	MESSIDOR [10]	8-bit RGB	1440 x 960 2240 x 1488 2304 x 1536	1200	89.5% 1-(MAD/OD radius)	[141]
Statistical shape modeling						
Image Gradient Based Landmark Search	National University Hospital Singapore	24-bit RGB	512 x 512	35	82% images have $\leq$ 3 pixel MAD	[80]
RANSAC approach	Seoul University Korea	8-bit RGB	2896 x 1944	53 Normal and 30 Glaucoma	84.5% Overlapping Score	[72]
Minimum Mahalanobis distance Method	ORIGA^{-light} [145]	8-bit RGB	3072 x 2048	482 Normal and 168 Glaucoma	89% Overlapping Score	[43]
Search Space Restriction along Normal Lines	DRIONDB [27]	8-bit RGB	600 x 400	110	92% Overlapping Score	[56]

optic disc. They then segmented out the optic cup in the green channel and calculated CDR from the vertical lengths of the segmented areas. Since these algorithms had the tendency to segment out the pixels other than optic disc therefore it led to shape approximation of the anatomical structure. Mookiah *et al.* [94] with their fuzzy histogram approach improved the segmentation accuracy which in their local dataset was even better than model-based Gradient Vector Flow (GVF) technique. The histogram was then correlated with roughness index to represent optic disc region. The authors suggested use of more diverse images and appropriate fuzzy membership functions for increase in accuracy as the algorithm over segmented PPA regions.

In [75], various statistical criteria for thresholding have been employed, such as 1) percentage of higher pixel intensity values; 2) comparative value of pixel intensity as compared to the total intensity values of the extended background image which is other than optic disc area. The overall accuracy was determined in terms of measuring vertical diameter of the optic disc. This method is applicable to both healthy images and images with AMD. Babu and Shenbagadevi [20] used k-means clustering after converting the image into YUV colour space (one luma Y and two chrominance UV components) based on Commission Internationale de Éclairage (CIE) format. They calculated the CDR by taking the rectangular area measurements of both the optic disc and optic cup. The overall accuracy of the method was determined by comparing CDR values with those obtained from Gold Standard values from the Ophthalmologists.

In the non-model-based approaches for extracting out optic disc, the measures such as vertical length or horizontal length were used in determining CDR after extracting out optic cup. CDR, although one of the important aspect in diagnosing glaucoma, it is not crucial for glaucoma documentation [65] as some of the patients can have large size of ONH. Therefore it is sufficient to determine other symptoms such as neuroretinal rim loss, PPA etc which require exact segmentation of optic disc and optic cup. Therefore, model-based approaches can be used in determining out exact boundaries of optic disc and are explained in the following sections.

2) Boundary approximation modeling

These methods are concerned with circular or elliptical shape approximation of the optic disc boundary. These methods might not represent the exact boundary of the

optic disc but can be quite useful in determining CDR. Zhu *et al.* [147] applied the Hough Transform on edge map obtained after applying morphological operations on the luminance gray scale of the image. The luminance grayscale can be obtained after normalizing each component of the RGB space. This method is loosely connected to main convergence point of retinal blood vessels. The authors warned about their method failure on low quality images as circular hough space might be misguided due to weak edge information. Aquino *et al.* [19] approximated the optic disc boundary using circular Hough transform on the gradient image obtained after removal of blood vessels. The results were compared with 'Circular Gold Standards' (benchmarks) obtained from the ophthalmologists. They suspected that performance of elliptical approximation and deformable approaches could outperform circular approximation. Carmona *et al.* [27] obtained a set of hypothesis points that represented geometric properties and intensity levels similar to ONH contour pixels. Then a genetic algorithm was applied in order to find an ellipse approximating the boundary of ONH. The method was applied on DRION-DB database and the accuracy was reported in terms of pixel difference. The authors also reported its computational inefficiency and failure cases on the images having PPA. It might be improved if the hypothesis also involve statistical properties such as entropy, homogeneity etc which can be able to distinguish among PPA and ONH pixels.

3) Freeform Modeling Based Approaches

In the freeform modeling, there is no explicit structure of template except some constraints. In this category, Active Contour Modeling (ACM) [70] has been widely investigated for extraction of optic disc boundaries. ACM is fundamentally a deformable contour. It changes its shape corresponding to the properties of an image-based contour properties and/or knowledge based constraints. The behavior of classical parametric active contours is typically controlled by internal and external energy functions. The external energies determine the region of the model and could be derived from image features such as edges. Internal energies, such as elasticity and rigidity determine the curvature of the model and could serve as smoothness constraints to resist any deformation. The minimization of a total energy function moves the contour towards the target shape.

Mendels *et al.* [90,91] applied morphological operations on retinal images in YIQ(Luminance In-phase Quadrature) followed by an active contour to segment the optic disc. In the morphological process, a dilation operator was first applied followed by an erosion operator in order to retain the disc contour whilst remove the blood vessels. Having removed the blood vessels crossing the disc boundary, an active contour was initialized as a circle centered inside the optic disc. The contour was fitted to the rim of the disc using the Gradient Vector Flow (GVF) derived from edge maps [136]. The final location of the contour was independent of initialization values. This technique was tested on nine retinal images. The morphological preprocessing has been proven effective compared to directly use of original grayscale images, however a quantitative comparison was not presented. Osareh *et al.* [100] applied the same method on different colour spaces and found the 'Lab' space to be more suitable for the application of ACM. Xu *et al.* [137] modified the contour energy function by defining the vector of control points with regards to smoothness, gradient orientation and median intensity. The contour was initialized using circular Hough transform. Moreover, the contour points were grouped into edge point clusters and uncertain point clusters using a weighted k-means algorithm where the position of the contour points were updated automatically. This operation retains the edge points close to their original positions and updates the uncertain points to their correct positions. The overall accuracy of optic disc extraction was high but the authors reported the algorithm failure on the images having PPA as the energy function did not converge.

Joshi *et al.* [68] used a level-set approach in which a contour is represented by a zero-level-set of the Lipschitz function [106]. A good accuracy has been achieved based on appropriately selected initialization parameters, but the computational efficiency was low. Yu *et al.* made its fast implementation on the expense of accuracy by using region intensity information in level-set module. The method was applied on MESSIDOR [10] after blood vessel removal by morphological pre-processing.

ACM achieved higher accuracy in segmenting out optic disc as compared to Non-model-based approaches however, it was prone to error when a testing image involves any textural changes or atrophy associated with any retinal diseases around the optic disc boundary [69]. Moreover, since these techniques were applied in their local dataset therefore their robustness is questionable. Therefore, these techniques need to be

tested on public available databases in order to improve their generalization.

4) Statistical Shape Modeling Based Approach

Statistical shape modeling involves an offline training process in order to determine a shape model parameterizing the diverse of characteristics of the shape. In this category, Active Shape Modeling (ASM) has been explored for the extraction of optic disc boundary. ASM represents shape approximation of an object using a statistical-model. The ASM deforms to reflect the boundary shape of the optic disc in ways that are consistent with shapes presented in the training set.

Li and Chutatape [80] proposed the use of ASM to model the boundary of optic disc. They differentiated the optic disc edges from other edges on the basis of image gradient. They compared their results with the landmarks obtained from ophthalmologists using Mean Distance to the Closest Point (MDCP). Fengshou *et al.* [43] used minimum Mahalanobis distance from the mean profile vector to choose the best candidate point during the local edge search. Gradient information was added as a weight into the Mahalanobis distance function. They applied their shape deformation procedure on the image composed of weighted combination of the colour channels and evaluated their results with the benchmark using other evaluation measures as well along with MDCP. We constrained the search space by defining the search boundary on the image gradient for determining the edges of optic disc [56]. Restricting the search space on the image improved the results as compared to the original ASM. The method needs to be improved by reducing the blood vessel occlusion. Kim *et al.* [72] defined the imaginary circle after selecting ONH as brightest point. The random sample consensus technique [44] was applied in which the imaginary circle was first warped into a rectangle and then inversely warped into a circle to find the boundary of ONH. The shape warping was applied on the thresholded binary image in which boundary pixels were highly dependent on the thresholding value. The author predicted more accuracy after adding constraint conditions into the model selection of Random Sample Consensus (RANSAC).

The reason of Statistical shape modeling of not achieving higher segmentation accuracy is that there were less number of parameters trained during construction of training set. Most of the methods of optic disc extraction have been applied on red

channel. As far as PPA is concerned, it has higher discrimination with optic disc rim in green channel [97, 98] as well as blue channel [86]. In case of glaucoma, it is a challenging task to determine optic disc boundary in presence of PPA. Therefore, the training set of statistical shape modeling might include infomration from both red as well as green channel so as to distinguish between optic disc rim and the region outside optic disc including PPA. The information can include statistical measures, and even contour energy information in order to improve the segmentation accuracy. Moreover, reducing blood vessel occlusion can also aid to improve segmentation accuracy.

3.2.3 Optic Cup Extraction

Table 3.3: Results of different methods of optic cup extraction

Localization Method	Image Database	Colour Space	Image Dimension	Number of Test Images	Accuracy	Citation
Morphological approach						
Fuzzy C-means Clustering	Aravind Eye Hospital India	RGB space	1504 x 1000	20 Normal and 25 Glaucoma	91.7% CDR Correlation Coefficient	[20]
Morphological Operations	Kasturba Medical College India	8-bit RGB converted to Grayscale	560 x 720	24 Normal and 37 Glaucoma	90% Neural Network classification [116]	[99]
Level-set approach						
Vessel Kink Interpolation in 3D	Aravind Eye Hospital India	8-bit RGB	2896 x 1944	33 Normal and 105 Glaucoma	82% Overlapping Score	[68]
Gradient Vector Flow Modeling	ORIGA^{-light} [145]	8-bit RGB	3072 x 2048	94 Normal and 10 Glaucoma	90.85% CDR Correlation Coefficient	[134]
Blood Vessel Kinks Edge Detection	ORIGA^{-light} [145]	8-bit RGB	3072 x 2048	17 Normal and 10 Glaucoma	95.2% CDR Correlation Coefficient	[135]

After the segmentation of optic disc boundary, the next step is to find out the boundary of optic cup in order to determine the features such as CDR, neuroretinal rim loss etc for the diagnosis of glaucoma. Similar to boundary extraction of optic disc, ACM was used to determine the optic cup boundary and they also incorporated depth analysis to minimize the energy function with regards to intensity, smoothness and shape. Automatic extraction of optic cup boundary using 2D fundus image have also been proposed in the literature discussed as follows.

1) Morphology based Cup Segmentation

Nayak *et al.* [99] used morphological operations in the green channel of RGB images to segment optic cup (Figure 3.5(c)). As mentioned in Section 3.2.2, the results were used in order to classify between normal and glaucoma images after measuring CDR, Neuroretinal Rim Loss and vasculature shift. The classification accuracy is shown in Table 3.3. Babu *et al.* [20] applied Fuzzy C-means clustering on the Wavelet transformed green plane image after the removal of blood vessels. They compared the CDR values with those of Gold Standard obtained from the ophthalmologists. In both of the methods, the segmentation accuracy for the optic cup was not reported.

2) Level-Set Approach for Cup Boundary Detection

Wong *et al.* [134] proposed a level-set approach to represent the boundary of optic cup in the form of gradient flow equation. The gradient flow equation was initialized by a particular threshold value. The threshold value was selected according to higher 66.7% of the normalized cumulative intensity values of the image in green channel based on the fact that optic cup is more prominent in green channel. The boundary of the optic cup was smoothened by ellipse fitting. They applied the same approach on the red channel to obtain the optic disc boundary. Their later studies proposed the concept of blood vessel kinks at the edge of the optic cup for boundary extraction [135]. They used Canny edge detection and wavelet transform to determine the edges of the optic cup. The bending of blood vessels at the angle of more than 20 degrees were empirically determined to be at the edge of optic cup. Joshi *et al.* [68] used the same information of blood vessel kinks at the edge of optic cup to determine the optic cup boundary by interpolating the vessels kinks and the optic cup boundary in the 3rd dimension using spline interpolation. Clinical knowledge of ophthalmologists obtained from direct 3D cup examination was utilized to approximate the cup boundary.

Till date, very limited report on optic cup segmentation algorithms are available; and the results for the existing methods are preliminary. Since the edge between an optic disc and an optic cup is not usually visible in normal contrast of colour fundus images, therefore there is need to determine certain parameters which can distinguish between optic cup and optic disc. optic cup extraction may also require segmenting out vasculature structure and in-painting with neighborhood for accurate dimension

measurement.

3.2.4 Peripapillary Atrophy

Table 3.4: Results of different methods of the PPA localization / extraction

Extraction Method	Image Database Dimensions	Colour Space	Image	Number of Test Images	Accuracy	Citation
PPA detection						
Disc Difference Method	SCORM [111]	RGB converted to HSV space	800 x 800	20 Normal and 20 Glaucoma	95% within PPA	[123]
GLCM Based Texture Analysis	SCORM [111]	RGB converted to HSV space	800 x 800	20 Normal and 20 Glaucoma	92.5% within PPA	[77]
PPA extraction						
GLCM Based Texture Analysis	Gifu University Hospital Japan	8-bit RGB	1600 x 1200	26	73% LDA Segmentation Overlapping Score	[98]
Region Growing Technique	Lothian Birth Cohort Scotland	Blue channel of RGB	not reported	94	93% Overlapping Score	[86]

In this section, we review the automatic PPA detection and segmentation methods for diagnosing glaucoma discussed as follows:

1) PPA Localization

Tan *et al.* [123] detected PPA for determining pathological myopia. They proposed the variational level-set method [93] to extract the PPA boundary. The variational level-set method is initialized with a horizontal elliptical contour within optic disc boundary whereas a vertical elliptical contour is initialized outside the boundary. The horizontal elliptical contour is initialized in order to reduce the influence of the edges of the retinal vessels and allow the level-set function to grow and seek for the correct optic disc boundary. Conversely, a vertical elliptical contour is set externally as it best represents the physiological shape of the optic disc. The difference of these two optic discs is taken and thresholding in the HSV (Hue Saturation Value) colour space is used to roughly segment the PPA area. They claimed the PPA localization accuracy was 95% however, they did not consider the cases if PPA is present in both temporal and nasal sides. Moreover, no PPA segmentation was done. The test images were taken

from Singapore Cohort study Of the Risk factors for Myopia (SCORM) [111].The same authors [77] proposed a fusion of two decision methods. Gray Level Covariance Matrix (GLCM) based texture analysis was used to generate a degree of roughness which is then compared for the temporal side and nasal side. The higher degree of roughness in the temporal side compared to nasal side indicates PPA presence. Statistical analysis around the optic disc boundary, including average intensity and standard deviation were also used to detect PPA. However, like previous method, no PPA segmentation was performed.

2) PPA Extraction

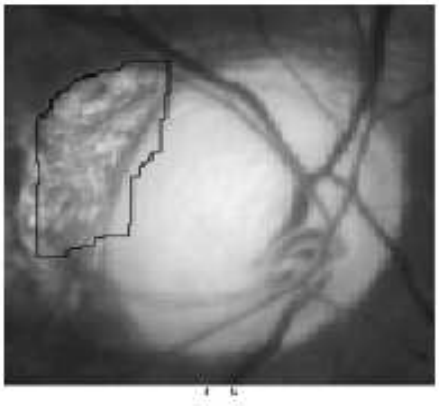

Figure 3.6: Example of PPA extraction [97, 98]

The statistical textural features, such as contrast, correlation, variance etc were determined in [97, 98] and a feature vector of 63 features was constructed. The PPA and non PPA pixel values were classified based on the feature vector. The training set was based on stereo images which were obtained by taking the retinal pictures of both normal and glaucoma patients from different angles in order make the 3D projection. The classification was performed using Linear Discriminant Analysis (LDA) [116]. The testing dataset consists of 58 glaucoma patients out of which 26 images have moderate to severe PPA. Lu *et al.* [86] extracted PPA using region growing on the blue channel after optic disc segmentation. They achieved the segmentation accuracy of 93%. An example is shown in Figure 3.6.

The PPA segmentation is an important step not only because it is one of main indications in glaucoma diagnosis but also it can improve the segmentation accuracy of optic disc if it is detected first. Therefore textural based properties can be used

in order to classify among optic disc region, PPA and other retinal areas. Moreover, there is need to use accurate classification algorithm which can distinguish among these regions.

3.3 Non-segmentation based Classification between Normal and Glaucomatous Retinal Images

Table 3.5: Results of different methods of non-segmentation based classification between normal and glaucomatous retinal images

Extraction Method	Image Database	Colour Space	Image Dimensions	Number of Test Images	Accuracy	Citation
Glaucoma Risk Index	Pattern Recognition Lab Germany	8-bit RGB	1600 x 1216	336 Normal and 239 Glaucoma [73]	80% on 5-fold cross validation (SVM)	[24]
Wavelet Coefficients	Kasturba Medical College India	8-bit RGB	560 x 720	24 Normal and 37 Glaucoma	93% on 10-fold cross validation (SMO)	[39]

Although there are few efforts made for the classification between normal and glaucomatous patients based on features that do not require segmentation of retinal structures, these methods can serve as prior knowledge for measuring different glaucomatous symptoms associated with retinal segmentation. Some of those methods are discussed as follows and their results are summarized in Table 3.5.

In non-segmentation based methods, Bock has made a major contribution [23, 24, 89]. Initially pixel intensity values were used on which PCA was applied [146] for dimensionality reduction. As a pre-processing step, they corrected illumination and intensity inhomogeneity then in-painted vasculature area after segmenting them out. Later on they added features such as image texture, FFT coefficients, histogram models, B-spline coefficients etc. Based on these features they calculated Glaucoma Risk Index (GRI). They used classifiers such as naive Bayes classifier, k-nearest neighbor classifier and Support Vector Machines (SVM) [116] to classify between healthy and glaucomatous images. They found SVM to be less prone to sparsely sampled feature space. Dua *et al.* [39] used wavelet-based energy features and compared the

performance of different classifiers including the previously mentioned classifiers, random forests [25] and Sequential Minimal Optimization (SMO) [71]. From SMO they obtained the maximum classification accuracy.

Unlike segmentation based methods, there are few methods available based on non-segmentation analysis for the retinal images associated with glaucoma. If they are used in conjunction with segmentation based methods, they can not only be quite effective in increasing the classification accuracy among different stages of glaucoma but also can serve as a benchmark for development of further automatic classification methods.

3.4 Automatic Retinal Disease Analysis on SLO Images

Apart from fundus images, some of the previous efforts suggest the automatic retinal disease analysis on SLO images. There are different types of SLO devices in the market with each one having its particular specifications in terms of retinal Field of View (FOV), grayscale value, resolution etc. An SLO image can be quite effective in determining the glaucoma related symptoms due to their high resolution [122]. Another report suggest the measurement of retinal vessel diameter in semi-automated analysis of retinal disease [96].

Among existing SLO devices, the SLOs manufactured by our collaborator, Optos have the largest FOV and becoming popular among retinal imaging devices with one of leading market shares in the USA [8]. Some of the previous methods for automatic retinal disease analysis have been applied on images of Optos manufactured SLO. Automatic vasculature segmentation and width measurement methods have also been applied on these images [104]. Another work suggest the application of post processing after vasculature segmentation [108] and automatic detection of retinal capillaries [148]. The retinal vasculature segmentation and width analysis is quite helpful in automatic analysis of many retinal and cardiovascular disease however, we need to determine methods for the automatic analysis of glaucoma related indications.

3.5 Discussion and Conclusion

Glaucoma causes changes in retinal structures which leads to peripheral vision loss if left untreated. The latest clinical information suggests observation of the ONH area and the retinal changes around it in order to diagnose glaucoma. Therefore after IOP measurement, the retinal exam is mostly based on measuring ONH related measurements such as optic disc size, optic cup size, their ratio, Neuroretinal Rim observation, PPA etc. It is very difficult to determine the optic cup boundary from 2-D retinal image as there is no sharp edge indicating it. Moreover, the occlusion of blood vessels make the extraction difficult of not only optic cup but also optic disc boundary which can become even tougher if PPA is present.

The survey has been categorized into two types of methods i.e. segmentation based methods and non-segmentation based methods. The methods which were applied on the same datasets are grouped together so as to present their results on a common benchmark. As far as segmentation based methods are concerned, they involve series of steps; each of which can be performed using the specific algorithm. It is important to observe the overall accuracy of each step from the ONH localization to extraction of boundaries of optic disc, optic cup and PPA which are needed to be high to ensure the effectiveness of the overall process maintained at a satisfactory level.

The ONH localization has been the initial step in determination of glaucoma as well as other retinal diseases such as Diabetic Retinopathy. The reason is that the ONH has been considered as the brightest region in the retinal image and therefore can serve as a way to locate other retinal structures. But, the presence of bright reflections in the retinal image brighter than ONH led to vasculature segmentation as all the retinal blood vessels converge in the ONH. The vasculature segmentation not only localized the ONH accurately but also the researchers who worked on optic disc and optic cup segmentation found comparatively accurate results after segmenting out retinal blood vessels. However, the accurate segmentation of vasculature structure has itself been a challenging task.

Current vasculature segmentation methods are mostly applied and therefore quite efficient on public datasets. These datasets are composed of healthy images and the images diseased with Diabetic Retinopathy which consists of small lesions and are

usually observed away of ONH. But they often segmented out PPA as well which is usually present in the images diseased with glaucoma. Based on our research, textural analysis could help to distinguish among the PPA and non PPA regions and incorporating them along with vasculature segmentation methods can increase their efficiency on glaucoma images. Moreover, accurate in-painting methods by neighborhood pixels after segmenting out vasculature structure can be used to remove blood vessel occlusion problem which can lead to accurate segmentation of optic disc and optic cup. 3-D scans obtained from modalities; such as OCT, can simplify the optic cup boundary detection problem but these modalities are not available in every hospital. Therefore we have to limit ourselves to 2-D scans.

Apart of image processing and computer vision based techniques, pattern recognition based methods have also been applied in order to locate and extract out the ONH boundary and optic cup. Statistical based parameters and design of accurate classifier will not only improve the results in terms of accuracy but also it will make the algorithms more robust and generalized. Huge diverse training data will significantly improve the classification efficiency. Another key issue in pattern recognition techniques is that there are few available public dataset of glaucoma based retinal images. Although there are contributions from some hospitals and research labs, there are not enough number of retinal images diseased with glaucoma as in the case of diabetic retinopathy. Since glaucoma progresses slowly and its symptoms occur gradually, therefore it is required to develop a retinal image database of different stages of glaucoma with annotations around different retinal structures associated with glaucoma. The database will serve as a benchmark to test and validate algorithms related to glaucoma based feature extraction. Since any of the single symptom mentioned earlier is not the guaranteed sign of glaucoma, the combination of all features is required for the accurate diagnosis. If the automatic methods are improved in terms of accuracy and generalization; they will serve as a benchmark for the clinicians to diagnose the disease based on measurements obtained by using those methods.

Chapter 4

Glaucoma Detection Framework - Rationale and Principles

4.1 Introduction

In this chapter we will present the overview of proposed *Glaucoma Detection Framework* (GDF). We will start our discussion with the brief explanation of benchmark used in this thesis. Then we will discuss about the overview of the GDF (Section 4.3 which involves rationale and principles used for the analysis and evaluation of different procedures of the GDF. The principles of analysis and evaluation include image-based feature generation and selection and evaluation metrics used for determination of performance of our algorithms.

4.2 Benchmark Retinal Image Database

To the best of our knowledge, there are a few public datasets are available from glaucoma patients and they have limited annotations [27, 49, 115]. This is shown in Table 4.1. According to it, RIM-ONE dataset is more suitable compared to other datasets but it has some limitations i.e. it does not have optic cup and vasculature annotations. Therefore the dataset from Pattern Recognition Lab, Erlangen Germany [74] is used for vasculature training and Drishti-GS is used for training optic cup. Besides, SLO images are not publicly available. In collaboration with Optos [8], who provided us images from their SLO, we need to find a way to automatically identify the

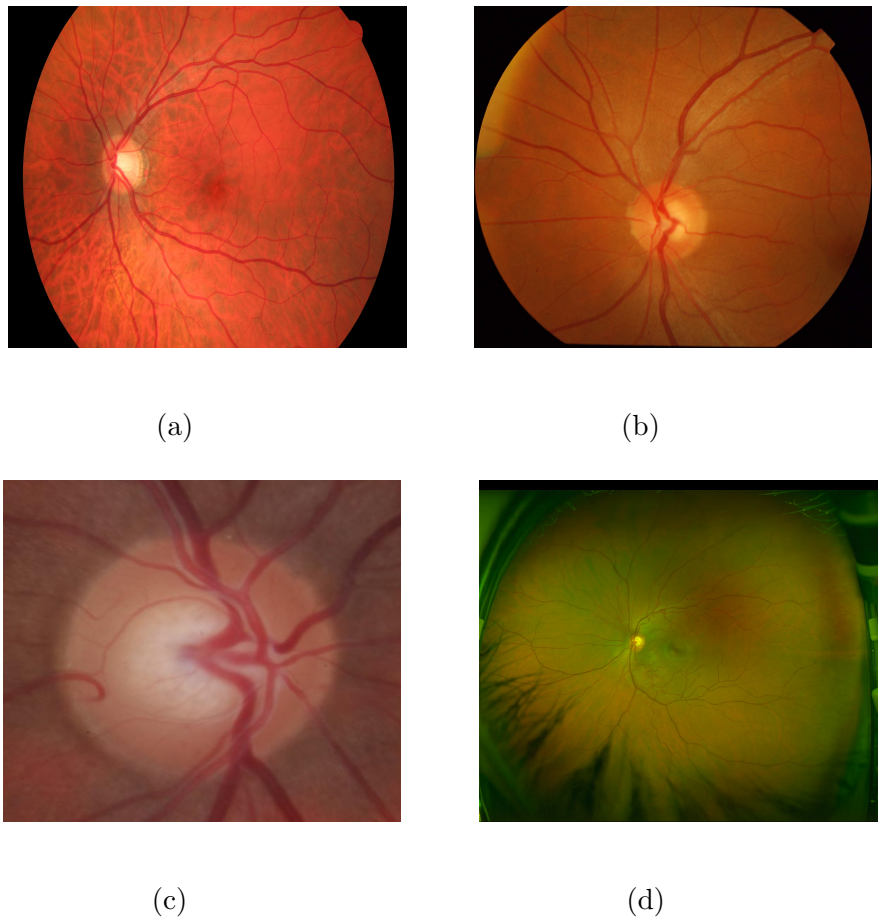

(a) (b)

(c) (d)

Figure 4.1: Examples of retinal images from each dataset (a) Pattern Recognition Lab, Erlangen(b) Drishti-GS (c) RIM-ONE and (d) Optomaps. RIM-ONE is the only dataset with the ONH images

features of glaucoma from images using the SLO images as well. Our methodology has been applied on different retinal image datasets; each one has different specifications. Some examples from each datasets are shown in Figure 4.1. Each database used in this thesis is discussed as follows:

4.2.1 Pattern Recognition Lab, Erlangen Germany

The public database of Pattern Recognition Lab, Erlangen (PRLE) [74] contains 15 images of healthy patients and 15 images of patients with diabetic retinopathy obtained using fundus camera. Each image has the FOV of 45° and annotated with vasculature area. Each image has the resolution of 3504 x 2336 pixels. This database has been used for vasculature segmentation training and validation. An example of ground truth from the dataset has been shown in Figure 4.2(a).

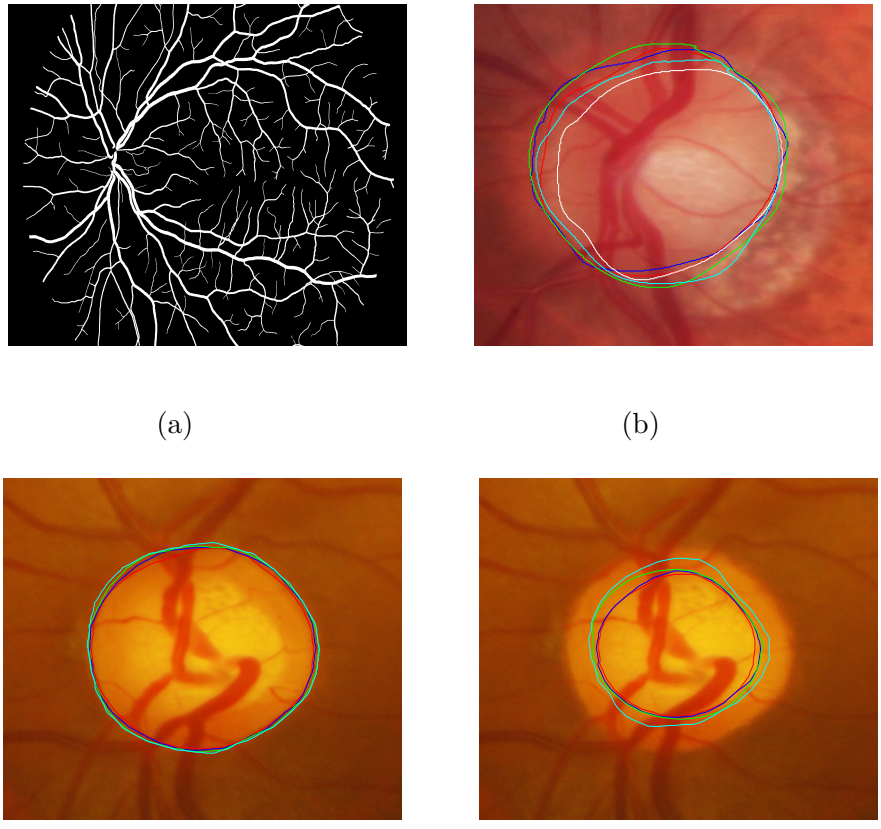

(a) (b)

(c) (d)

Figure 4.2: Examples of ground truth from (a) Pattern Recognition Lab, Erlangen on vasculature area (b) RIM-ONE around optic disc (c) Drishti-GS around optic disc and (d) Drishti-GS around optic cup. The annotation with different colours represent the annotations from differennt experts.

Table 4.1: Annotation of retinal image datasets

Annotation	Pattern Recognition Lab	RIM-ONE	Drishti-GS	Optomaps
Vasculature mask	X			X
Optic Disc Annotation		X	X	X
Optic Cup Annotation			X	X
Glaucoma vs Healthy		X		X

Table 4.2: Inter-observer variability in the dataset

Expert X vs Expert Y	All images	Normal images	Glaucoma images
1 vs 2	3.71% ± 1.99%	3.92% ± 2.00%	3.48% ± 2.00%
1 vs 3	3.94% ± 1.51%	4.25% ± 1.47%	3.26% ± 1.47%
1 vs 4	2.93% ± 2.09%	3.16% ± 2.27%	2.58% ± 1.60%
1 vs 5	2.40% ± 1.40%	2.45% ± 1.36%	2.38% ± 1.60%
2 vs 3	2.64% ± 1.48%	2.79% ± 1.61%	2.36% ± 1.12%
2 vs 4	5.24% ± 3.43%	5.76% ± 3.69%	4.27% ± 2.45%
2 vs 5	4.46% ± 2.69%	4.71% ± 2.83%	4.02% ± 2.29%
3 vs 4	5.25% ± 2.56%	5.82% ± 2.66%	4.01% ± 1.87%
3 vs 5	4.61% ± 2.04%	4.95% ± 2.11%	3.75% ± 1.64%
4 vs 5	2.69% ± 1.72%	2.95% ± 1.89%	2.08% ± 1.01%

4.2.2 RIM-ONE (An Open Retinal Image Database for Optic Nerve Evaluation)

RIM-ONE [49] dataset is based on the ONH images. An example has been shown in Figure 4.1(c). Therefore we don't need to apply the ONH localization algorithm on the RIM-ONE dataset images. These retinographs have been captured in the three hospitals cited before which are located in different Spanish regions. Compiling images from different medical sources guarantee the acquisition of a representative and heterogeneous image set. All the retinographs are non-mydriatic retinal photographs captured with specific flash intensities, thus avoiding saturation. It has 158 images with 118 normal and 40 glaucoma images. The images have variable resolution ranging from 300 to 900 both sides. Each image has been annotated around optic disc by 5 experts; 4 ophthalmologists and 1 optometrist. An example ground truth of optic disc annotation in RIM-ONE is shown in Figure 4.2(b). The average inter-observer variability among these experts has been shown in Table 4.2. The inter-observer variability for a particular image has been calculated by determining degree of overlap of the optic disc mask obtained by annotation from each expert and then performing the comparison among them. The degree of overlap has been calculated using Dice Coefficient [37] (explained in Section 4.4.3). The inter-observer variability shows high similarity among optic disc annotations.

Table 4.3: Inter-observer variability of optic disc and optic cup

Expert X vs Expert Y	Optic disc	Optic cup
1 vs 2	1.00% ± 0.39%	1.47% ± 0.83%
1 vs 3	1.87% ± 0.61%	3.07% ± 1.57%
1 vs 4	2.99% ± 1.35%	5.31% ± 2.10%
2 vs 3	0.84% ± 0.27%	1.57% ± 0.94%
2 vs 4	1.96% ± 1.20%	3.81% ± 1.61%
3 vs 4	1.09% ± 1.02%	2.22% ± 1.25%

4.2.3 Drishti-GS

Drishti-GS dataset consists of a total of 50 images [115] (Figure 4.1(b)). The main purpose of including the dataset in our study is to obtain the optic cup annotations. All the images have been marked by 4 eye experts with varying clinical experience. All images are collected at Aravind Eye Hospital, India. Selected patients are between 40-80 years of age with roughly equal number of males and females. The data collection protocol is as follows.

- All images are taken centered on optic disc with a field-of-view(FOV) of 30-degrees and of dimensions 2896 X 1944 pixels and PNG uncompressed image format.
- Ground truth (Table 4.1) is collected from data experts with varying clinical experience of 3,5,9 and 20 years respectively.
- For the ground truth collection a dedicated marking tool is created to allow for precise boundary marking.

The Drishti-GS dataset has high similarity among optic disc as well as optic cup annotations as shown in Table 4.3. An example around optic disc and cup annotations has been shown in Figure 4.2 (c) and (d) respectively. The example images has been shown after cropping out the ONH area.

4.2.4 Optomaps

The Optomaps have been obtained from Optos [8] and are acquired using their ultra-wide field SLO. Each image has a FOV of up to 200 degrees of the retina at resolution

14 μm. The device captures the retinal image without dilation, through a small pupil of 2 mm. The image has two channels: red and green. The green channel (wavelength: 532nm) provides information about the sensory retina to retinal pigment epithelium whereas the red channel (wavelengh: 633nm) shows deeper structures of the retina towards the choroid. Each image has a dimension of 3900×3072 and each pixel is represented by 8-bit on both red and green channels. There are two datasets of Optomaps. The first dataset is composed of 104 retinal images which are either healthy or diseased with diabetic retinopathy due to which they have lesions on the retina. The main purpose of including this dataset is to design retinal area detection framework (Section 5.2). The second dataset is composed of 51 healthy and 51 diseased retinal images. The diseased retinal images have been obtained from the diabetes patients with the suspect of glaucoma. The healthy retinal images have been annotated around optic disc and vasculature structure whereas diseased retinal images have been annotated around optic disc and optic cup.

4.3 The Glaucoma Detection Framework

The block diagram of the GDF is shown in Figure 4.3. The GDF is initiated by pre-processing stage needed for the ONH analysis. The pre-processing stage includes retinal area detection, the ONH localization and vasculature segmentation. Since most of the retinal symptoms associated with glaucoma are related to the ONH, therefore the localization of the ONH is the first step towards the automatic analysis of glaucoma. Although one of the retinal image dataset has ONH localized images, the other retinal image datasets need to be ONH localized. Vasculature segmentation is included in pre-processing stage as its features are calculated required for optic disc and optic cup segmentation. Also, vasculature segmentation is required for calculating the vasculature shift. After pre-processing stage, we obtain the ONH image i.e. the image with the ONH area as the main object. The next step is for optic disc and optic cup segmentation for calculating changes in the ONH structures associated with glaucoma such as the CDR, neuroretinal rim loss etc. After segmentation of optic disc and cup, we calculate regional image features to extract image-based information (e.g. textural, spatial and frequency based information) of the ONH image. Finally, we performed

classification between normal and glaucoma images using both regional image feature information and geometrical measure information.

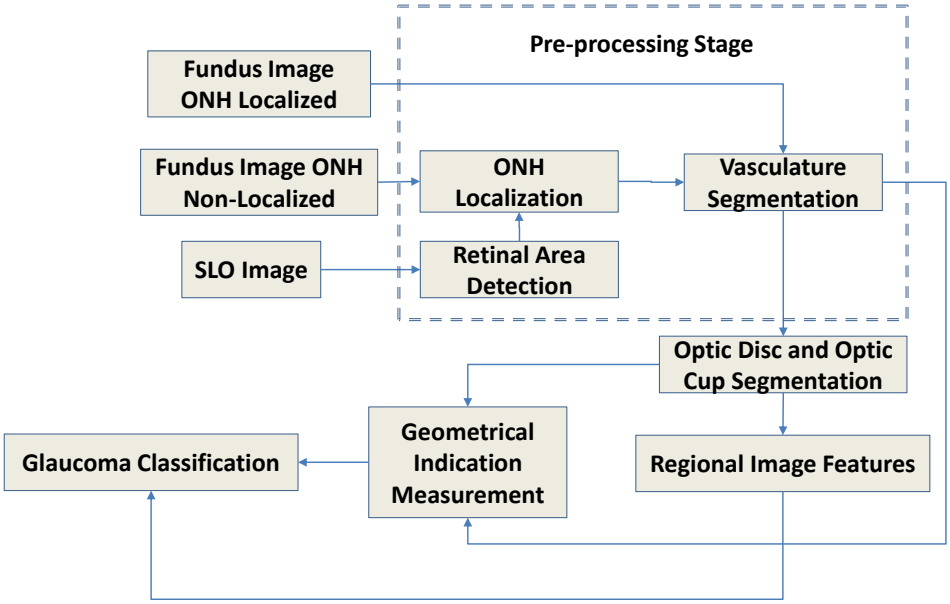

Figure 4.3: Block diagram of the Glaucoma Detection Framework (GDF)

4.4 Analysis and Evaluation of the GDF

In this section, we will discuss about analysis and evaluation of different stages of the GDF. It includes benchmarking, feature generation, feature selection and evaluation. Therefore, we are discussing following points in the following sections.

- Generation of Image-based Features
- Feature Selection Methods
- Evaluation Metrics
- Machine Used for Experimentation

4.4.1 Generation of Image-based Features

In this thesis, the retinal scans are analyzed and evaluated using image-based features. These features are used to distinguish among different retinal structures. In order to determine the features most relevant to the classification, feature selection techniques have also been applied (Section 4.4.2). Also the segmentation results obtained after classification are evaluated against the annotations obtained from the clinicians.

We intend to segment out different retinal structures by differentiating in terms of textural, regional, grayscale-gradient, Gabor and biologically inspired features. Textural and regional features can be calculated for the small sub-regions called superpixels (Section 5.2.4). The gradient, Gabor and biologically inspired features can also be calculated for each pixel. Textural and gradient based features are calculated from red and green channels so as to accommodate their image response in the training set after blurring. For determining features at different smoothing scales, both red and green channels of images are convolved with the Gaussian at different scales [14] . In an SLO image, the blue channel is set to zero therefore no feature is calculated for the blue channel.

1) Textural Features

Texture can be analyzed using Haralick features [58] obtained by Grey Level Co-occurrence Matrix (GLCM) analysis. GLCM determines how often a pixel of a grey value i occurs adjacent to a pixel of the grey value j. Four angles are used for observing the pixel adjacency i.e. $\theta = 0°, 45°, 90°, 135°$. These directions are shown in Figure. 4.4(a). GLCM also needs an offset value **D** which defines pixel adjacency by certain distance. Figure. 4.4(b) illustrates the process of creating GLCM using the image **I** with $\theta = 0°$ for observing pixel adjacency. As an example, 1 and 1 in image **I** are are adjacent to each other at $\theta = 0°$ only once, therefore the value at GLCM at position (1,1) is 1. Similarly, 1 and 2 in **I** occur twice at $\theta = 0°$, therefore the value in GLCM at (1,2) is 2. The features, which are calculated using the GLCM matrix are summarised in Table 4.4. The mean value in each direction was taken for each Haralick feature and they are calculated from both red and green channels.

Table 4.4: Textural features extracted using GLCM

Feature Name	Equation	Definition
Autocorrelation	$acorr = \sum_i \sum_j ijp(i,j)$	Linear dependence in GLCM between same index
Cluster Shade	$C_{shade} = \sum_i \sum_j (i + j - \mu_x - \mu_y)^3 p(i,j)$	Measure of skewness or non-symmetry
Cluster Prominence	$C_{prom} = \sum_i \sum_j (i + j - \mu_x - \mu_y)^4 p(i,j)$	Show peak in GLCM around the mean for non-symmetry
Contrast	$con = \sum_{i=1}^{N_g} \sum_{j=1}^{N_g} \lvert i-j \rvert^2 p(i,j)$	Local variations to show the texture fineness.
Correlation	$corr = \frac{\sum_i \sum_j (ij)p(i,j) - \mu_x \mu_y}{\sigma_x \sigma_y}$	Linear dependence in GLCM between different index
Difference Entropy	$H_{diff} = -\sum_{i=0}^{N_g-1} p_{x-y} log(p_{x-y}(i))$	Higher weight on higher difference of index entropy value
Dissimilarity	$diss = \sum_i \sum_j \lvert i-j \rvert p(i,j)$	Higher weights of GLCM probabilities away from the diagonal
Energy	$E = \sum_i \sum_j p(i,j)^2$	Returns the sum of squared elements in the GLCM
Entropy	$H = -\sum_i \sum_j p(i,j) log(p(i,j))$	Texture randomness producing a low value for an irregular GLCM
Homogeneity	$homom = \sum_i \sum_j \frac{1}{1+(i-j)^2} p(i,j)$	Closeness of the element distribution in GLCM to its diagonal
Information Measures 1	$IM_1 = (1 - exp[-2.0(H_{xy} - H)])^{0.5}$	Entropy measures
Information Measures 2	$IM_2 = \frac{Entropy - H_{xy2}}{\mathrm{MAX}(H_x, H_y)}$	Entropy measures
Inverse Difference Normalized	$IDN = \sum_i \sum_j \frac{p(i,j)}{1 + \frac{\lvert i-j \rvert}{N_g}}$	Inverse Contrast Normalized
Inverse Difference Moment Normalized	$IDMN = \sum_i \sum_j \frac{p(i,j)}{1 + \frac{(i-j)^2}{N_g}}$	Homogeneity Normalized
Maximum Probability	$Pr_{max} = \max_{(x,y)} p(i,j)$	Maximum value of GLCM
Sum average	$\mu_{sum} = \sum_{i=2}^{2N_g} i p_{x+y}(i)$	Higher weights to higher index of marginal GLCM
Sum Entropy	$H_{sum} = -\sum_{i=2}^{2N_g} p_{x+y} log(p_{x+y}(i))$	Higher weight on higher sum of index entropy value
Sum of Squares: Variance	$\sigma_{sos} = \sum_i \sum_j (i-\mu)^2 p(i,j)$	Higher weights that differ from average value of GLCM
Sum of Variance	$\sigma_{sum} = \sum_{i=2}^{2N_g} (i - H_{sum}) p_{x+y}(i)$	Higher weights that differ from entropy value of marginal GLCM

(i,j) represent rows and columns respectively, N_g is number of distinct grey levels in the quantised image, μ_x and μ_y are mean values of GLCM across x-axis and y-axis respectively, μ is mean of the GLCM matrix, $p(i,j)$ is the element from normalized GLCM matrix $p_x(i)$ and $p_y(j)$ are marginal probabilities of matrix obtained by summing rows and columns of GLCM respectively i.e. $p_x(i) = \sum_{j=1}^{N_g} p(i,j)$, $p_y(j) = \sum_{i=1}^{N_g} p(i,j)$, $p_{x+y}(k) = \sum_{i=1}^{N_g} \sum_{j=1}^{N_g} p(i,j), k = i + j - 1 = 1, 2, 3, ..., 2N_g$ and $p_{x-y}(k) = \sum_{i=1}^{N_g} \sum_{j=1}^{N_g} p(i,j), k = \lvert i-j \rvert + 1 = 1, ..., N_g$, H_x and H_y and entropies of p_x and p_y respectively, $H_{xy} = -\sum_i \sum_j p_x(i) p_y(j) log(p_x(i) p_y(j))$, $H_{xy2} = -\sum_i \sum_j p(i,j) log(p_x(i) p_y(j))$

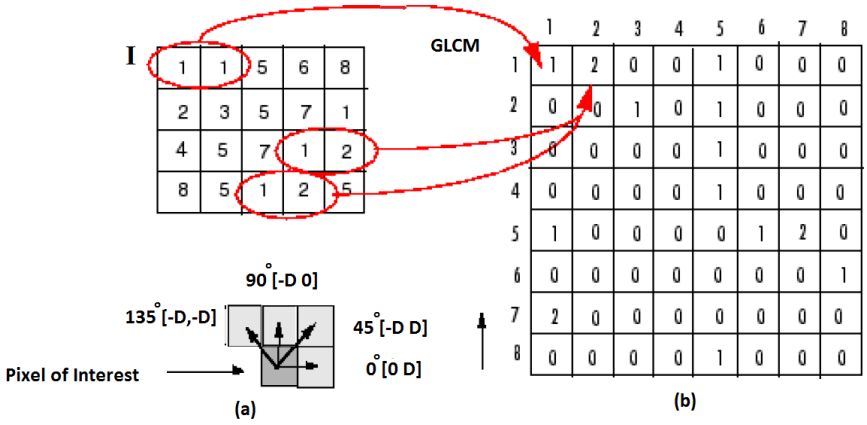

Figure 4.4: (a) GLCM directions and offset (b) GLCM process using image **I** [57].

2) Gradient Features

In order to calculate these features, the response from Gaussian filter bank [14] is calculated. The Gaussian filter bank includes Gaussian $\mathcal{N}(\sigma)$, its two first order derivatives $\mathcal{N}_x(\sigma)$ and $\mathcal{N}_y(\sigma)$ and three second order derivatives $\mathcal{N}_{xx}(\sigma)$, $\mathcal{N}_{xy}(\sigma)$ and $\mathcal{N}_{yy}(\sigma)$ in horizontal(x) and vertical(y) directions. Lindeberg and Frangi introduced Gaussian based features which are mostly applicable for vasculature detection [47, 81]. These are tabulated in Table 4.5.

3) Gabor Features

Gabor filters serve as frequency based filters and being used for image segmentation [34]. For extracting features, we applied the following equations:

$$Gb(x, y, \theta, f, \sigma_x, \sigma_y) = \exp(-\frac{1}{2}(\frac{\hat{x}^2}{\sigma_x^2} + \frac{\hat{y}^2}{\sigma_y^2})) * \exp(i2\pi f x) \tag{4.1}$$

$$\hat{x} = xcos\theta + ysin\theta \tag{4.2}$$

$$\hat{y} = ycos\theta - xsin\theta \tag{4.3}$$

x and y are image pixel coordinates.

4) Biologically Inspired Features

The biologically inspired features are inspired by the process of visual cortex of human brain in image recognition tasks. Here the retinal image is filtered in a number of

Table 4.5: Gaussian based features

Feature Name	Equation	Explanation
Gamma-normalized derivative	$L_{pp,\gamma-norm} = \frac{\sigma^\gamma}{2}(\mathcal{N}_{xx} + \mathcal{N}_{yy} - \sqrt{(\mathcal{N}_{xx} - \mathcal{N}_{yy})^2 + 4\mathcal{N}_{xy}{}^2})$	$\frac{\sigma^\gamma}{2}$ is normalization factor with $\gamma = \frac{3}{2}$
	$L_{qq,\gamma-norm} = \frac{\sigma^\gamma}{2}(\mathcal{N}_{yy} + \mathcal{N}_{yy} + \sqrt{(\mathcal{N}_{xx} - \mathcal{N}_{yy})^2 + 4\mathcal{N}_{xy}{}^2})$	$\sigma = [\sqrt{(2)}, 2, 2\sqrt{(2)}, 4]$ are the Gaussian scale values
Gamma-normalized absolute principal curvature	$M_{\gamma-norm} = max(\lvert L_{pp,\gamma-norm}\rvert, \lvert L_{qq,\gamma-norm}\rvert)$	
Vesselness measure	$\nu_0 = \begin{cases} 0\,(\lambda_2 > 0) \\ exp(-\frac{R_B{}^2}{2\beta^2})(1 - exp(-\frac{S^2}{2c^2})) \\ (otherwise) \end{cases}$	λ_1, λ_2 are eigen values of $H = \begin{bmatrix} \mathcal{N}_{xx} & \mathcal{N}_{xy} \\ \mathcal{N}_{yx} & \mathcal{N}_{yy} \end{bmatrix}$ $R_B = \frac{\lambda_1}{\lambda_2}$, $\beta = 0.5$ [47], $S = \sqrt{\mathcal{N}_{xx}{}^2 + \mathcal{N}_{yy}{}^2 + 2\mathcal{N}_{xy}{}^2}$ $c = \frac{max(S)}{2}$
Lindeberg Ridges	$ML = max(\lvert L_{pp}\rvert, \lvert L_{qq}\rvert)$	
	$N_{\gamma-norm}(L) = (L_{pp,\gamma-norm}{}^2 - L_{qq,\gamma-norm}{}^2)$	
	$A_{\gamma-norm}(L) = (L_{pp,\gamma-norm} - L_{qq,\gamma-norm})^2$	
Staal Ridges	$\rho(Pix, \sigma) = -\frac{1}{2}\lvert sign(\bigtriangledown\mathcal{N}_{x,y}(Pix + \vec{v}, \sigma).\vec{v}) - sign(\bigtriangledown\mathcal{N}_{x,y}(Pix - \vec{v}, \sigma).\vec{v})\rvert$	$Pix = I(x, y)$, $\vec{v}$=eigen vector of largest eigen value, $\mathcal{N}_{x,y}$=Gaussian in x and y directions
Differential Geometric Edge Definition	$L_{uu} = \mathcal{N}_{xx} + \mathcal{N}_{yy}$	(u, v) are local coordinate system [81]
	$L_{u,u} = \mathcal{N}_x{}^2 + \mathcal{N}_y{}^2$	
	$L_{uv} = \mathcal{N}_x{}^2\mathcal{N}_{xx} + 2\mathcal{N}_{xy}\mathcal{N}_x\mathcal{N}_y + \mathcal{N}_y{}^2\mathcal{N}_{yy}$	

low-level visual 'feature channels' at multiple spatial scales, for features of colour, intensity, flicker etc. It consists of 6 feature maps of intensity units I and 12 colour units representing neuronal working of mammals [62]. The colour units have 4 different colour channels representing excitation as well as inhibition of colours. The excitation and inhibition of different colours make two pairs. They are formed as red-green (R-G) and blue-yellow (B-Y).

By using dyadic Gaussian pyramids [17] convolved on the intensity channel of an input colour image, nine spatial scales are generated with a ratio from 1:1 (scale 0) to 1:256 (scale 8). To get intensity feature maps, the centre-surround [121] operation is performed between centre levels and surround levels. Centre-surround operation is the absolute difference of an image at centre scale c and surround scale s. The centre-surround operation at different intensity and colour units has been shown as:

$$I(c, s) = \lvert I(c) - Interp_{s-c}I(s)\rvert \tag{4.4}$$

$$RG(c,s) = |(R(c) - G(c)) - Interp_{s-c}(R(s) - G(s))| \tag{4.5}$$

$$BY(c,s) = |(B(c) - Y(c)) - Interp_{s-c}(B(s) - Y(s))| \tag{4.6}$$

where $Interp_{s-c}$ represent interpolation to $s - c$ level.

Using centre levels (c=2,3,4) and surround levels ($s = c + d$ with d=3,4), six feature maps are computed at levels of 2-5, 2-6, 3-6, 3-7, 4-7, and 4-8. Because scales are different between center levels and surround levels, maps of surround levels are interpolated to the same size as the corresponding center levels, and then they are subtracted point-by-point from the corresponding center levels to generate the relevant feature maps.

5) Regional Features

These features are used to define regional attributes and are applicable when image is divided into different sub-regions (Section 5.2.4) for analysis. Table 4.6 represents the features describing regional attributes.

Table 4.6: Regional features

Feature Name	Equation	Definition
Mean Intensity	$I_\mu = \frac{\sum_i \sum_j I_s(i,j)}{N_s}$	Mean value of region
Area	N_s	Number of pixels in region
Convex Area	N_{sc}	Number of pixels in convex area of region. Convex area is the polygon representing the region with all interior angles less than 180°
Extent	$Ext = \frac{N_s}{N_{sb}}$	Ratio of total number of pixels in the region to number of pixels in the bounding box
Orientation	θ_s	Region angle with respect to x-axis
Solidity	$Sol = \frac{N_s}{N_{sc}}$	Ratio of number of pixels in the region to convex area

4.4.2 Feature Selection Method

The main purposes for feature selection are reducing execution time and dimensionality reduction by selecting features most relevant to the particular retinal structure determination. For feature selection, we have selected following approaches:

1) Sequential Feed-forward Selection Approach

In the Sequential Feed-forward Selection (SFS) approach, the interaction among features is taken into account. From the available set of features, the feature with the highest *Area Under the Curve* (AUC) [113] is selected. The next feature is chosen in such a way that when it is used along with the first selected feature, it will give the highest AUC compared to other non-selected features. The process is repeated until there is little improvement (less than 0.01) or no improvement in the AUC.

2) Filter Approach

In the Filter approach, the features are ranked with respect to their effectiveness in classification. In order to determine most relevant features, an Independent Evaluation Criterion (IEC) for binary classification is used [82]. In IEC, the classification performance of each feature is calculated individually according to AUC [113].

3) Filter and SFS Approach

The 'Filter and SFS' approach is similar to SFS approach except that it is applied on the filtered feature set rather than complete feature set.

4.4.3 Evaluation Metrics

1) Dice Coefficient

The Dice Coefficient evaluates the degree of overlap of two regions and is used to determine the extent to which the segmented objects match. It is defined as:

$$D(A, B) = \frac{2|A \cap B|}{|A \cup B|}, \tag{4.7}$$

where A and B are the segmented regions surrounded by model boundary and annotations from the ophthalmologists respectively, $\cap$ denotes the intersection and $\cup$

denotes the union. Its value varies between 0 and 1 where a higher value, indicates an increased degree of overlap.

2) Receiver Operating Characteristics and Area Under the Curve

A receiver operating characteristic (ROC), or ROC curve, is a graphical plot that illustrates the performance of a binary classifier system as its discrimination threshold is varied. The curve is created by plotting the true positive rate against the false positive rate at various threshold settings. For a binary classifier, true positive rate (*Sensitivity*) is the proportion of class-1 test examples (pixels, superpixels or images) correctly identified. It can be illustrated as:

$$Sensitivity = \frac{TP}{TP + FN} \tag{4.8}$$

where TP is number of class-1 test examples correctly identified and FN is number of class-1 test examples misidentified. Similarly false positive rate (*Specificity*) is the proportion of class-0 test examples correctly identified. It can be illustrated as:

$$Specificity = \frac{TN}{TN + FP} \tag{4.9}$$

where TN is number of class-0 test examples correctly identified and FP is number of class-0 test examples misidentified. The area under th ROC is called *Area Under the Curve* or AUC. The overall accuracy [18] can be calculated as

$$Accuracy = \frac{TN + TP}{TN + TP + FN + FP} \tag{4.10}$$

AUC is measured so as to determine classification power of the classifier.

4.4.4 Machine Used for Experimentation

Our all experimentation has been performed on a PC with Intel Core i7-2600 CPU with 16GB DDR3-1333 RAM.

4.5 Conclusion

In this chapter we have outlined the proposed GDF and discussed the rationale and principles of analysis and evaluation procedures of the GDF. These principles include feature generation, feature selection and evaluation metrics. These principles would be followed in the upcoming chapters. In order to evaluate the methods we have proposed towards the development of GDF, we have the datasets from different fundus and SLO images. These datasets have been annotated by different eye clinicians around glaucoma related anatomical structures such as optic disc or optic cup. Based on our evaluation, there is high inter-observer similarity among different clinicians in particular dataset. This can also lead to determine the mean of the annotations on the particular image which can be used to train our algorithms. This has been discussed in the upcoming chapters.

Chapter 5

Retinal Image Pre-Processing

5.1 Introduction

In this chapter we will discuss the proposed methods for the pre-processing stage needed to analyze the ONH. This includes determination of true retinal area, ONH localization, and vasculature segmentation. As shown in Figure 5.1(a), the determination of true retinal area in fundus images is quite straight forward i.e. we just need to threshold out dark background. On the other hand, we need to find methods to classify true retinal area and artefacts present in Optomaps (SLO images). The ONH localization algorithm can run properly on SLO images only if true retinal area has been segmented out. After the ONH localization, we need to segment out vasculature area. Therefore, our discussion will start from retinal area detection in Optomaps followed by the ONH localization and vasculature area segmentation.

5.2 Retinal Area Detection

The 2D retinal scans obtained from SLO may contain structures other than the retinal area; collectively regarded as artefacts. Exclusion of artefacts is important as a pre-processing step before automated detection of features of retinal diseases. In a retinal scan, extraneous objects such as the eyelashes and eyelids may appear bright and in focus. Therefore, automatic segmentation of these artefacts from an imaged retina is not a trivial task. The purpose of performing this study is to develop a method that can exclude artefacts from the retinal scans so as to improve automatic detection of

disease features from the retinal scans.

The SLO manufactured by Optos [8] produces images of the retina with a width of up to 200 degrees (measured from the centre of the eye). This compares to 45-60 degrees achievable in a single fundus photograph. Examples of retinal imaging using fundus camera and SLO are shown in Figure. 5.1. Due to the wide FOV of SLO images, structures such as eyelashes, eyelids are also imaged along with the retina. The true retinal area has been outlined in Figure 5.1 (b) with blue colour. The structures outside the outline are artefacts. If these structures are removed, this will not only facilitate the effective analysis of the retinal area, but also enable registering multi-view images into a montage to assist disease diagnosis.

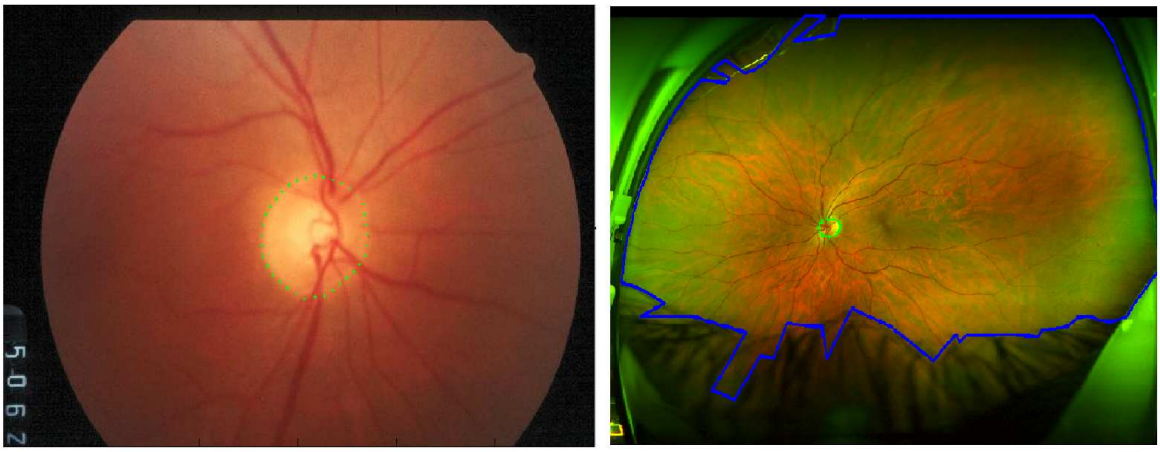

Figure 5.1: An example of (a) a fundus image and (b) an SLO image annotated with true retinal area and the ONH

In this work, we have constructed a novel framework for the extraction of retinal area in SLO images. For differentiating between the retinal area and the artefacts, we have determined different image-based features which reflect grayscale and textural information at multiple resolutions. Then we have selected the features among the large feature set which are relevant to classification. The feature selection process improves the classifier performance in terms of computational time. Finally, we have constructed the classifier for discriminating between the retinal area and the artefacts. Our prototype has achieved average classification accuracy of 92% on the dataset having healthy as well as diseased retinal images.

5.2.1 Background

In an image obtained from the SLO, the eyelashes show as either dark or bright region compared to retinal area depending upon how the laser beam is focused as it passes through the eyelashes. The eyelids show as a region with greater reflectance compared to the retinal area. Therefore, we need to find features which can differentiate among true retinal area and the artefacts in SLO retinal scans. After visual observation in Figure. 5.1(b), the features reflecting the textural and structural difference could have been the suggested choice. In previous work, these features have been calculated for different regions in fundus images; mostly for quality analysis [35, 36, 105, 142].

In previous work, the representation of retinal images was performed in terms of image features such as intensity, skewness, textural analysis, histogram analysis and sharpness [35, 55, 142]. Dias *et al.* [36] determined four different classifiers using four types of features. They were analyzed for the retinal area including colour, focus, contrast and illumination. The output of these classifiers was concatenated for quality classification. Apart from calculating image features for a whole image, grid analysis containing small patches of the image has also been proposed for reducing computational complexity [35]. For determining image quality, the features of Region of Interest (ROI) of anatomical structures such as Optic Nerve Head (ONH) and Fovea have also been analyzed [105]. These features included structural similarity index, area or visual descriptor. Some of the above mentioned techniques suggest the use of grid analysis which can be time-effective method since features are generated for each square in the grid rather than for each pixel. However, grid analysis might not be an accurate way to represent irregular regions in the image. Therefore, we opted for the use of superpixels [15, 95, 128, 129] which group pixels into different image dependent regions depending upon their regional size and compactness.

5.2.2 Retinal Area Detection Method

In the proposed method of the retinal area detector, we will follow the classification approach as shown in Figure 5.2. The method is based on following steps:

- Gamma adjustment
- Superpixels Generation

- Ground Truth Determination
- Feature Generation and Selection
- Classifier Construction

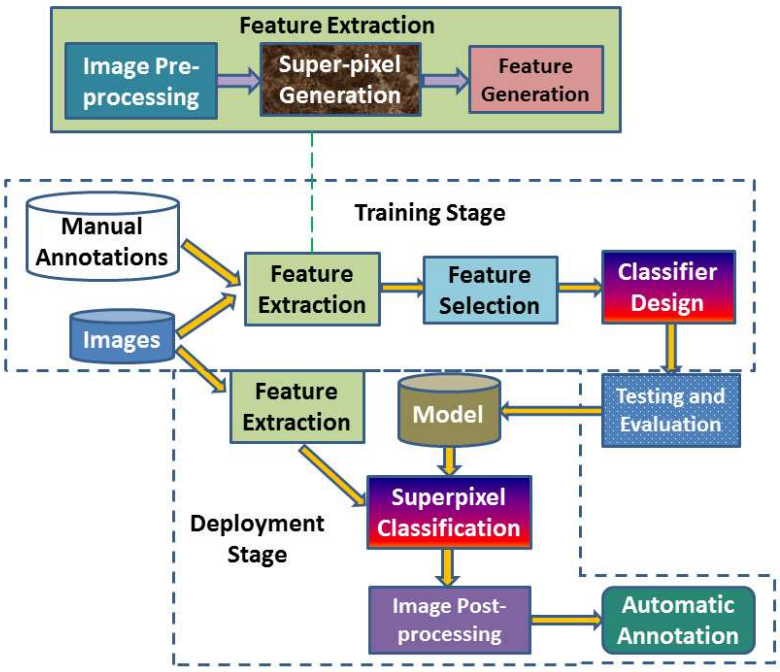

Figure 5.2: Block diagram of retina detector framework

5.2.3 Gamma Adjustment

The SLO images are initially of very low contrast to be visualized. Also there might be variation among different images due to device light exposure variations etc. In order to visualize the SLO images as well as maintain all the images at same mean intensity, they are normalized by applying a Gamma (γ) adjustment to bring the mean image intensity to a target value. γ was calculated using

$$\gamma = \frac{\log_{10}(\mu_{target}) - \log_{10}(255)}{\log_{10}(\mu_{orig}) - \log_{10}(255)} \tag{5.1}$$

where μ_{orig} is mean intensity of the original image and μ_{target} is mean intensity of the target image. For image visualization, μ_{target} is set to 80 as image contrast below 80 was quite low to image was quite bright beyond this value which might be an issue

in determining features for distinguishing between artefacts and retinal area. Finally, the Gamma adjustment of the image is given by Equation (5.2).

$$I_{norm} = (\frac{I}{255})^{\gamma}, \tag{5.2}$$

5.2.4 Generation of Superpixels

A retinal scan obtained from the SLO has the resolution of 3900 x 3072. Therefore the calculation of features for each pixel which need the neighborhood information (e.g. textural features) would be quite computationally inefficient. Therefore, we propose analyzing the SLO image-based features calculated for a small region in the retinal image called superpixels. The determination of the feature vector for each superpixel is computationally efficient as compared to feature vector determination for each pixel. The superpixels from the images in the training set are assigned the class of either retinal area or artefacts depending upon the majority of pixels in the superpixel belonging to the particular class. The classification is performed after ranking and selection of features in terms of effectiveness in classification.

The superpixel algorithm groups pixels into different regions, which can be used to calculate image features while reducing the complexity of subsequent image processing tasks as shown in Figure 5.3. Superpixels capture image redundancy and provide a convenient primitive image pattern. As far as fundus retinal images are concerned, the superpixels have been generated for the analysis of anatomical structures [32] and retinal hemorrhage detection [124]. For retinal hemorrhage detection, the superpixels were generated using watershed approach [109] but the number of superpixels generated in our case need to be controlled. The watershed approach sometimes generates number of superpixels of the artefacts more than desired. The superpixel generation method used in our retina detector framework is Simple Linear Iterative Clustering (SLIC) [15], which was shown to be efficient not only in terms of computational time, but also in terms of region compactness and adherence. The algorithm is initialized by defining the number of superpixels to be generated. The value was set to 5000 which showed the best trade-off between computational efficiency and prediction accuracy.

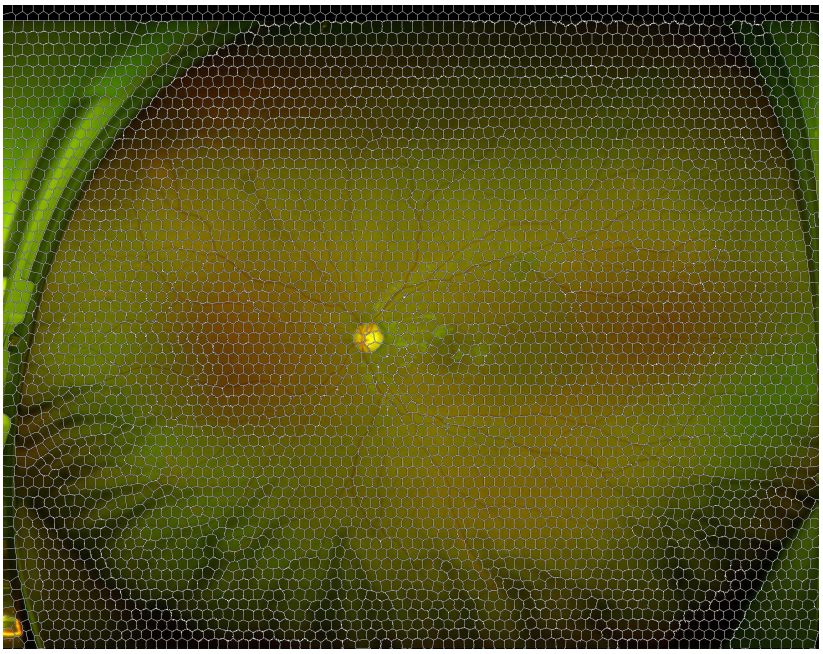

Figure 5.3: Retinal image divided into superpixels

5.2.5 Ground Truth Determination

Our proposed method for retinal area detection is based on training and testing the superpixel based features so as to distinguish between retinal area and the artefacts. For training purpose, we have the dataset of SLO images composed of 104 retinal scans. Some of the retinal scans have been obtained from diabetic retinopathy patients with having lesions on their retina. An example can be shown in Figure 5.4. The lesions can be shown as bright spots on retina. These lesions might be misguided as the part of artefacts during automatic retinal area detection due to their bright structure and appearance like actual artefacts in the SLO retinal scan. Therefore, the training set include the features calculated from superpixels obtained from retinal scans with and without lesions. As shown in Figure 5.4, the clinical annotation around the retinal area is taken into account to determine the class of superpixel as either retinal area or artefacts. The superpixels at the border of the retinal area annotation might contain pixels from both retinal area and the artefacts. In that case, the superpixel will be counted as part of retinal area or the artefacts if the majority of pixels in the superpixel belong to either class. In order to avoid large training set, we randomly selected 28 images for training and cross-validation and 76 images for the testing purpose.

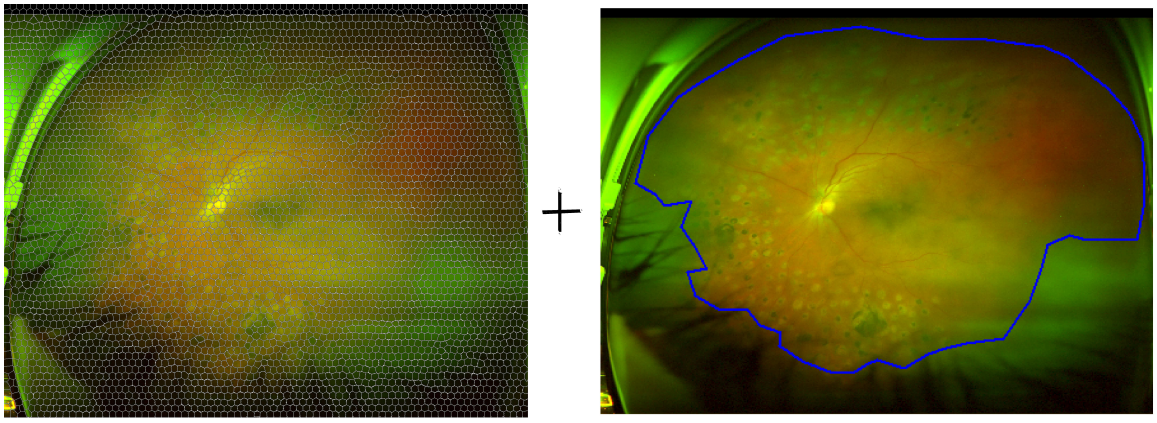

Figure 5.4: Determination of ground truth using superpixels and clinical annotations

5.2.6 Feature Extraction

After the generation of superpixels, the next step is to determine their features. We intend to differentiate between the retinal area and artefacts using textural and gradient based features. Textural and gradient based features are calculated from red and green channels on different Gaussian blurring scales; also known as smoothing scales [14]. In an SLO image, the blue channel is set to zero therefore no feature is calculated for the blue channel. The details of these features has been described in Section 4.4.1.

The image features are calculated for each superpixel of the images present in the training set and they form a matrix of the form as shown in Equation (5.3).

$$FM = \begin{bmatrix} A_R^{tex} & A_G^{tex} & A_R^{g} & A_G^{g} & A^{re} \\ \\ B_R^{tex} & B_G^{tex} & B_R^{g} & B_G^{g} & B^{re} \end{bmatrix} \tag{5.3}$$

where A and B represent class of true retinal area and class of artefacts respectively; superscripts tex, re, g represent textural features, regional features and gradient based features; and subscript R and G represent the red and green channel respectively. For determining features at different smoothing scales, both red and green channels of images are convolved with the Gaussian [14] at scales $\sigma = 1, 2, 4, 8, 16$. The textural features are calculated at the original scale as well as at five different smoothing scales so as to accommodate their image response in the training set after blurring. In this way the total number of columns (scalar values) in both channels of A^{tex} and B^{tex} will

be 114 making it 228 altogether. The gradient features has 6 columns in each scale making 30 columns for each channel of A^g and B^g so 60 columns in total for each superpixel. As far as regional features are concerned, except I_μ, they are independent of channel variation. Therefore, they are calculated only once for the superpixel so 7 columns for A^{re} and B^{re} (I_μ is calculated for both red and green channels). In this way, there are the total number of 295 features in FM calculated for each superpixel of the image present in the training set. Each column of the feature matrix calculated for the particular image is normalized using z-score normalization [40]. Z-score normalization returns the scores of the column with zero mean and unit variance. The normalized feature matrix can be represented as:

$$FM^{ZS} = \frac{FM - FM_\mu}{FM_\sigma} \tag{5.4}$$

where, FM_μ and FM_σ are the mean and standard deviation of FM across the examples.

5.2.7 Feature Selection

After the generation of feature matrix (FM^{ZS}), the next step is to select the features most relevant towards the classification. One advantage of feature selection procedure is increase in computational efficiency since we need to calculate only selected number of features. Another advantage of feature selection procedure is exclusion of the features which are inhibiting the classification power of the feature matrix.

For feature selection procedure, we have selected SFS approach for feature selection. The advantage of SFS procedure is that it can determine the features set which is most relevant towards the classification. This can be shown by comparison of its performance with other feature selection approaches as well as the feature set with having all features. The comparison of performance can be shown in Figure 5.5 in terms of classification power of different feature sets with the help of ROC curves. The ROC curves are generated using 5-fold cross validation on the training set. The ROC curves and AUC values reveal that if the features are selected using the SFS approach, they can have a classification power almost similar to the complete feature set while reducing the computational time.

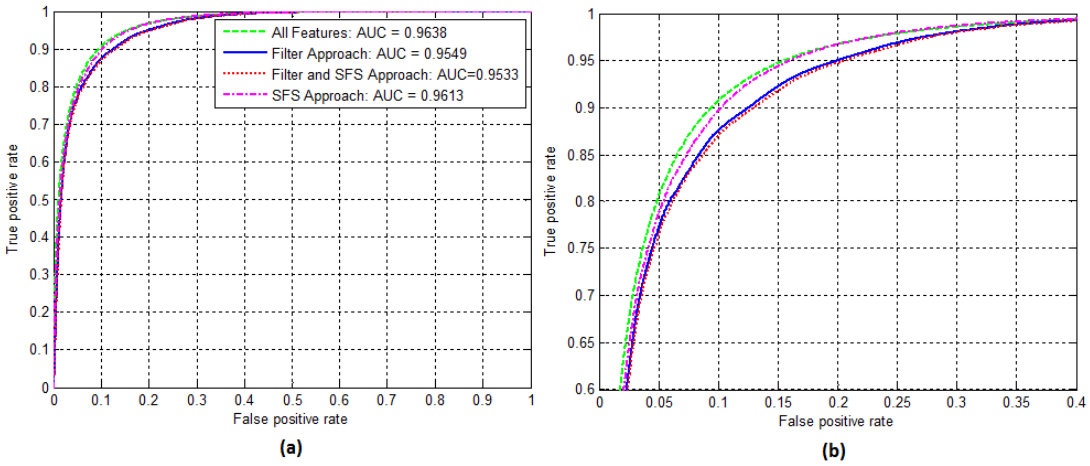

Figure 5.5: (a) Receiver Operating Characteristics on the test sets (b) magnified version of (a)

The individual and collective performance of the features selected in the feature sets from the above mentioned approaches are shown in Figure. 5.6. The x-axis of each plot has been shown in Table 5.1. As an example, the variables for 'Feature Index' (x-axis for Figure. 5.6(a) and (b)) has been shown in the respective column of Table 5.1 in order. The explanation of each variable can be found in Section 4.4.1. As an example, in $\mu_{sumR}(16)$, μ_{sum} is the 'Sum average' taken from the Textural features of Table 4.4. R subscript denotes the red channel whereas 16 represents the value of Gaussian scale. Similarly, $\mathcal{N}_{yyR}(2)$ is the red channel convolved with second order gradient in y-axis with gaussian scale 2 (Section 4.4.1 and Table 4.5).

According to Figure 5.6, the results show that the SFS approach performed better compared to other two approaches despite the fact that the feature set also consists of those features which ranked low in independent evaluation criterion. We selected 10 features out of 295 features since there was little improvement or no in AUC beyond it. The SFS is computationally intensive as it requires 5 minutes / feature on filtered feature set and 30 minutes/feature on complete feature set. Nevertheless, SFS is once in a lifetime process and the calculation time for calculating 10 features is 25 seconds per image whereas calculating the complete feature set can take around 10 minutes per image with comparable performance to the SFS feature set as shown in Figure 5.5. The Table 5.2 represents the percentage of different types of features selected in each feature set. The table shows clear dominance of textural features compared to gradient features and regional features.

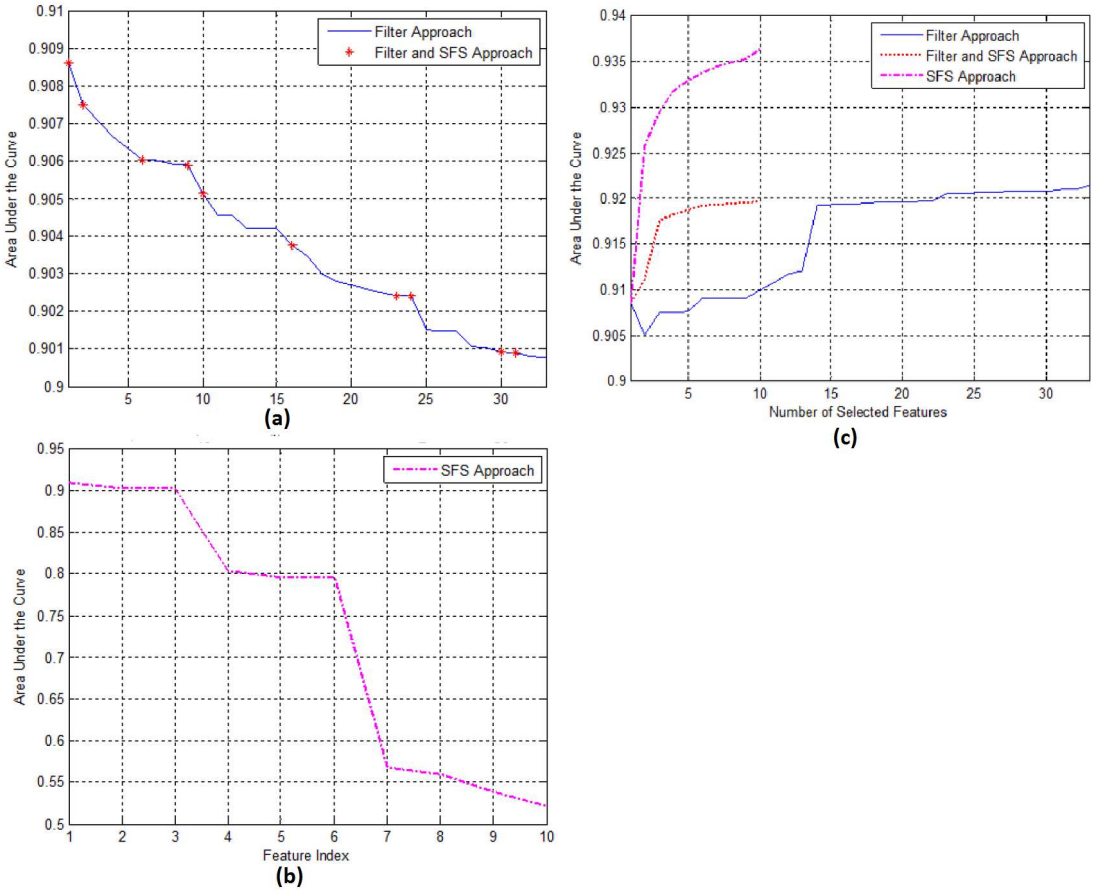

Figure 5.6: (a),(b) Plot of independent evaluation criterion. The axis of 'Feature Index' in Figure. 5.6 (a) and (b) is ordered according to descending independent evaluation criterion. The features represented by 'Feature Index' and 'Number of Selected Features' are shown in Table 5.1. The features are ranked in descending order of independent evaluation criterion value. (a) shows Red dots for 'Filter and SFS approach' represent the 10 features selected by applying SFS on 'Filter approach' set. By applying the SFS on complete feature set, 10 out of 295 features have been selected as shown in (b) 'SFS approach'. (c) shows plot of increasing classification power (AUC) value by selecting the features one by one in different feature set. The axis of 'Number of Selected Features' in Figure. 5.6 (c) represents the order with which the features are selected using the SFS approach.

Table 5.1: Feature sets obtained usung different feature selection approaches. 'Feature Index' represents the order of highest independent evaluation criterion measure. 'Number of Selected Features' represent the sequence of feature selection in the feature set. R and G subscripts represent Red and Green channel respectively. The detail of feature symbols can be found in Section 4.4.1

Feature Selection Method	Feature Symbols
Filter Approach (Feature Index and Number of Selected Features)	$\mu_{sumR}(16)$, $\sigma_{sumR}(16)$, $\mu_{sumR}(8)$, $\mathcal{N}_R(16)$, $\mu_{sumR}(4)$, $\sigma_{sumR}(8)$, $\mu_{sumR}(2)$, $\mu_{sumR}(1)$, μ_{sumR}, $\sigma_{sumR}(4)$, $\sigma_{sumR}(2)$, $\mathcal{N}_R(8)$, $\sigma_{sumR}(1)$, $acorr_R(16)$, $\sigma_{sosR}(16)$, σ_{sumR}, $\mathcal{N}_R(4)$, $\mathcal{N}_R(2)$, $\mathcal{N}_R(1)$, $\mathcal{N}_{yyR}(1)$, $I_{\mu R}$, $\mathcal{N}_{xxR}(1)$, $acorr_R(8)$, $\sigma_{sosR}(8)$, $acorr_R(4)$, $\sigma_{sosR}(4)$, $\mathcal{N}_{yyR}(2)$, $acorr_R(2)$, $\sigma_{sosR}(2)$, $acorr_R(1)$, $\sigma_{sosR}(1)$, $acorr_R$, σ_{sosR}
Filter and SFS Approach (Feature Index)	$\mu_{sumR}(16)$, $\sigma_{sumR}(16)$, $\sigma_{sumR}(8)$, μ_{sumR}, $\sigma_{sumR}(4)$, σ_{sumR}, $acorr_R(8)$, $\sigma_{sosR}(8)$, $acorr_R(1)$, $\sigma_{sosR}(1)$
Filter and SFS Approach (Number of Selected Features)	$\mu_{sumR}(16)$, $\sigma_{sosR}(1)$, $\sigma_{sumR}(8)$, $\sigma_{sosR}(8)$, $\sigma_{sumR}(16)$, μ_{sumR}, σ_{sumR}, $acorr_R(8)$, $acorr_R(1)$, $\sigma_{sumR}(4)$
SFS Approach (Feature Index)	$\mu_{sumR}(16)$, $acorr_R(8)$, $\sigma_{sosR}(8)$, σ_{sumG}, $acorr_G$, σ_{sosG}, $H_G(8)$, $\mathcal{N}_{yR}(16)$, $H_G(1)$, $H_{diffG}(1)$
SFS Approach (Number of Selected Features)	$\mu_{sumR}(16)$, σ_{sosG}, $H_G(8)$, $\mathcal{N}_{yR}(16)$, $\sigma_{sosR}(8)$, $H_{diffG}(1)$, $acorr_G$, $acorr_R(8)$, σ_{sumG}, $H_G(1)$

Table 5.2: Percentage of different types of features across different feature set

Feature Set	Textural Features	Gradient Features	Regional Features
SFS approach	90%	10%	0%
Filter approach	72.73%	24.24%	3.03%
Filter and SFS approach	100%	0%	0%

5.2.8 Classifier Construction

The classifier is constructed in order to determine the different classes in a test image. In our case, it is a two class problem: true retinal area and artefacts. We have applied Artificial Neural Networks (ANN). The ANN is the classification algorithm that is inspired by human and animal brain. It is composed of many interconnected units called artificial neurons. ANN takes training samples as input and determines the model that best fits to the training samples using non-linear regression. Consider the Figure 5.7 which shows three basic blocks of ANN i.e. input, hidden layer (used for recoding or providing representation for input) and output layer. More than one hidden layer can be used but in our case, there is only one hidden layer with 10 neurons. The output of each layer is in the form of matrix of floating values which can be obtained by sigmoid function as:

$$h_W(x) = \frac{1}{1 + \exp(-W^T x + b)} \tag{5.5}$$

where b is the bias value and W are the weights of input x. These weights can be determined by *backpropagation algorithm* which tends to minimize mean square error value between desired output and actual output as:

$$err = \frac{1}{2}(t - y)^2 \tag{5.6}$$

where t and y represent the target output and actual output of the output layer. The minimization of Equation (5.6) can be represented as:

$$\frac{\partial err}{\partial W_i} = (y - t)y(1 - y)x_i \tag{5.7}$$

Since it is an iterative process therefore weights are updated by *delta rule* as

$$\Delta w_i = \alpha(t - y)x_i \tag{5.8}$$

α represents the step size. The weights were updated until 1000 iterations.

After the construction of our classifier, we have compared its performance against different classifiers in terms of accuracy and computational time. The classifiers have been applied across different feature sets which are obtained by using different feature selection procedures as mentioned in Section 4.4.2. The classifiers we have selected for

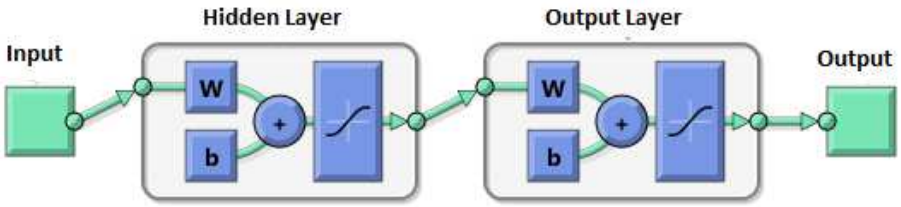

Figure 5.7: Artificial Neural Networks Diagram

comparing the performance of our classifier are Support Vector Machines (SVM) and k Nearest Neighbours (kNN) [40].

The idea behind kNN method is to find out samples whose feature are similar to the classes to be detected. The function, which we are following in order to determine the similarity of the features with true retinal area is 'Euclidean Distance'. SVM finds a separating hyperplane with the maximal margin in higher dimensional space. In our comparison study, we are using non-linear SVM with Radial Based Function (RBF) kernel with default parameter of $(number\ of\ features)^{-1} = 0.1$ [61].

5.2.9 Experimental Evaluation

In order to determine degree of overlap between the retinal areas obtained from clinical annotation and automatic segmentation results, we have used Dice Coefficient. Let RA_1 and AR_1 represent samples (e.g. Superpixels or pixels) from the retinal area and the artefact area obtained from the framework respectively and RA_2 and AR_2 be these samples from the benchmark. The class of superpixels in the benchmark is decided based on majority of pixels in the superpixel belonging to particular class. Also, $|RA_1| + |AR_1| = |RA_2| + |AR_2| = N_{sample}$ i.e. total number of samples (superpixels or pixels) in an image. If we calculate Dice Coefficient for the image, Equation (4.7) can be deduced as:

$$D_I = \frac{(|RA_1 \cap RA_2| + |AR_1 \cap AR_2|)}{N_{sample}} \tag{5.9}$$

The Dice Coefficient for the retinal area D_R is given as:

$$D_R = \frac{2|RA_1 \cap RA_2|}{|RA_1| + |RA_2|} \tag{5.10}$$

The results of retinal area detection are shown in Table 5.3. The table shows significant performance of retinal area detection with accuracy of 92%. Some good examples

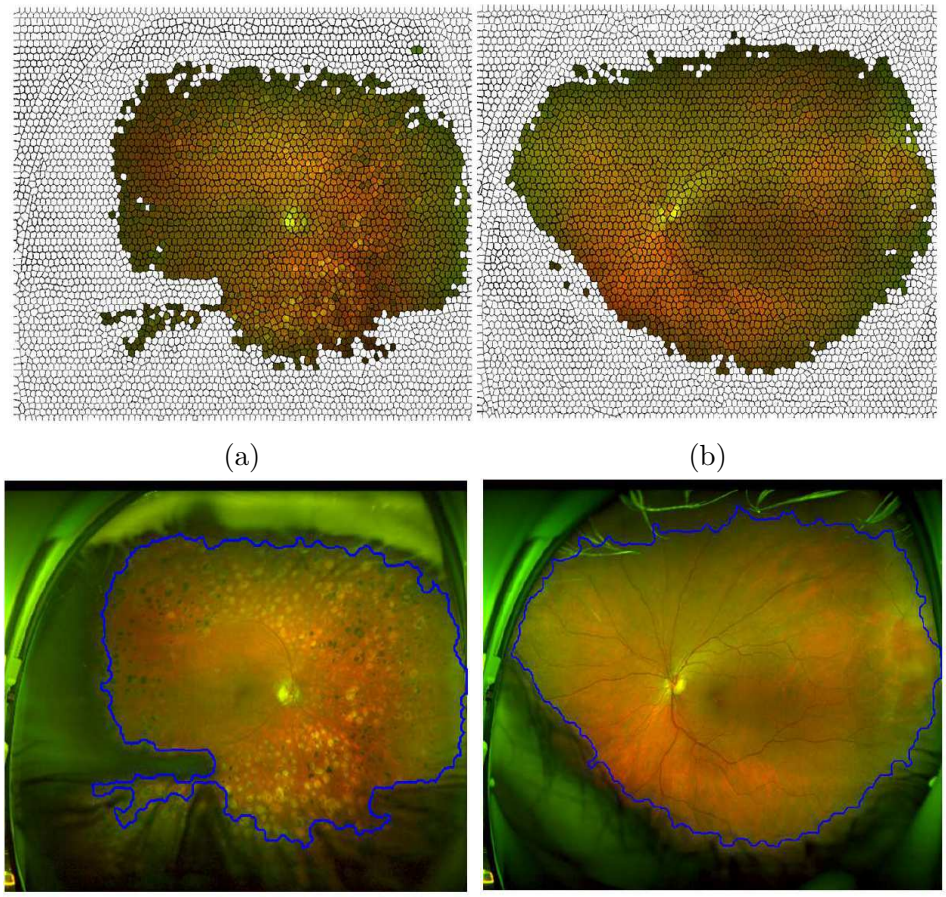

(a) (b)

(c) (d)

Figure 5.8: Superpixel classification result of two examples of the SLO images. Columns represent different examples of retinal images. Left column are retinal scans with lesions whereas right column is the retinal scan from healthy subject. Figures (a) to (b) represent superpixel classification results and Figures (c) to (d) represent the final output

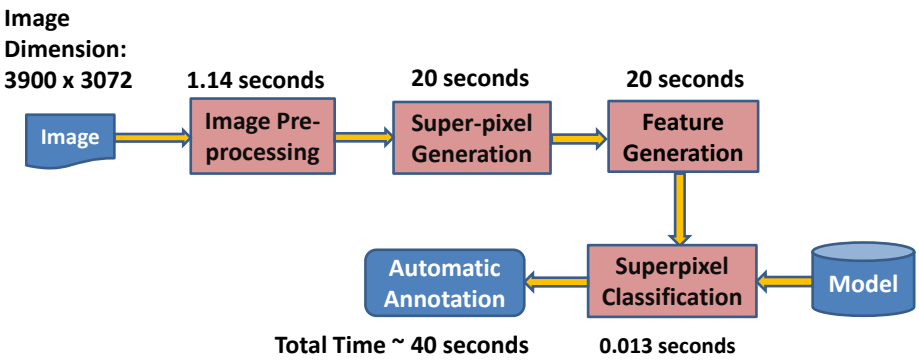

Figure 5.9: Block diagram of deployment stage of retinal area detector alongwith execution time of each block

of retinal area detection has been shown in Figure 5.8. The Figure 5.8(a) and (c) show the examples of superpixel classification and retinal area detection on the retinal scan with disease lesions whereas the same for healthy retinal scan has been shown in Figure 5.8(b) and (d). The retinal area detection accuracy on these examples of diseased and healthy retinal scans is 90% and 95% respectively. The accuracy is quite high in most of the images in the testing set however, there are some false positives in case of retinal scan with higher visibility of eyelids which should be classified as part of artefacts. An example has been shown in Figure 5.10. The example shows that a portion of eyelid has been misclassified as part of retinal area. In this case the retinal area detection accuracy is 85%.

Table 5.3 compares the performance of ANN with other classifiers. As far as classification accuracy is concerned there is little difference among the outputs of different classifiers. The advantage of using ANN is its high computational efficiency in terms of classification testing time. Compared to SVM, ANN has the advantage of reduced processing time while processing a batch of images. Although the training time of ANN is longer compared to its other two counterparts, the training stage is once in a lifetime process and once the model is deployed, it can process any image. Figure. 5.9 represents the total time taken by an image to be processed for automatic annotations.

Table 5.3: Comparison of framework output performance using different classifiers. The performance is compared with respect to computational time taken during training and testing and average accuracy. The training time is calculated for 28 images. Testing time shows the average time taken by the framework

			Superpixel Samples		Pixel Samples	
Classifier	Training Time	Testing Time	D_I	D_R	D_I	D_R
ANN	30 minutes	0.013 seconds	90.48%	90.28%	91.93%	91.87%
SVM	12.5 minutes	8.5 seconds	90.93%	90.89%	92.00%	91.94%
kNN	1.45 seconds	2.05 seconds	90.34%	90.17%	91.43%	91.31%

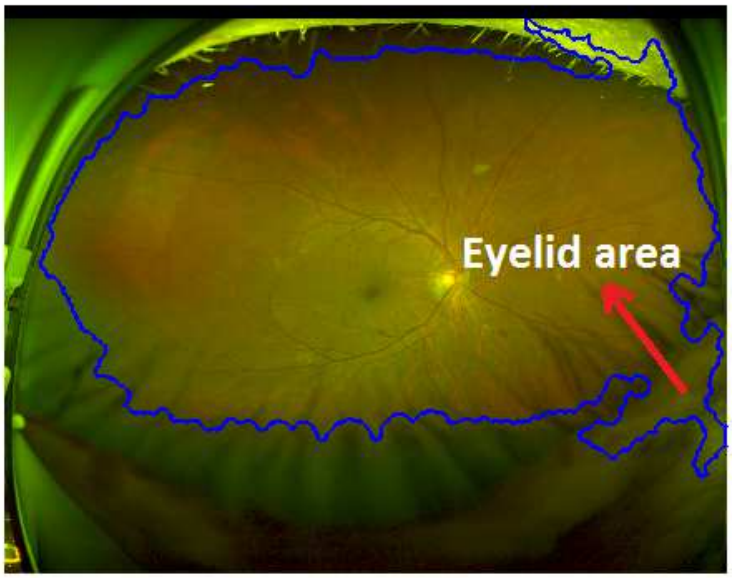

Figure 5.10: An example of retinal area detection with higher visibility of eyelids

5.3 The ONH Localization

After determination of retinal area, the next step is to localize the ONH. The purpose of localizing the ONH is to determine glaucoma related features which require segmentation of the ONH related structures. The literature survey suggests several methods which have been divided into three different categories (Section 3.2.1). Out of these categories, the category which regards the ONH center as convergence point of vasculature segmentation has been the most successful. These methods usually not misguided by the bright spots on retina which are not part of the ONH. However, the accuracy of these methods depend on vasculature enhancement in the ONH area. Among different methods under this category, our method is inspired with the method of horizontal and vertical edge mapping [88] due to its speed and robustness. We have determined weighted feature maps for the ONH localization which enhance the ONH region for better accuracy and robustness. The details are discussed as follows:

5.3.1 Weighted Feature maps based ONH Localization Method

In this method, two feature maps are calculated. Their equations are given as follows:

$$F_1 = (|I_x| - |I_y|)./Y \tag{5.11}$$

$$F_2 = (|I_x| + |I_y|). * Y \tag{5.12}$$

where I_x and I_y are gradients with respect to x and y direction respectively. Y is the intensity map and $.*$ and $./$ are pixelwise multiplication and division respectively. The purpose of F_1 is to enhance the vasculature. Since the vasculature converges at the ONH, therefore we will determine the point along horizontal axis with maximum vasculature density i.e. the ONH. The red slider shown in Figure 5.11a slides along the horizontal direction. The width of the slider is equal to the maximum width of the retinal blood vessel. The slider profile at the particular point is the sum of all the pixels from the feature map (F_1) within the slider region. Since the vasculature region has the maximum density at the ONH area, therefore the sum would be maximum compared to other points in the horizontal direction and slider will stop at that point. On the other hand, the square slider slides on F_2 (Figure 5.11b) in the vertical direction where the rectangular slider in F_1 has stopped. F_2 map enhances the ONH region, therefore the square slider will stop at the center of the ONH. The width of the square slider is equal to the square area in which the ONH can be contained.

The ONH localization using Equation (5.11) and (5.12) has worked in most of the images in our datasets but it has been misguided sometimes if there are lesions on the retina which can be mistreated as part of vasculature or if ONH area is blurred. In order to increase the robustness of the algorithm, we have determined *Weight maps* of both feature maps and then performed pixelwise multiplication between feature maps and the respective weight maps. In the coloured retinal scan, the green channel has prominent ONH region compared to red or blue channel. Therefore, for determining weight maps, the green channel of the image is passed through Fast Radial Symmetry Transform (FRS) [144] and Matched Filtering [30]. FRS transform obtains the positively affected pixels and negatively pixels along the gradient directions in a predefined radius. It enhances ONH due to its brightness and strong edges and diminishes the reflections with weak edges. The matched filter involves convolution of green channel with Gaussian kernel in 12 directions from 0°to 360°and the maximum response from each filter is taken into consideration. It is one of the oldest technique to segment out

retinal vasculature structure. Although its not completely accurate, it enhances the vasculature structure of the retina.

Each of the FRS transformed map and matched filter map is normalized between 0 and 1 and then pixelwise multiplied to F_2 and F_1 respectively. In this way, the vasculature structure and ONH area are enhanced more than other retinal areas. We now have equations as:

$$F_1 = (|I_x| - |I_y|)./Y. * MF(I) \tag{5.13}$$

$$F_2 = (|I_x| + |I_y|). * Y. * frs(I, rad) \tag{5.14}$$

where frs and MF are weight maps obtained from Fast Radial Symmetry Transform and Matched Filtering respectively. The frs is initialized with the rad equal to radius of the optic disc. The feature maps from one image has been shown as an example in Figure 5.11. The location result in fundus image as well as the SLO image has been shown in Figures 5.12 and 5.13.

5.3.2 Ground Truth

In order to determine the localization accuracy of the ONH, we have the datasets of fundus images and the SLO images.

Fundus Images: The fundus image dataset has been obtained from Drishti-GS [115]. There are 50 images in the training set. Each image in the training set has been annotated with the centre of the ONH along with the ONH (optic disc) boundary annotation. The ONH boundary annotation is used to calculate the minimum distance of the ONH boundary from the centre.

SLO Images: There are 102 SLO images in the dataset. Each dataset has been annotated around the ONH (optic disc). The centre of the ONH is calculated by determining the centroid of the annotations of the ONH boundary. The minimum distance of the ONH boundary from the centre has also been calculated.

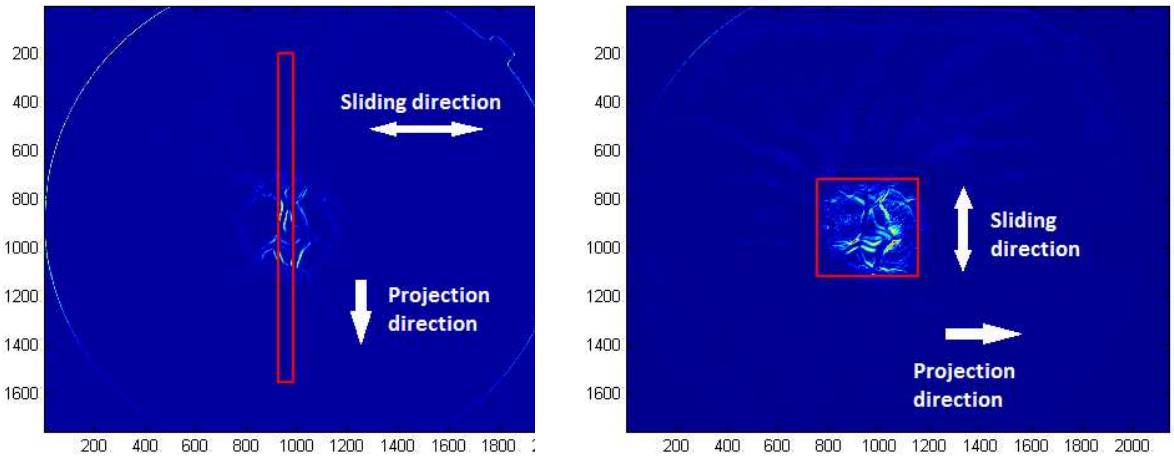

(a) Feature map 1(F_1) (b) Feature map 2(F_2)

Figure 5.11: Examples of both feature maps with respective sliders. The feature maps have been enhanced by pixelwise multiplication with matched filter map and FRS transform map.

5.3.3 Experimental Evaluation

The ONH centre is considered automatically localized if the distance between manually annotated ONH centre and automatically localized ONH have the distance less than 50% of the minimum distance between the ONH centre and the ONH boundary. The approach of accuracy measurement has been followed by most of the ONH localization methods [88], [45]. The results with average accuracy and execution time are shown in Table 5.6. The ONH localization method achieved the 100% accuracy on the Drishti-GS images. However, the method is failed on two SLO images as the vasculature area is not enhanced due to high atrophy area around the ONH. As far as total execution time is concerned, most of the total execution time is of frs which is 8 seconds for the Drishti-GS dataset and 12 seconds for the Optomaps. The frs execution time depends on the image resolution as well as radius of the ONH.

Table 5.4: Accuracy and execution time of ONH localization in different datasets

Image Dataset	Accuracy	Execution Time	Image Resolution
Drishti-GS	100%	10 seconds	2896 x 1944
Optomaps	98%	15 seconds	3900 x 3072

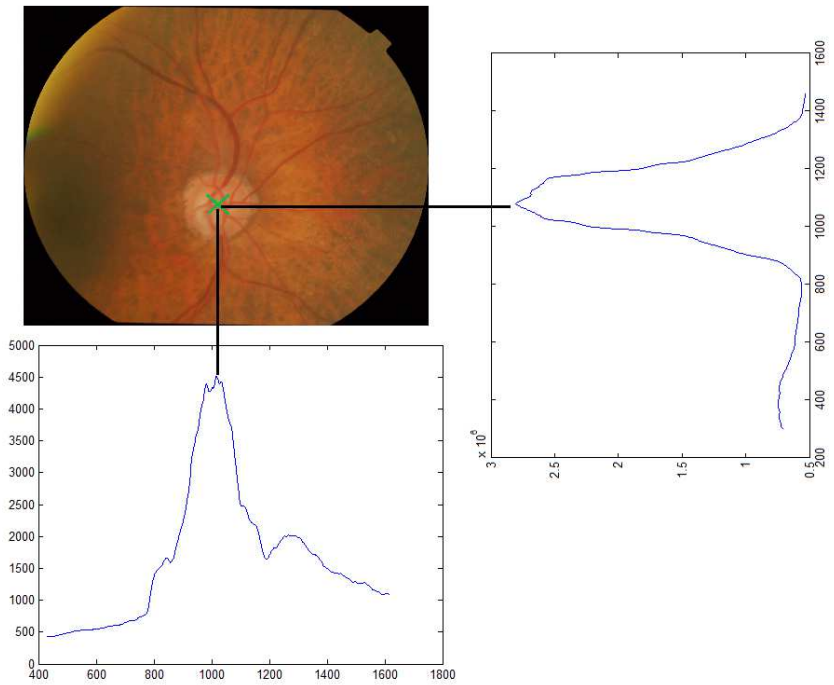

Figure 5.12: Fundus image ONH localization example with slider profile

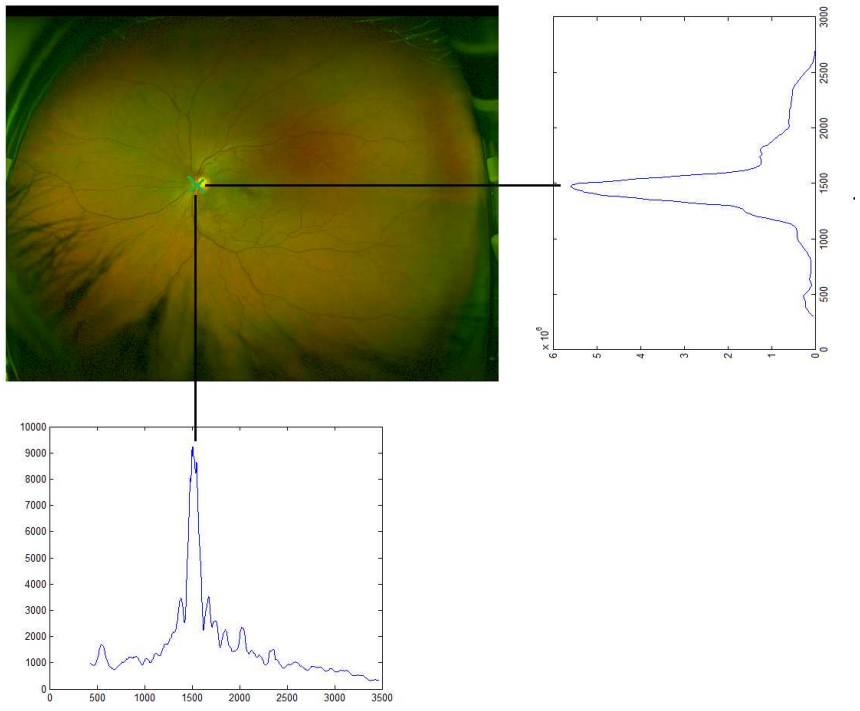

Figure 5.13: SLO image ONH localization example with slider profile

5.4 Vasculature Segmentation

After localizing the ONH, the next step is to segment out vasculature structure. As discussed earlier, there are two main reasons for segmenting out vasculature structure in our project.

1. The vasculature structure occludes the ONH area. Therefore we need to segment and remove it for accurate segmentation of the optic disc and the optic cup.

2. The vasculature shift in the ONH area is in itself indication towards glaucoma [65].

There are several methods reported for retinal blood vessel segmentation [30,47,87]. Most of these methods have been applied on complete retinal area; most of them misidentified ONH boundary as part of the vasculature structure. Also in case of glaucoma images, PPA was also misidentified as the part of vasculature area.

5.4.1 Ground Truth

Our proposed vasculature segmentation method has been applied on the ONH cropped image. The ONH cropped image has been obtained after the ONH localization and cropping the ONH area. The training has been performed between non-vasculature area and vasculature area in the ONH cropped image. The method has been applied on both fundus and the SLO images.

Fundus Images: The fundus images annotated with vasculature area have been taken from the dataset of Pattern Recognition Lab, Erlangen (PRLE) as the glaucoma datasets for fundus images (Drishti-GS and RIM-ONE) have not been annotated with vasculature area. The PRLE dataset has 30 images with each image has the resolution of 3504 x 2336 pixels however, after the ONH cropping, the resolution is 300 x 300 pixels.

SLO Images: We have 51 images annotated with vasculature area. Each image has the resolution of 3900 x 3072 pixels however, it becomes 341 x 341 after ONH localization and cropping the ONH area.

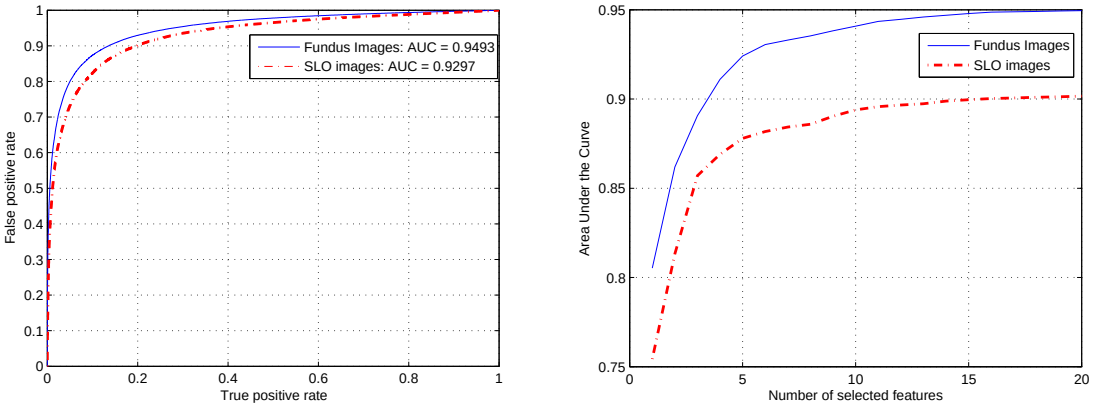

(a) (b)

Figure 5.14: Results of feature selection procedure with (a) Area Under the Curve of Fundus Images and the SLO images and (b) SFS feature selection procedure. The x-axis symbols are shown in Table 5.5

5.4.2 Feature Generation and Selection

We perform pixelwise classification between vasculature structure and non-vasculature area. The reason for not using superpixel in this case is that misclassification of a superpixel which is a group of pixels can be more expensive for accuracy as compared to a misclassified pixel. The pixel wise training may account for high computational time in training and testing stages. Therefore, we have randomly selected 1000 pixels from each of vasculature area and non-vasculature area in order to avoid large training sets which might be computationally inefficient for training. The vasculature structure is more prominent in the green channel, therefore the gradient, Gabor and biologically inspired features are calculated using the green channel. The textural features would be computationally inefficient for pixelwise calculation especially in testing stage so they were not included in the feature set. The final feature matrix is shown as follows:

$$FM = \begin{bmatrix} A_G^g & A_G^{gab} & A_G^{bio} \\ \\ B_G^g & B_G^{gab} & B_G^{bio} \end{bmatrix} \tag{5.15}$$

where A and B represent classes of vasculature area and non-vasculature area, superscripts g, gab, bio represent gradient based, Gabor and biologically inspired features respectively and G represents the green channel. For gradient based features, we have used scales $\sigma = \sqrt{2}, 2, 2\sqrt{2}, 4$. The Gaussian features have 6 columns in each scale making 24 columns. Also, the maximum responses across the scales of each feature

shown in Table 4.5 are also calculated. In short, the total gradient based features were 43. In addition, 18 biologically inspired and 32 Gabor features at different directions and frequencies are selected. In this way, there are the total number of 93 features in the feature matrix for each pixel of the image present in the training set. Each column of the feature matrix calculated for the particular image is z-score normalized.

The results of feature selection procedure using the SFS approach are shown in Figure 5.14b. Like in case of retinal area detection, the SFS continued selecting the features till the instant when there is little or no improvement. For both fundus images and the SLO images, 20 features have been selected. The 'Selected Feature Set ' is shown in Table 5.5. The AUC has been calculated using 5-fold cross validation in the training set and is shown in Figure 5.14a.

Table 5.5: Feature sets obtained using SFS approach for vasculature segmentation. The detail of feature symbols can be found in Section 4.4.1

Datasets	Feature Symbols
Fundus Images	$\mathcal{N}_{xxG}(4)$,$BY(2,5)$,$\bigtriangledown I_G$,$\mathcal{N}_{yyG}(4)$, $ML(4)$,$BY(4,8)$,$ML(2\sqrt{2})$, ν_0, $\mathcal{N}_{yG}(\sqrt{2})$, $Gb(x,y,0°,2,\frac{1}{3},\frac{\sqrt{2}}{3})$, $ML(2)$,$Gb(x,y,0°,2,\frac{1}{4},\frac{\sqrt{2}}{4})$, $\mathcal{N}_{xG}(\sqrt{2})$,ρ, $I(4,8)$, R_B, $Gb(x,y,90°,2,\frac{1}{3},\frac{\sqrt{2}}{3})$, $Gb(x,y,90°,2,\frac{1}{10},\frac{\sqrt{2}}{10})$, $\mathcal{N}_{yyG}(2\sqrt{2})$, $\mathcal{N}_{yyG}(\sqrt{2})$
SLO Images	$BY(2,5)$, ρ, $\bigtriangledown I_G$, R_B, $N_{\gamma-norm}(L)$, $A_{\gamma-norm}(L)$, $\mathcal{N}_{yyG}(\sqrt{4})$, $ML(2\sqrt{2})$, $\mathcal{N}_{xxG}(2\sqrt{2})$, $\mathcal{N}_{yyG}(2\sqrt{2})$, $\mathcal{N}_{xxG}(2)$, $\mathcal{N}_{xxG}(4)$, $Gb(x,y,90°,2,\frac{1}{3},\frac{\sqrt{2}}{3})$, ν_0, $\mathcal{N}_{xG}(\sqrt{2})$, $Gb(x,y,90°,2,\frac{1}{10},\frac{\sqrt{2}}{10})$, $I(4,8)$, $I(4,7)$, $\mathcal{N}_{yG}(\sqrt{2})$, $\mathcal{N}_{xxG}(\sqrt{2})$

5.4.3 Experimental Evaluation

For classification between vasculature area and non-vasculature area in the ONH cropped image, we have used backpropagation ANN with single layer. We have allocated 20 neurons in the hidden layer although good results can be achieved from 10 neurons till 30. The ANN has been trained and validated using 5-fold cross validation.

From the output of the ANN, we can obtain neural weights which determines the membership value for the particular class. It is quite tricky to classify between the vasculature structure and the non vasculature area near optic disc. The non-vasculature area contains pixels from optic disc rim, optic cup, PPA (if present) and retinal area. Therefore, we segmented out only those pixels which has neural weights greater than 0.98. Some of the classification results are shown in Figure 5.15. The segmentation accuracy has been evaluated against the ground truth (Section 5.4.1)

using dice coefficient as:

$$D_{vas} = \frac{2(|vas_1 \cap vas_2|)}{|vas_1| + vas_2|} \tag{5.16}$$

where vas_1 and vas_2 are vasculature area obtained from the benchmark and automatic segmentations respectively. The vasculature segmentation accuracy, AUC values and execution time are shown in Table 5.6. For testing purpose, the ONH area has been cropped from PRLE and Optomaps after ONH localization. These results have been calculated for PRLE and SLO images.

Table 5.6: Accuracy and execution time of vasculature segmentation in different datasets.

Image Dataset	Segmentation Accuracy	AUC	Execution Time
PRLE	90.77%	0.9493	10 seconds
SLO images	90.21%	0.9297	10 seconds

The results although accuracy greater than 90%, our main task of determining ONH cropped image vasculature classifier is to avoid edges of the optic disc and PPA while segmenting vasculature area. Therefore, we have tested our classifier on RIM-ONE dataset [49] (Section 4.2). The vasculature segmentation classifier for SLO images has been tested on ONH cropped SLO images. Figure 5.15 shows examples of segmentation output of the vasculature classifier on both fundus (Figure 5.15(b),(d)) and SLO images (Figure 5.15(f)). The fundus images have been taken from RIM-ONE dataset. All these examples show the vasculature segmentation result while avoiding optic disc boundary to be the part of vasculature area. Figure 5.15(b) shows the vasculature segmentation results on the image with PPA in Figure 5.15(a). This example shows that our vasculature classifier is not over-segmenting the PPA to be the part of vasculature area. We can also deduce from visual examples of vasculature segmentation on RIM-ONE that classifier designed on PRLE images is able to segment out vasculature area in RIM-ONE. Since we don't have vasculature annotations on RIM-ONE, therefore we have not performed quantitative analysis of vasculature segmentation accuracy on RIM-ONE. Like RIM-ONE, the classifier can also segment out vasculature area in Drishti-GS dataset. The total execution time depends on the size of the ONH cropped image.

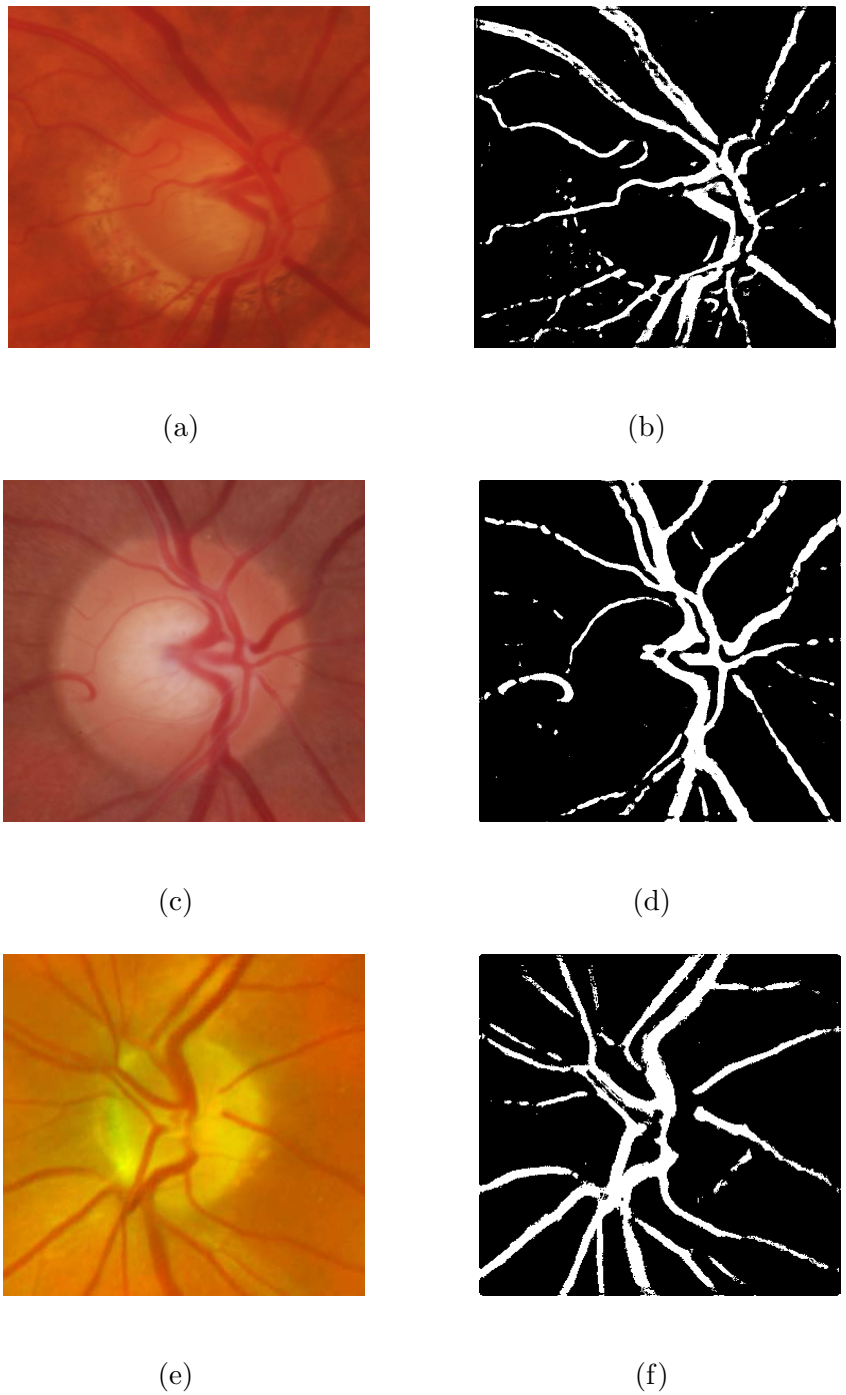

(a) (b)

(c) (d)

(e) (f)

Figure 5.15: Examples of segmentation results on fundus images and the SLO images. (a) glaucoma fundus image from RIMONE with PPA around it, (b) segmented output of (a), (c) normal fundus image from RIMONE, (d) segmented output of (c), (e) the SLO image and (f) segmented output of (e)

5.5 Conclusion

In this chapter, we discussed about pre-processing steps need to extract the ONH area. The pre-processing steps include retinal area detection, ONH localization and vasculature segmentation. Distinguishing true retinal area from artefacts in SLO images is a challenging task, which is also the first important step towards computer-aided disease diagnosis. In this work, we have proposed a novel framework for automatic detection of true retinal area in SLO images. We have used superpixels to represent different irregular regions in a compact way and reduce the computing cost. Feature selection enables the most significant features to be selected and thus reduces computing cost too. A classifier has been built based on selected features to extract out the retina area. It has been compared with other two classifiers and was compatible while saving the computational time. The experimental evaluation result shows that our proposed framework can achieve an accuracy of 92% in segmentation of the true retinal area from an SLO image. The automatic retinal area detection in SLO images can serve as a first step in automatic analysis of retinal diseases in SLO images while avoiding bright artefacts to be the part of retinal area. This can be crucial in automatic analysis of retinal diseases with lesions. However, the segmentation accuracy should be above 90% in order to include important regions of the retina i.e. the ONH, disease lesions etc. In case of glaucoma, the ONH localization algorithm is able to perform more accurately after true retinal area detection.

Apart from retinal area detection, we have proposed weighted feature map based ONH localization method so as to improve the ONH localization accuracy and robustness. The average ONH localization accuracy on fundus images and SLO images is 100% and 98% respectively. The vasculature segmentation is a key step to determine the vasculature shift which is one of the geometrical indication associated with glaucoma. We proposed the classification model for segmenting out vasculature area from the ONH image. The average segmentation accuracy achieved on fundus images and SLO images is 90.77% and 90.21%. The following chapters are based on detailed analysis of ONH area and segmentation of its different regions so as to determine structural and geometrical changes associated with glaucoma

Chapter 6

Optic Disc Segmentation

6.1 Introduction

This chapter is concerned with automatic segmentation of the optic disc boundary. The optic disc boundary can be segmented out if the optic disc centre is accurately localized since it is used for initialization of the model representing the optic disc boundary. The segmentation of optic disc is essential for determining glaucoma related features such as the CDR, neuroretinal rim loss etc. Their automatic determination is not a trivial task since it involves accurate segmentations of optic disc and optic cup. There are several methods with respect to optic disc segmentation which have been discussed in Chapter 2. We have divided those methods into three different categories i.e. non-model based approaches, boundary approximation modeling, statistical shape modeling and freeform modeling approaches. Non-model based approaches are based on morphological operation which are highly dependent on grayscale values. Boundary approximation modeling are the approximate representation of optic disc in terms of elliptical or circular area. For accurate representation of optic disc boundary, the statistical shape modeling or freeform modeling could have been the better choice. However, there were certain issues in the previous methods. Firstly, most of the previous optic disc extraction methods have been applied on red channel. There can be certain channels which can have higher classification power to distinguish between inside and outside of the optic disc. These channels can be determined by feature generation methods discussed in Section 4.4.1. We can call these channels as *feature*

maps. Secondly, the statistical shape analysis methods were often misguided by vasculature occlusion [56]. Also, statistical shape modeling has always as issue in order to find optic disc edge. Thirdly, in case of glaucoma, both statistical and freeform modeling approaches were misguided by the PPA.

In order to address these issues, we propose two models i.e. *Point Edge Model* (PEM) and *Region Classification Model*. The RCM determines the optic disc region using the set of feature maps suitable for region classification. On the other hand, the PEM updates the contour obtained from RCM according to the force field equation of the feature maps with the highest gradient around the optic disc boundary. The main purpose of PEM is to update the contour according to true edge of the optic disc. We call the hybridization of these two models as *Point Edge and Region Classification Model*.

6.2 Ground Truth

The training and evaluation of the proposed models has been carried out in two types of datasets i.e. the SLO images and fundus images. As discussed earlier, the feature sets obtained for both types of datasets are different. The ground truth protocols for both datasets have been explained as follows:

SLO Images: There are 102 SLO images out of which 51 images have been obtained from healthy subjects whereas 51 images have been obtained from glaucomatous suspected subjects. Each image has been ONH cropped with resolution of 341 x 341 after ONH cropping. Each image has been annotated around optic disc by one expert.

Fundus Images: In fundus dataset, we have 50 images from Drishti-GS dataset and 158 images from RIM-ONE. The Drishti-GS images have been ONH cropped with resolution of 701 x 701 after ONH cropping. However, there is no disease annotation in Drishti-GS dataset. Each image has been annotated around optic disc by four experts. As far as RIM-ONE is concerned, it is composed of ONH cropped images. RIM-ONE is composed of 118 healthy and 40 glaucomatous images with resolution varying from 300 to 900. Each image has been annotated around optic disc by five experts. For constructing training and validation set, we have randomly picked 40 images from Drishti, 40 healthy from RIM-ONE and 40 glaucomatous images from RIM-ONE; making 120

altogether. The rest of the images have been used for testing the model.

6.3 Point Edge and Region Classification Model

The *Point Edge and Region Classification Model* (PERCM) for optic disc segmentation is based on region search as well as edge search. Therefore, we have trained two types of models. One model will search the optic disc region using the region classification model which we name as *Region Classification Model* (RCM). Other model will update the shape model using edge force. We name this model *Point Edge Model* (PEM). The block diagram of the PERCM is shown in Figure 6.1. We will discuss the following relevant components in detail:

1. Generation and selection of feature maps
2. Region Classification Modeling (RCM)
3. Point Edge Modeling (PEM)
4. The PERCM algorithm

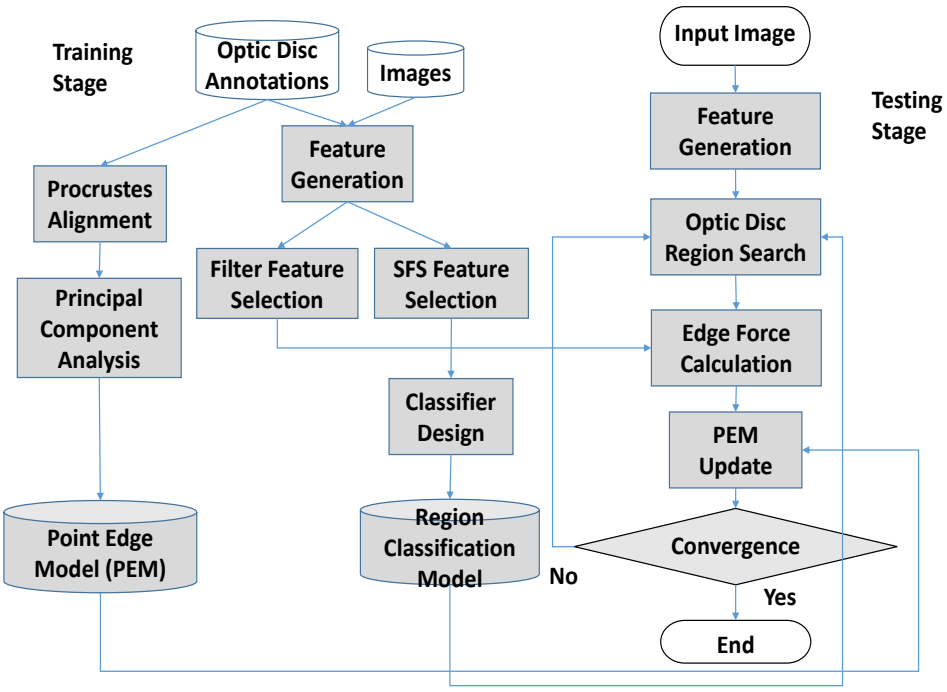

Figure 6.1: Block diagram of Point Edge and Region Classification Model for optic disc segmentation

6.3.1 Generation and Selection of Feature maps

The feature maps are generated by calculating features (Chapter 5) for each pixel of the image. We use these feature maps to classify between the region outside the boundary of the optic disc and the region inside the boundary of the optic disc. The region outside the boundary of optic disc includes the retinal area and the PPA. The region inside the boundary includes ONH rim and optic cup. Besides, the retinal vasculature area is also converged inside the ONH area and occluding the optic disc. Since the vasculature area has been segmented out (Chapter 5), therefore we can remove the vasculature by morphological inpainting. Morphological inpainting can be performed by morphological closing around different directions and retaining the maximum response for each vessel pixel. For minimum computational complexity, we have selected 8 different directions. We have used 'disk' element for morphological closing with radius equal to maximum width of the vasculature area. Since the morphological inpainting can also affect the optic disc boundary, therefore we have calculated the feature maps under two situations, i.e. 1) with vasculature removal and 2) without vasculature removal. The feature matrix can be given as:

$$FM = \begin{bmatrix} A_N^g & A_N^{gab} & A_N^{bio} & A_V^g & A_V^{gab} & A_V^{bio} \\ \\ B_N^g & B_N^{gab} & B_N^{bio} & B_V^g & B_V^{gab} & B_V^{bio} \end{bmatrix} \tag{6.1}$$

The subscript N denotes the feature maps with no-vessel removal and V denotes the other way round. These features are calculated for red and green channels in both fundus and SLO images and on different scales i.e. $\sigma = 2, 4, 8, 16$. The blue channel in fundus images has very low histogram range of grayscale value and therefore not suitable for texture analysis however, it can be used for biologically inspired features calculation (Section 4.4.1). In SLO images, the blue channel is set to zero. There are 190 feature maps in both vessel removed and non-vessel removed types; making 380 in total. We then normalize the FM using z-score normalization.

As far as feature maps are concerned, we determined two feature sets i.e. one for RCM model and one for PEM model. The feature set for the RCM model has been determined using the SFS approach since the RCM model will search the for the contour representing the optic disc region. The SFS approach will determine the

Table 6.1: Feature symbols for each feature set obtained using the SFS and Filter approaches for optic disc region determination. The detail of feature symbols can be found in Section 4.4.1

Feature Selection Approaches	Fundus Images	SLO Images
SFS Approach	$L_{uvRN}(16)$, $RG_N(4,7)$, $I_N(4,8)$, $L_{u,uRV}(16)$, $S_{RV}(2)$, $\mathcal{N}_{RV}(16)$, $L_{qq,\gamma-normGN}(8)$, $\mathcal{N}_{xGV}(16)$, G_V, $L_{qq,\gamma-normRV}(8)$	$L_{uvGV}(16)$, $L_{uvGN}(16)$, $\mathcal{N}_{yyRV}(16)$, $L_{qq,\gamma-normRV}(2)$, $L_{pp,\gamma-normRN}(8)$, $BY_V(3,7)$, $\mathcal{N}_{yyRN}(16)$, $\mathcal{N}_{xxRN}(16)$, $\mathcal{N}_{RV}(16)$, R_V
Filter Approach	$L_{uvRN}(16)$, $L_{uvRV}(16)$, $L_{qq,\gamma-normRN}(8)$, $L_{qq,\gamma-normRV}(8)$, $\mathcal{N}_{yyRN}(4)$, $\mathcal{N}_{yyRV}(4)$, $L_{u,uRN}(4)$, $L_{u,uRV}(4)$, R_N, R_V	$L_{uvGV}(16)$,$L_{qq,\gamma-normGV}(8)$, $\mathcal{N}_{yyGV}(4)$, $L_{u,uGV}(4)$, G_V, $Gb_V(x,y,90°,2,\frac{1}{10},\frac{\sqrt{2}}{10})$, $Gb_V(x,y,90°,2,\frac{1}{9},\frac{\sqrt{2}}{9})$, $Gb_V(x,y,90°,2,\frac{1}{8},\frac{\sqrt{2}}{8})$, $Gb_V(x,y,90°,2,\frac{1}{7},\frac{\sqrt{2}}{7})$, $Gb_V(x,y,90°,2,\frac{1}{6},\frac{\sqrt{2}}{6})$

features which will have highest classification power in conjunction with previously selected features (Section 4.4.2). In this way the SFS will select the features regardless of Individual Evaluation Performance (IEP) of each feature set. For RCM model, the SFS has selected 10 features beyond which there is little or no improvement as shown in Figure 6.2 (b) with blue line. The feature sets for both fundus and SLO images are capable to achieve the classification accuracy above 98%.

On the other hand, the feature set for the PEM model has been determined by selecting the features using filter approach which ranks these features according to IEP [82] (Section 4.4.2). The features with high IEP have strong edge profile and are more suitable for gradient calculation. The filter approach will select these features for PEM since it needs to update the RCM determined contour on the basis of feature maps with strong edge profiles. We have included the number of features until the mean of feature maps gradient around optic disc is the strongest. In our case, we have selected 10 features as the gradient of the regions other than optic disc would be enhanced beyond 10 and therefore affect the contour update. The features selected for both SLO images and fundus images using the SFS and Filter approaches are shown in Table 6.1.

According to Table 6.1, the selected features for fundus images and SLO images are different due to difference of gray levels in red and green channels in SLO images compared to fundus images. Also the blue channel is set to zero in SLO images which is used for calculation in 'Biologically Inspired Features'. The results of feature selection process using both SFS and Filter approach are shown in Figure 6.2.

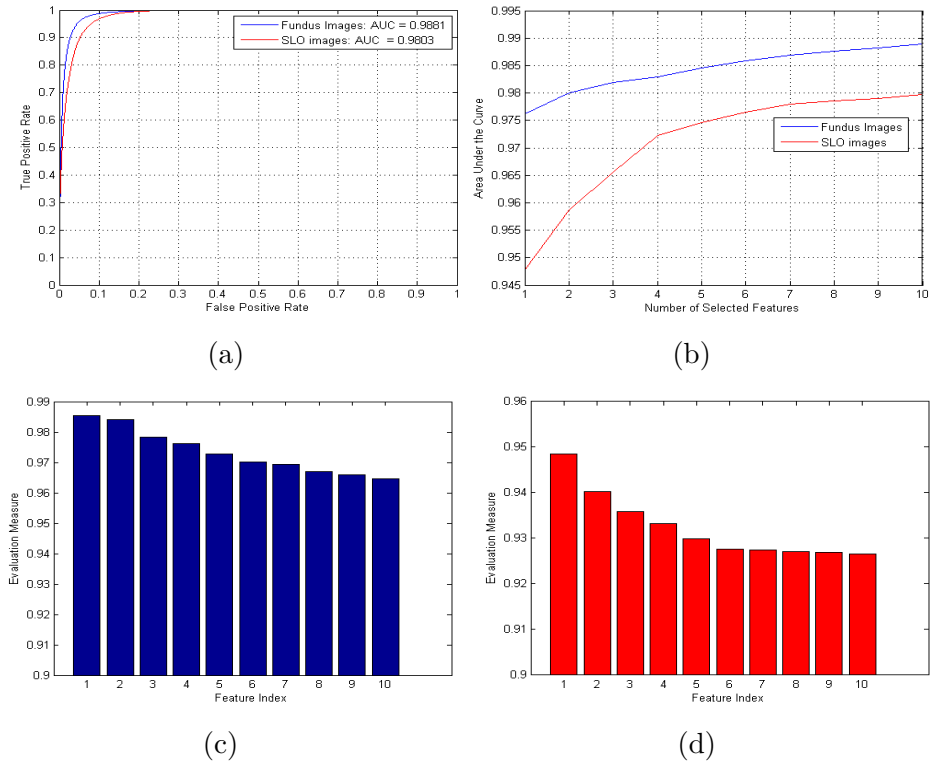

Figure 6.2: Results of feature selection procedures with (a) ROC curves of both fundus and SLO images for selected features using the SFS, (b) feature selection process using the SFS (c),(d) IEP of both fundus and SLO images respectively

Figure 6.2(a) represent the ROC curve obtained after 5-fold cross validation whereas Figure 6.2(b) shows the sequence of features selected during the SFS approach. The features shown in Table 6.1 selected by the SFS approach for both fundus and the SLO images represent the x-axis of Figure 6.2(b) whereas features selected by the Filter approach for fundus images and the SLO represent the x-axis of the Figure 6.2(c) and (d) respectively. By observing the subscript of features selected for fundus images by the SFS approach in Table 6.1, we may deduce that feature maps without vasculature removal perform better than those with vasculature removal in fundus imaging which is contradictory to what we found in our literature survey. Also there are feature maps that have a higher classification power compared to the red channel. In SLO images, we need to determine the feature maps from the green channel with the vasculature removal for better classification.

6.3.2 Region Classification Model

The *Region Classification Model* (RCM) model is generated so as to determine the optic disc region. The RCM is initialized at the optic disc centre as localized by the ONH localization method (Section 5.3). The model searches the optic disc boundary by determining the optimum profile normal to each point. In order to determine the RCM model, we perform pixelwise training on the feature maps obtained using the SFS approach. The pixelwise classification can be quite inefficient in terms of computational time and memory consumption since training and cross-validation sets will contain more than 30 images while training on fundus images as well as on SLO images separately. Therefore, we have decided to select 1000 feature map pixels from both inside and outside of the ONH from each image present in the training set.

In order to determine the classification model, we used backpropagation ANN which proved to be the fastest in terms of testing time as compared to other classifiers (Section 5.2.9). We have one hidden layer with 10 neurons in the ANN model for RCM. Also in contrast to the classification approaches as followed in [120, 126] we trained only one model for each contour point. This is because the feature map properties would be quite similar for each contour point as per retinal area and ONH rim.

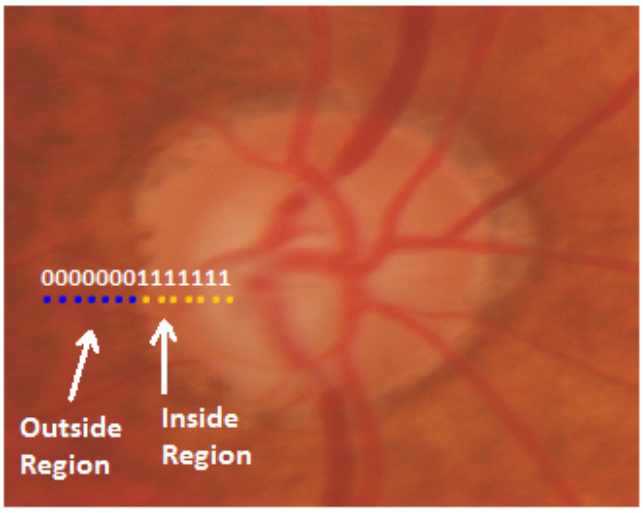

Figure 6.3: Profile sampling for region determination

Algorithm 1: Optimum profile search for optic disc region search

Input: $(X_{old}) = \{X_{old_j} | j = 1...m\}$,$m$ is number of contour points in X_{old}

n_2=number of profiles g for contour point X_{old_i} from X_{old} center to the image corner. Each g is sampled with $2n_1$ points i.e. n_1 samples to the left of profile g centre and n_1 samples to the right of the profile g centre. g is sampled on the feature maps selected using the SFS approach,

Region Classification Model (RCM)

Output: New contour Y which is the optimum boundary of the optic disc as determined by RCM

for (int j = 1;i≤m;i++) {

for (int i = 1;i≤n_2;j++){

$net_i(g)$=RCM(g)

$pf_i(g) = \frac{\sum_{i=1}^{n_1} net_i(g)}{n_1} + 1 - \frac{\sum_{i=n_1+2}^{n_1+n_1} net_i(g)}{n_1}$

}

Y_j=min(pf(g))

}

The region search procedure is illustrated in Algorithm 1. According to the algorithm, we sampled the profile of n_1 points on the line normal to contour on either sides i.e. 7 points on the right side and 7 on the left. In this way we determine around n_2 profiles by placing the contour point at different positions which are normal to original position of the contour point. An example of the profile sampling is shown in Figure 6.3. According to the figure, if the profile at the edge of the optic disc is classified, the left hand side samples should be classified as part of the retina whereas right hand side samples should be classified as part of ONH rim. This type of classification is quite effective in avoiding PPA or vasculature occlusion. Also the output of the neural

networks is in the form of weights representing relevance to the respective classes. For example if we treat the ONH area as class 1 and the retinal area as class 0 then the weights would be in between 0 and 1. In order to determine optimum profile we used the following formula:

$$pf(g) = argmin(\frac{\sum_{i=1}^{n_1} net_i(g)}{n_1} + 1 - \frac{\sum_{i=n_1+2}^{n_1+n_1} net_i(g)}{n_1}) \tag{6.2}$$

where $net_i(g)$ is the neural weight of the respective profile at sample i. The minimization of neural weights sum outside the ONH boundary and the maximization of neural weights sum inside the boundary can result in optimum profile close to the boundary of the optic disc.

6.3.3 Point Edge Modeling

In order to update the contour obtained from the RCM according to the edge of the optic disc, we have determined *Point Edge Model* (PEM). The PEM in conjunction with the RCM combine to form the iterative procedure of PERCM. The PEM will initialize the RCM, update the contour obtained from RCM and generate the condition of iterative procedure of PERCM. The PEM is composed of following steps:

1. Contour Generation for RCM Initialization.

2. PEM Model Update.

3. Generation of Iterative Procedure Condition.

1) Contour Generation for RCM Initialization

In every iteration of PERCM, the contour for RCM is initialized from the previous iterative step. In first iteration, the contour is initialized by mean of the shapes present in the training set. In order to calculate the mean of shapes in the training set, we need to align the shapes using Procrustes alignment [119]. The shape alignment aims to transform all training set shapes into a common coordinate frame.

In Procrustes alignment, the shape of an optic disc in a two-dimensional (2-D) image can be described by a set of n landmarks. These landmarks are manually annotated to describe the disc shape in a retinal image. Each shape can be described as a vector of n coordinate pairs having $2n$ elements as mentioned below:

$$\mathbf{v} = [(x_1, y_1), (x_2, y_2), ..., x_n, y_n]^T. \tag{6.3}$$

The task of shape alignment can be achieved by three transformation steps: centralization, scaling and orientation. For centralization, the centroid of each landmark shape is calculated as the average position of all its landmarks, then the shape is translated to its local origin by subtracting its centroid (see Figure 6.4(b)). The centroid of the shape can be represented as:

$$\mathbf{v}_{cent} = (\bar{x}, \bar{y}) = (\frac{1}{n}\sum_{j=1}^{n} x_j, \frac{1}{n}\sum_{j=1}^{n} y_j). \tag{6.4}$$

After translation to the origin, we need to normalize all shapes with zero mean and unit variance of each contour point present in the shape. The shapes can be normalized (see Figure 6.4(c)) using the Frobenius norm (2-norm) [119] equation as:

$$\mathbf{v}_{norm} = \frac{\mathbf{v}_{trans}}{norm(\mathbf{v}_{trans})}, \tag{6.5}$$

where,

$$\mathbf{v}_{trans} = \mathbf{v} - \mathbf{v}_{cent} \tag{6.6}$$

and

$$norm(\mathbf{v}) = \sqrt{{x_1}^2 + {y_1}^2 + ... + {x_n}^2 + {y_n}^2} \tag{6.7}$$

The annotations for the left and the right eyes are usually performed in different directions, i.e. clockwise and in anti-clockwise directions, we then need to flip the annotations of the left eye to lie in same direction to that of the right eye in order to perfectly align them as shown in Figure 6.4(d).

Finally, we obtain the mean of N aligned shapes present in the training set as:

$$\bar{X} = \frac{1}{N}\sum_{i=1}^{N} {\mathbf{v}^i}_{norm}. \tag{6.8}$$

2) PEM Model Update

In this model, we have calculated the force field in order to update the model towards optimum edge. The force field of the image can be represented as:

$$\mathbf{f} = \nabla(I(x, y)). \tag{6.9}$$

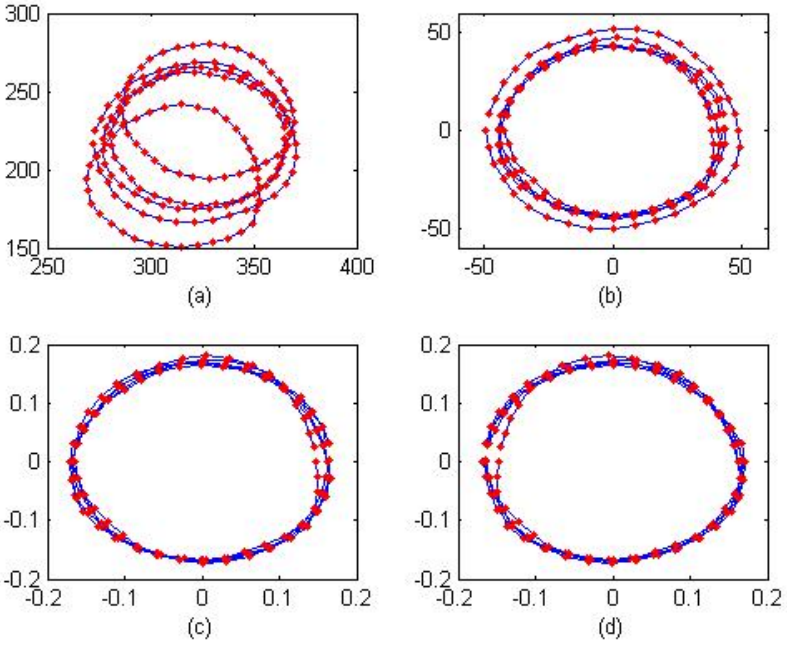

Figure 6.4: Alignment procedure of the optic disc shapes. The shapes are represented (a) in an original image, (b) after translation to the origin, (c) after normalization and (d) after flipping the annotations of left eyes so that the annotation direction of both the eyes would be same

where ∇ is the gradient map of the image. If the image is in the form of binary edge map (f_{edge}), it can represent the force field of the image as $\mathbf{f} = f_{edge}$. The force field has been calculated on the feature maps using the filter approach. This is in contrast to the techniques discussed in literature which have used red channel of the coloured fundus photograph for optic disc segmentation. In order to determine the edge force of the optic disc boundary, one could use Gradient Vector Field (GVF) [136]. Although GVF has a large capture range of detecting edges and ability to capture boundary concavities, it is quite sensitive to noise and has a high computational cost. Therefore we have decided to use *Kernel Vector Field* (KVF) which can be calculated by convolving the image edge map $f_{edge}(x, y)$ with kernel $\mathbf{k}(x, y)$ as shown in Equation (6.10). It has not only a large capture range and the ability to capture boundary concavities but also has reduced computational cost and a superior robustness to noise [78].

$$\mathbf{f}_{kvf} = f_{edge}(x, y) * \mathbf{k}(x, y) \tag{6.10}$$

Different values of the kernel $\mathbf{k}(x, y)$ are optimal for different shapes. In our case, optic disc has a circular shape. Consider the optic disc centre is at origin (0,0) and

the distance from the centre along x-axis and y-axis can be stated as (x,y). We can define radial power kernel using Equation (6.11) (6.12) (6.13):

$$\mathbf{k}(x,y) = m(x,y)\mathbf{n}(x,y) \tag{6.11}$$

where $m(x,y)$ is magnitude of the vector at (x,y) and $\mathbf{n}(x,y)$ is unit vector pointing to the origin $(0,0)$, defined as:

$$\mathbf{n}(x,y) = [\frac{-x}{r}, \frac{-y}{r}] \tag{6.12}$$

where $r = \sqrt{x^2+y^2}$, and

$$m(x,y) = (\sqrt{(x^2+y^2)} + \epsilon)^{-\gamma} \tag{6.13}$$

ϵ is small positive constant to prevent division by zero whereas γ is determined empirically as 1.5. Lower the value of γ, more influential would be the force field of the object of interest (in this case it is optic disc). The KVF is noise invariant compared to GVF which can be illustrated in Figure 6.5. Here a value of $r = 150$ which is the estimated value of the radius of optic disc in a 701x701 image. In the edge map shown in Figure 6.5(b) there are false edges inside the optic disc boundary which are misguided by GVF. However, force field calculated by KVF is directed towards the optic disc boundary.

In Equation (6.10), we determined f_{edge} by taking the mean of edge maps obtained after taking the gradient of feature maps selected from filter approach. It can be mentioned in the form of equation as:

$$f_{edge} = \frac{\sum_{i=1}^{n} \nabla(\Lambda_i)}{n} \tag{6.14}$$

where ∇ represent gradient operation, Λ_i is the ith feature map obtained after ranking feature maps using filter approach and selecting n features. The filter approach ranks the features according to strongest edge profiles around the optic disc. We have included the number of features n until the mean of feature maps gradient around optic disc is the strongest. In our case n=10. For a binary edge map, we can apply Canny edge detector on f_{edge} [52]. So Equation (6.10) can be re-written as:

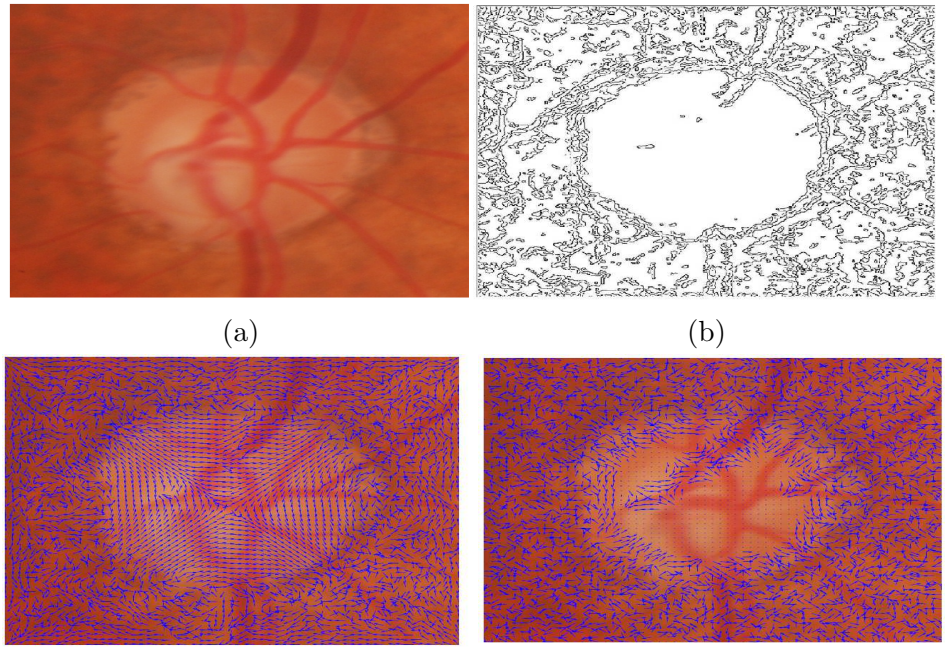

Figure 6.5: Comparison of GVF and KVF in calculating force field where, (a) colour fundus image, (b) binary edge map obtained using Canny edge detector, (c) force field using KVF and (d) shows force field using GVF. The comparison of (c) and (d) shows f_{kvf} is not misguided by false edge within the optic disc as in case of f_{gvf} in (d).

$$\mathbf{f}_{kvf} = \frac{\sum_{i=1}^{n} \nabla(\Lambda_i)}{n} . * \mathbf{k}(x, y) \tag{6.15}$$

where, $.*$ represent pixelwise multiplication.

The force field $\mathbf{f}_{kvf}$ can be used in PEM for model update. Based on [138, 143], the PEM model can be given as:

$$X = X' + w\ sign(\mathbf{f}(X'))\ exp^{-|\mathbf{f}(X')|}, \tag{6.16}$$

where X and X' are current and previous contours respectively. w is a step size value that is empirically selected as 2, $\mathbf{.}$ represent multiplication. In our case, $\mathbf{f} = \mathbf{f}_{kvf}$. The Equation (6.16) can be rewritten as:

$$X = X' + w\ sign(\mathbf{f}_{kvf}(X'))\ exp^{-|\mathbf{f}_{kvf}(X')|}, \tag{6.17}$$

3) Generation of Iterative Procedure Condition

As far as generation of iterative procedure condition is concerned, the PERCM tend to keep the contour consistent with the training shapes. Therefore, the iterative procedure of PERCM will continue until the condition of minimum error between the contour and the mean of training shapes is achieved. In order to generate the condition, we have determined eigen values and eigen vector. This can be generated as:

$$[\Phi, \lambda] = eig(S) \tag{6.18}$$

where, $\Phi = (\phi_1, \phi_2, ..., \phi_t)$ is a set of t eigen vectors corresponding to the largest t values of the covariance matrix of the training shapes S and $\lambda = (\lambda_1, \lambda_2, ..., \lambda_t)$ is the set of t eigen values. The covariance matrix can be given as:

$$S = \frac{1}{N-1} \sum_{i=1}^{N} (\mathbf{v}^i{}_{norm} - \bar{X})(\mathbf{v}^i{}_{norm} - \bar{X})^T. \tag{6.19}$$

In order to generate the iterative procedure condition, we know that statistical shape modeling is a method for building a model by learning patterns of variability from a training set of shapes in the form of annotations [33, 127]. Using the statistical shape modeling, the optic disc can be approximated as:

$$X \approx \bar{X} + \Phi \mathbf{b}, \tag{6.20}$$

where the vector $\mathbf{b}$ defines a set of parameters of a deformable model. By varying the elements of $\mathbf{b}$, we can vary the shape. The Equation (6.20) can be re-written as:

$$\mathbf{b} = \Phi_(1 : j)^T (X - \bar{X}). \tag{6.21}$$

where j is total number of eigen values and eigen vector used. The iterative procedure condition can be given as $|\mathbf{b}| < 3\sqrt{\lambda_{1:j}}$, where $\sum_{l=1}^{j} \lambda_j = 0.98 * \sum_{l=1}^{t} \lambda_j$.

6.3.4 The PERCM Algorithm

The PERCM is an iterative search procedure to update the model in every iteration. In order to search for the optic disc region, we need to determine the feature maps selected during the SFS approach. At the start of an iteration, X, which is initially

$\bar{X}$ is transformed from zero mean space into the colour space. This can be achieved by using Equation (6.22):

$$T_{X_t,Y_t,s,\theta} = \begin{bmatrix} X_t \\ \\ Y_t \end{bmatrix} + \begin{bmatrix} s\cos\theta & -s\sin\theta \\ \\ s\sin\theta & s\cos\theta \end{bmatrix} \begin{bmatrix} X_x \\ \\ X_y \end{bmatrix}, \tag{6.22}$$

where (X_t, Y_t)=translational parameters, s=scaling parameter, θ=rotational parameter, X_x and X_y are x-coordinates and y-coordinates of the model respectively. Initially θ is set to zero whereas $s = \frac{\mathbf{v}_{trans}}{\mathbf{v}_{norm}}$ from Equation (6.5). X is placed approximately at the center of the optic disc. The contour points are moved according to RCM model (Section 6.3.2). The contour is then approximated according to *mean* shape of the training set. Then we apply PEM for model update. The test algorithm can be summarized in Algorithm 2 as:

Algorithm 2: PERCM Algorithm

1. Calculate feature maps on the basis of SFS and Filter approaches.
2. Initialize $X = \bar{X}$
3. while $|\mathbf{b}| \geq |3\sqrt{\lambda_i}|$ {
   - i $X_{old} = T_{X_t,Y_t,s,\theta}(X)$.
   - ii Determine new contour $\mathbf{Y}$ on the basis of SFS feature maps, RCM model and Equation (6.3) (See Algorithm 1).
   - iii Find the transformation parameters (X_t, Y_t, s, θ) which best maps X to $\mathbf{Y}$. This can be estimated as:

$$[\hat{X}_t, \hat{Y}_t, \hat{s}, \hat{\theta}] = argmin[\sum_{i=1}^{n} |\mathbf{Y}(n) - \bar{X}(n)|^2], \tag{6.23}$$

   - iv $X'_{new} = T_{\hat{X}_t,\hat{Y}_t,\hat{s},\hat{\theta}}(X)$
   - v Update $X_{new} = X'_{new} + w\ sign(\mathbf{f}_{kvf}(X'_{new}))\ exp^{-|\mathbf{f}_{kvf}(X'_{new})|}$,
   - vi Invert the transformation function and use to project $\mathbf{Y}$ into model coordinate frame.

$$y = {T_{\hat{X}_t,\hat{Y}_t,\hat{s},\hat{\theta}}}^{-1}(\mathbf{Y}) \tag{6.24}$$

   - vii Update the model parameters to match y

$$b = \Phi^T(y - \bar{X}). \tag{6.25}$$

   - viii $X = {T_{\hat{X}_t,\hat{Y}_t,\hat{s},\hat{\theta}}}^{-1}(X_{new})$
   - ix $[X_t, Y_t, s, \theta] = [\hat{X}_t, \hat{Y}_t, \hat{s}, \hat{\theta}]$ }
4. end

6.4 Experimental Evaluation

We have performed 5-fold cross validation on both 102 SLO and 120 fundus images (see Section 6.2 for ground truth). The accuracy of the optic disc segmentation method has been measured using Dice Coefficient. It can be calculated as:

$$D_{od} = \frac{2(|onh_1 \cap onh_2|)}{|onh_1| + |onh_2|} \tag{6.26}$$

where $|onh_1|$ and $|onh_2|$ are the ONH pixels obtained from the benchmark and automatic segmentation respectively. Initially, the results are compared across annotation of different experts in Drishti-GS and RIM-ONE since they have the optic disc annotation marked by more than one expert. The results are shown in Table 6.2. The comparison shows high inter-observer similarity among the experts as well as mean of all annotations. Therefore, the comparison among different methods is performed with respect to mean of all the annotations.

Table 6.2: Comparison of results of PERCM among different experts and mean of annotation of all experts

Datasets	Expert 1	Expert 2	Expert 3	Expert 4	Expert 5	Mean
RIM-ONE	0.93 ± 0.05	0.92 ± 0.06	0.92 ± 0.06	0.92 ± 0.07	0.93 ± 0.05	0.94 ± 0.05
Drishti-GS	0.95 ± 0.04	0.96 ± 0.03	0.97 ± 0.02	0.96 ± 0.01	N/A	0.97 ± 0.02

The PERCM results are compared with some popular statistical and freeform modeling approaches i.e. Active Shape Model (ASM) [33], Chan-Vese model [28] and GVF snake model [70]. The built-in code for these models are available in Mathworks Central. For these models, we have used the default input parameters however, the variation of the parameters made little difference. The Chan-Vese and GVF models have been converged in 1000 iterations. The comparison results are shown in Table 6.3. The results show that PERCM has outperformed these models in terms of segmentation accuracy.

The RIM-ONE and SLO datasets have been annotated with normal and glaucomatous images. The comparison of segmentation accuracy in terms of normal and glaucomatous images has been been shown in Table 6.4. The results show that segmentation accuracy in terms of normal images was better compared to glaucoma images.

If we compare ASM with Chan-Vese model, the Chan-Vese model has performed better in case of normal images however, it has been misguided by PPA in glaucomatous images. Nevertheless, our proposed approach performed significantly especially in case of RIM-ONE glaucomatous images. As far as SLO images are concerned, the PERCM is not able to perform that better as it was the case in fundus images. This might be the case due to low resolution of optic disc area as SLO images cover a large FOV of retina and optic disc is very small area of it.

Also by observing Figure 6.7, we can visualize the PERCM performs significantly better than other methods on the ONH image with PPA. Other examples of PERCM on different images of Drishti-GS, Optomaps and RIM-ONE have been shown in Figure 6.6. We can deduce that the PERCM has not been misguided by PPA as the part of optic disc or vasculature occlusion. The PERCM can converge within 3 iterations on each image with time taken at each iteration is 2 seconds at Intel Core i7-2600 CPU with 16GB DDR3-1333 RAM.

Table 6.3: Comparison of results of PERCM with freeform and statistical shape models

Datasets	Active Shape Model	Chan-Vese Model	GVF Snake Model	**PERCM**
RIM-ONE	0.89 ± 0.06	0.89 ± 0.10	0.87 ± 0.15	0.94 ± 0.05
Drishti-GS	0.91 ± 0.05	0.94 ± 0.04	0.95 ± 0.02	0.97 ± 0.02
SLO images	0.81 ± 0.09	0.73 ± 0.14	0.66 ± 0.14	0.90 ± 0.07

Table 6.4: Comparison of results of PERCM with freeform and statistical shape models in terms of healthy and glaucomatous images

	RIM-ONE		Optomaps	
	Normal	Glaucoma	Normal	Glaucoma
Active Shape Model	0.91 ± 0.06	0.87 ± 0.09	0.82 ± 0.10	0.80 ± 0.08
Chan-Vese Model	0.92 ± 0.06	0.84 ± 0.12	0.75 ± 0.13	0.72 ± 0.15
GVF Snake Model	0.87 ± 0.14	0.87 ± 0.16	0.66 ± 0.14	0.66 ± 0.14
PERCM	0.95 ± 0.03	0.92 ± 0.07	0.91 ± 0.07	0.89 ± 0.07

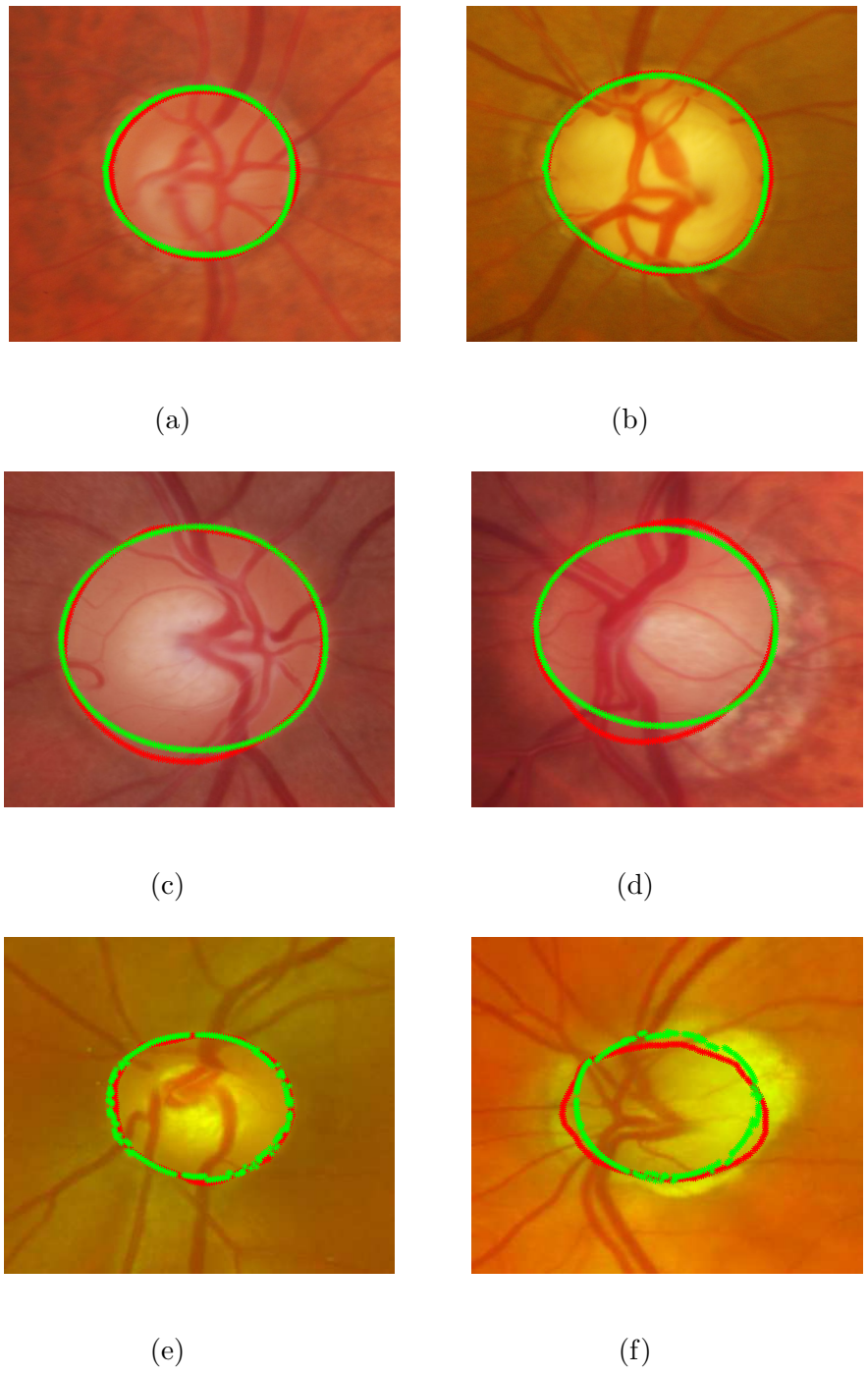

Figure 6.6: Examples of optic disc determination (a),(b) are examples from Drishti-GS database, (c),(d) are examples from RIM-ONE and (e),(f) are examples from Optomaps. The red outline shows the original annotation around optic disc whereas the green outline shows the automatic annotations from the PERCM

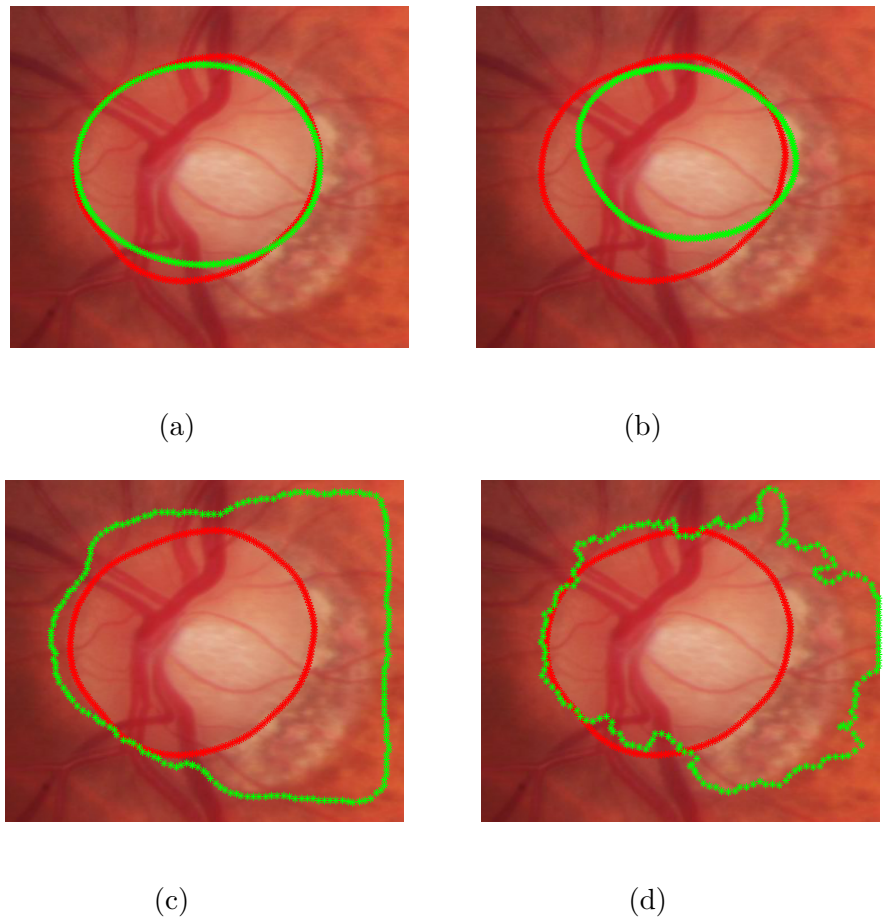

(a) (b)

(c) (d)

Figure 6.7: Visual comparison of the PERCM with other models which were applied on the ONH images with PPA. The images show the result of (a) **PERCM**, (b) ASM, (c) Chan-Vese model and (d) GVF snake contour

6.5 Conclusion

In this chapter we have proposed the combination of *Point Edge Model* (PEM) and *Region Classification Model* (RCM) entitled *Point Edge and Region Classification Model* for the determination of optic disc boundary. The PERCM initially determines the optic disc region on the basis of *Region Classification Model* (RCM) and then updates the optic disc contour using force field based *Point Edge Model* (PEM). The model has been tested against different databases of SLO and fundus images. The average segmentation accuracy achieved by the model on Drishti-GS, RIM-ONE and Optomaps is 97%, 94% and 90% respectively. The experimental evaluation indicates that our method outperforms the previous popular statistical shape and freeform modeling approaches. Besides, our method has been tested on different datasets which indicates a high robustness of our method. An accurate segmentation of optic disc is useful

for accurate segmentation of the optic cup as well as glaucoma related geometrical symptoms such as the CDR etc.

Chapter 7

Optic Cup Segmentation

7.1 Introduction

In this chapter we will discuss optic cup segmentation which is the next step after optic disc segmentation. The procedure of optic cup segmentation is similar to that of optic disc except there are variations in terms of initialization and force calculation. The reason is that size of the optic cup is too small to run the region search along normal line profiles. Also the optic cup has no clear gradient compared to that of optic disc. Therefore it is a challenging task to determine the boundary of the optic cup. In order to address these issues, we have developed two models. *Region Classification Model* (RCM) is proposed for classification between optic cup and the rim area. On the other hand, *Weighted Point Edge Model* (WPEM) determines the force field using the weighted feature maps calculated by the RCM for optic cup in order to enhance the optic cup region compared to rim area in the ONH.

7.2 Ground Truth

For training and evaluation of the models, we have two datasets:

Fundus Images: For fundus images, we have used Drishti-GS dataset. The Drishti-GS dataset has been annotated around optic cup by four experts. There are 50 images in the training set with resolution of 701 x 701 of the ONH cropped image. However, there are no disease annotations in Drishti-GS dataset.

SLO Images: In SLO images, the optic cup has been annotated by one expert

in the retinal scan with the suspected glaucoma patients. Therefore we have 51 SLO images with optic cup annotation and the resolution of 341 x 341 of the ONH cropped image.

7.3 Weighted Point Edge and Region Classification Model

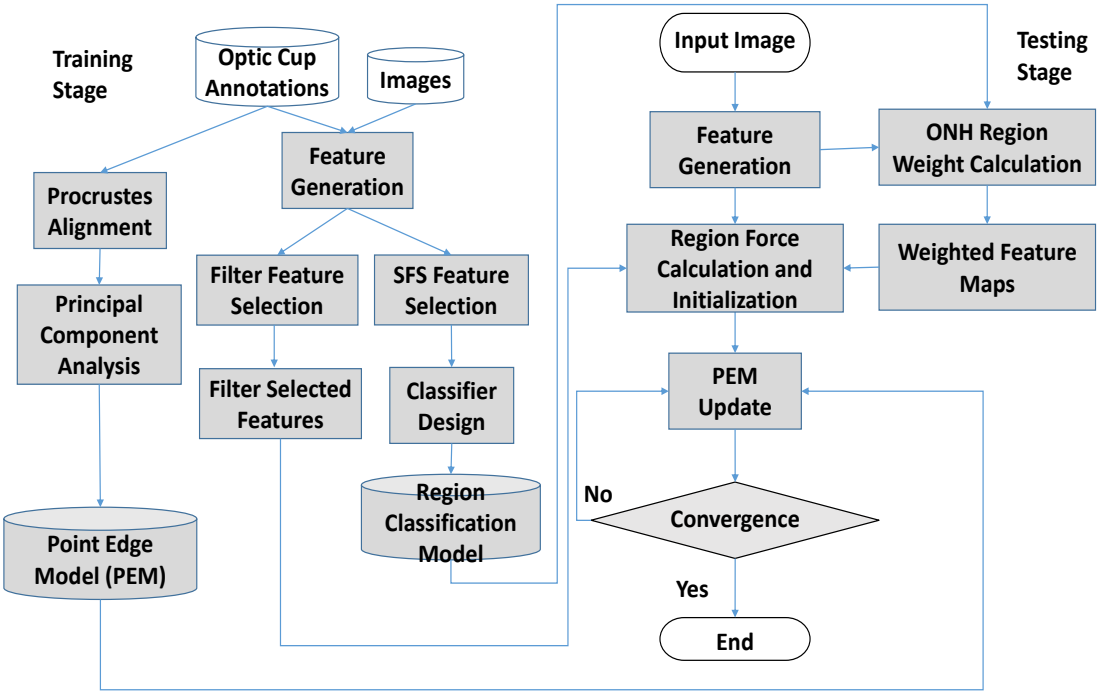

Figure 7.1: Block diagram of the Weighted Point Edge and Region Classification Model for optic cup segmentation

In the *Weighted Point Edge and Region Classification Model* (WPERCM) for optic cup segmentation, the *Weighted Point Edge Model* (WPEM) updates the contour using the force field determined by the weighted feature maps. The weighted feature maps are obtained by multiplying the IEP selected feature maps by classifier weights obtained from the RCM of the ONH region classification in order to strengthen the optic cup region compared to the rim area. The block diagram is shown in Figure 7.1. In the following subsections, we will discuss the following:

1. Generation and selection of feature maps.

2. Region force calculation.

3. Testing algorithm.

7.3.1 Generation and Selection of Feature Maps

The feature maps for optic cup segmentation are generated so as to distinguish between cup area and the ONH rim area. Like optic disc segmentation, we have calculated feature maps using both approaches, i.e. 1) with vasculature removal and 2) without vasculature removal. The feature matrix can be given as that in Equation (6.1) which is the z-score normalized. Also, we have used both filter approach and the SFS approaches for selecting two types of feature sets which are different for both the SLO and fundus images. During fundus images training, we have only used features from Drishti-GS dataset since there are no annotations for optic cup in RIM-ONE dataset. The features selected for both the SLO images and fundus images using the SFS and Filter approaches are shown in Table 7.1 and their performance is illustrated in Figure 7.2

Table 7.1: Feature sets obtained using the SFS and Filter approaches for optic cup region determination. The detail of feature symbols can be found in Section 4.4.1.

Feature Selection Approaches	Fundus Images	SLO Images
SFS Approach	$L_{uvRV}(16)$, $\mathcal{N}_{yyRV}(2)$, $L_{pp,\gamma-normRV}(16)$, $L_{u,uGN}(16)$, $L_{qq,\gamma-normGN}(2)$, $RG_N(4,7)$, $L_{u,uGV}(16)$, $\mathcal{N}_{yyRV}(16)$, $BY_N(4,8)$, $\mathcal{N}_{xyRV}(8)$, $I_V(4,8)$, $I_V(4,7)$, $I_V(3,7)$, $L_{uvGN}(16)$, $L_{uvRN}(16)$	$L_{u,uRN}(4)$, $BY_N(4,8)$, $L_{pp,\gamma-normGN}(8)$, $BY_V(4,7)$, $L_{uuRN}(4)$, $\mathcal{N}_{yyRN}(16)$, $BY_N(2,5)$, $L_{uvGV}(2)$, $L_{u,uRV}(2)$, $L_{qq,\gamma-normGN}(2)$, $L_{u,uGN}(16)$, $RG_V(4,8)$, $RG_N(4,8)$, $\mathcal{N}_{yyGV}(16)$, $L_{qq,\gamma-normGN}(8)$
Filter Approach	$L_{uvRV}(16)$, $L_{qq,\gamma-normRV}(8)$, $\mathcal{N}_{yyRV}(4)$, $L_{u,uRV}(4)$, R_V, $L_{uvRN}(16)$, $L_{qq,\gamma-normRN}(8)$, $\sqrt{\mathcal{N}^2{}_{xRV}(2)+\mathcal{N}^2{}_{yRV}(2)}$, $\mathcal{N}_{yyRN}(4)$, $L_{uuRN}(4)$,R_N, $\mathcal{N}_{xRV}(2)$, $\mathcal{N}_{xyRV}(2)$, $\mathcal{N}_{xxRV}(4)$, $\mathcal{N}_{yRV}(4)$	$L_{u,uRN}(4)$, R_N, $\mathcal{N}_{yyRN}(4)$, $L_{qq,\gamma-normRN}(8)$, $\mathcal{N}_{yyRN}(2)$, $\mathcal{N}_{xyRN}(2)$, $\mathcal{N}_{xRN}(2)$, $L_{uvRN}(16)$, $L_{uuRN}(4)$, $\mathcal{N}_{xyRN}(16)$, $\mathcal{N}_{RN}(4)$, $L_{pp,\gamma-normRN}(4)$, $L_{u,uRV}(4)$, $\mathcal{N}_{yyRV}(4)$, $\mathcal{N}_{xxRV}(2)$

Here we have also selected two types of feature set i.e. feature set for RCM model and the feature set for WPEM model. The feature set with high classification power, we selected 15 features for both the SLO and fundus images since there was little improvement in classification performance beyond that. In case of WPEM model the first 10 to 15 features ranked by filter approach are sufficient for determining strongest boundary around optic cup. Keeping the consistency with the number of features selected for RCM, we have selected 15 features for WPEM model. This accounted for

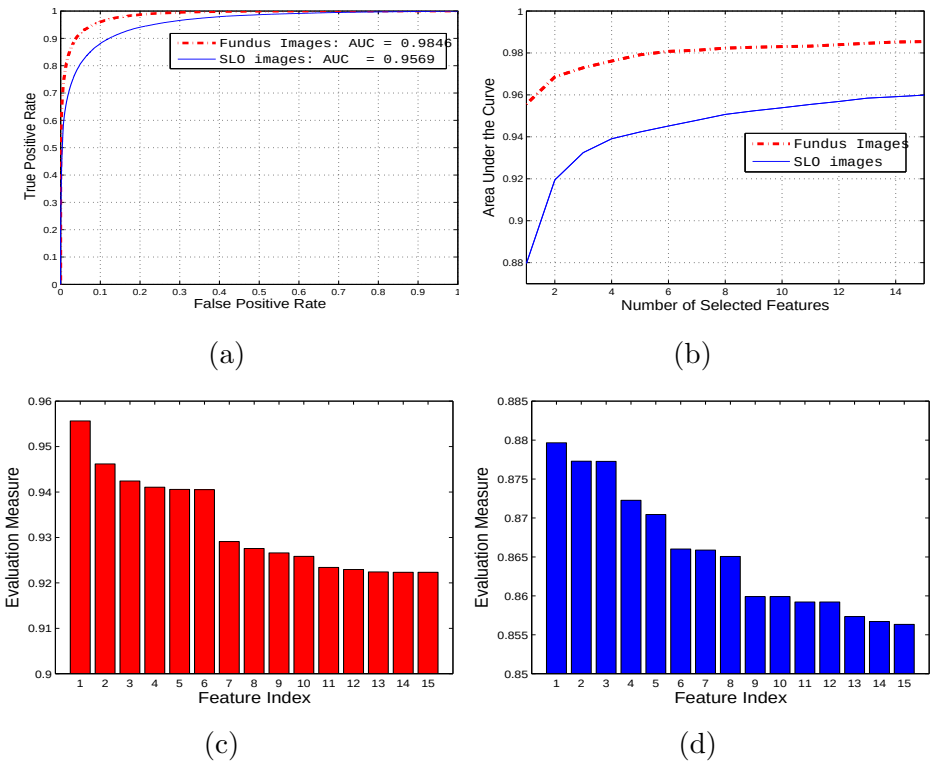

(a) (b)

(c) (d)

Figure 7.2: Results of feature selection procedures with (a) ROC curves of both fundus and the SLO images for selected features using the SFS, (b) feature selection process using the SFS (c),(d) IEP of both fundus and the SLO images respectively

the features with IEP greater than 0.9 for fundus images and 0.85 for SLO images. The subscript of the features in Table 7.1 shows that feature sets are composed of hybrid combination of red and green channel. This was in contrast to the works in literature survey which used only green channel for cup segmentation.

7.3.2 Region Force Calculation

1) ONH Region Classification

After the determination of feature sets, the next step is to classify the ONH region into rim area and cup area. This can be performed using the RCM model by training the pixelwise classification model on the feature maps obtained using the SFS approach. We have randomly selected 1000 feature map pixels from each of rim area and cup area from each image present in the training set so as to avoid large training set for pixelwise classification. We have then performed classification using neural weights. After the classification, we obtain the classification map of neural weights (Net_c) shown

in Figure 7.3(b).

2) Region Force Calculation and WPEM Update

Since the gradient is very weak between boundary of the rim and the cup, therefore we have performed the pixelwise multiplication between classification map(Net_c) and the feature maps selected using filter approach. The purpose of performing the multiplication is to enhance the gradient for determining optic cup boundary. For determination of region force, we determined the *Kernel Vector Field* (KVF) using Equation (7.1)

$$\mathbf{f}_{kvf} = f_{region}(x, y) * \mathbf{k}(x, y) \tag{7.1}$$

where $\mathbf{k}(x, y)$ can be calculated using Equation (6.11), (6.12) and (6.13). For optic cup, r in Equation (6.12) can be in the range of 20% to 80% to the r of optic disc. For γ in Equation (6.13), we selected the value 0.5 to make the optic cup force field more influential since lowering γ value in the equation will increase the magnitude of the force field. In Equation (7.1), we determined f_{region} as:

$$f_{region} = \sum_{i=1}^{n} \nabla(\Lambda_i . * Net_c) \tag{7.2}$$

where Λ_i is the ith feature map obtained after ranking feature maps using filter approach and selecting n features. In our case n=15. $.*$ is the pixelwise multiplication. So Equation (7.1) can be re-written as:

$$\mathbf{f}_{kvf} = \sum_{i=1}^{n} \nabla(\Lambda_i . * Net) * \mathbf{k}(x, y) \tag{7.3}$$

The visual result of $\mathbf{f}_{kvf}$ are shown in Figure 7.3e. For comparison, we calculated the force field using the f_{region}=f_{edge}, where value of f_{edge} is calculated from Equation (6.14). The region force field $\mathbf{f}_{kvf}$ can be used in WPEM for model update. We can deduce WPEM as:

$$X = X' + w\ sign(\mathbf{f}_{kvf}(X'))\ exp^{-|\mathbf{f}_{kvf}(X')|}, \tag{7.4}$$

where X and X' are current and previous contours respectively. w is the step size parameter is empirically selected as 5.

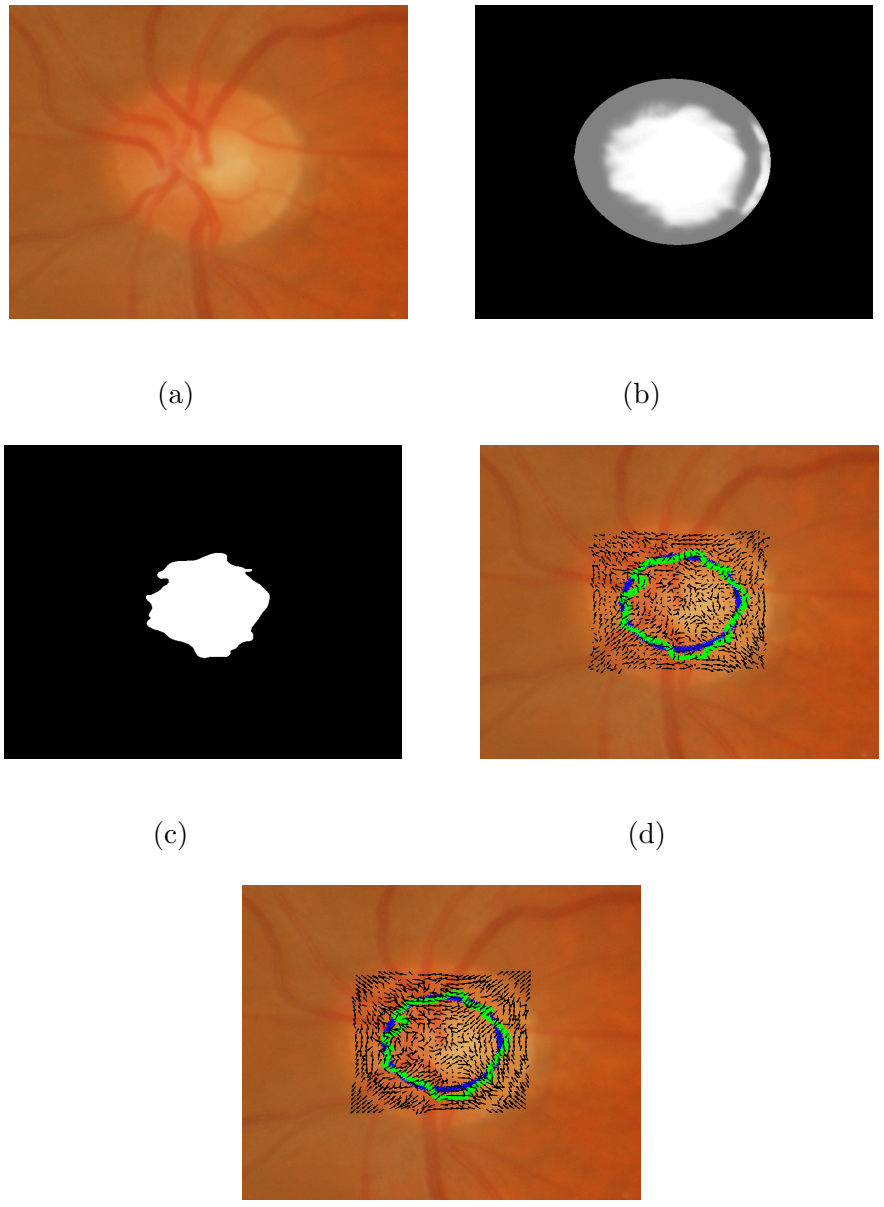

(a) (b)

(c) (d)

(e)

Figure 7.3: An example of determination of classification map and force calculation with (a) original image, (b) classification map of the neural weights, (c) pixels with neural membership value greater than 90%. (d) and (e) shows the comparison of force field calculated for optic cup of (d) feature maps and (e) feature maps multiplied by neural weights. The feature maps multiplied by neural weights have stronger force field around optic cup

Algorithm 3: The WPERCM Algorithm

1. Calculate feature maps on the basis of SFS and Filter approaches using X_{old}.
2. Initialize $X = \bar{X}$
3. while $|\mathbf{b}| \geq |3\sqrt{\lambda_i}|$ {
   - i $X_{old} = T_{X_t,Y_t,s,\theta}(X)$.
   - ii Determination of Net_c using RCM model.
   - iii $f_{region} = \sum_{i=1}^{n} \nabla(\Lambda_i . * Net_c)$
   - iv $Y = (Net_c >= 1.9)$
   - v Find the transformation parameters (X_t, Y_t, s, θ) which best maps X to $\mathbf{Y}$. This can be estimated as

$$[\hat{X}_t, \hat{Y}_t, \hat{s}, \hat{\theta}] = argmin[\sum_{i=1}^{n} |\mathbf{Y}(n) - \bar{X}(n)|^2] \tag{7.5}$$

   - vi $X'_{new} = T_{\hat{X}_t,\hat{Y}_t,\hat{s},\hat{\theta}}(X)$
   - vii Update $X_{new} = X'_{new} + w\ sign(\mathbf{f}_{kvf}(X'_{new}))\ exp^{-|\mathbf{f}_{kvf}(X'_{new})|}$,
   - viii Invert the transformation function and use to project $\mathbf{Y}$ into model coordinate frame.

$$y = {T_{\hat{X}_t,\hat{Y}_t,\hat{s},\hat{\theta}}}^{-1}(\mathbf{Y}) \tag{7.6}$$

   - ix Update the model parameters to match y

$$b = \Phi^T(y - \bar{X}). \tag{7.7}$$

   - x $X = {T_{X_t,Y_t,s,\theta}}^{-1}(X_{new})$
   - xi $[X_t, Y_t, s, \theta] = [\hat{X}_t, \hat{Y}_t, \hat{s}, \hat{\theta}]$

   } **end**

7.3.3 The WPERCM Algorithm

The WPERCM starts with the ONH classification between the rim area and cup area. After classification, we have the classification map of neural weights. In a classification map, we select only those pixels for which we are 90% sure of being the part of optic disc. The weights of the classification map are distributed between 1 and 2. We will select those weights which are having the value greater than 1.9. The final mask will be used for determining the contour Y. The mask is shown in Figure 7.3(c). The testing algorithm is mentioned in Algorithm 3.

7.4 Experimental Evaluation

Neither of these datasets have disease annotations. Therefore we have not provided the comparison of optic cup segmentation accuracy in terms of normal and glaucomatous images. For determination of optic cup segmentation accuracy, we have cross-validated across Optomaps and Drishti-GS database using 5-fold cross validation. The segmentation accuracy for optic cup can be calculated using the dice coefficient mentioned as follows:

$$D_{oc} = \frac{2(|Rim_1 \cap Rim_2| + |OC_1 \cap OC_2|)}{N_{tot}} \tag{7.8}$$

where Rim_1 and Rim_2 are the rim pixels and OC_1 and OC_2 are the optic cup pixels obtained from the benchmark and the automatic segmentation respectively. Also, $N_{tot} = Rim_1 + Rim_2 + OC_1 + OC_2$. Like in case of optic disc segmentation, we have determined the segmentation accuracy of optic cup across different experts as well as mean of all annotations. This can be possible in Drishti-GS dataset since optic cup in SLO images have been annotated by only one expert. The comparative results of optic segmentation accuracy across different experts has been shown in Table 7.2. The comparative results across different experts show low inter-observer variability.

The optic cup segmentation results are shown in Table 7.3. The results are compared with the ASM [33] and Chan-Vese model [28]. Chan-Vese model is the active contour modeling without edges which is usually used in the cases when the gradient of the object is not prominent. ASM is the most popular example of statistical shape modeling. We have used built-in codes for ASM and Chan-Vese model obtained from

Table 7.2: Optic cup segmentation performance comparison in Drishti-GS by WPERCM across different experts and mean of annotations of all experts

Datasets	Expert 1	Expert 2	Expert 3	Expert 4	Mean
WPERCM	0.84 ± 0.11	0.86 ± 0.10	0.85 ± 0.08	0.81 ± 0.09	0.87 ± 0.09
Active Shape Models	0.71 ± 0.15	0.66 ± 0.16	0.60 ± 0.19	0.50 ± 0.20	0.63 ± 0.17
Chan-Vese	0.81 ± 0.11	0.84 ± 0.09	0.82 ± 0.08	0.81 ± 0.09	0.84 ± 0.08

Mathworks Central with default parameters. The Chan-Vese model is able to converge within 1000 iterations whereas ASM model has taken 10 iterations to converge. The Table 7.2 and Table 7.3 show the comparison optic cup segmentation performance across different methods. Due to inter-observer variability of more than 5% across different experts in Drishti-GS dataset, the optic cup segmentation performance has been compared with other models across different experts and mean of all annotations. The comparison shows that WPERCM has performed significantly better compared to its other two counterparts. This is also evident in case of SLO images shown in Table 7.3.

Some examples of visual comparison of these models is shown in Figure 7.5. The comparison shows that ASM is unstable while modeling the optic cup whereas Chan-Vese model is often misguided due to weak edge force around small optic cup area. Some examples of optic cup segmentation has been shown in Figure 7.4. RIM-ONE does not have optic cup annotations therefore the test results cannot be compared. However, we have performed optic cup segmentation in RIM-ONE dataset by constructing the WPERCM model based on Drishti-GS dataset which has lead to CDR calculation discussed in Chapter 9. The WPERCM can converge within 3 iterations on each image with time taken at each iteration is 2 seconds at Intel Core i7-2600 CPU with 16GB DDR3-1333 RAM.

Table 7.3: Comparison of results of the WPERCM with freeform and statistical shape models. The results show the accuracy in terms of dice coefficient

Datasets	Active Shape Model	Chan-Vese	**WPERCM**
Drishti-GS	0.63 ± 0.17	0.84 ± 0.08	0.87 ± 0.09
Optomaps	0.73 ± 0.1	0.75 ± 0.09	0.81 ± 0.12

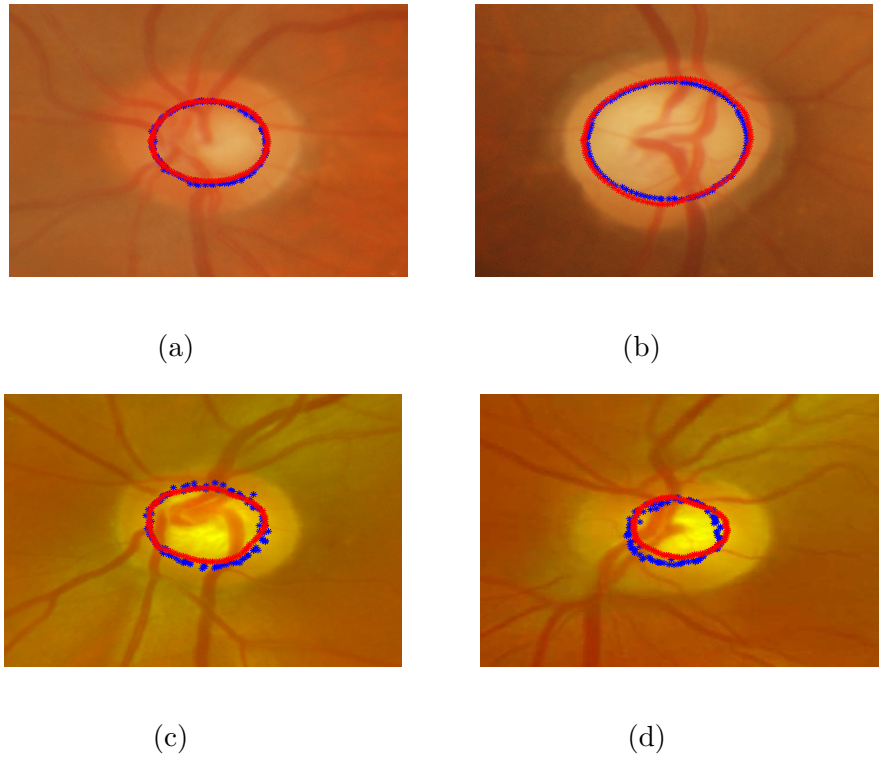

(a) (b)

(c) (d)

Figure 7.4: Examples of optic cup determination with red outline is the benchmark and blue outline is the automatic annotation. (a),(b) are the examples from Drishti-GS database and (c),(d) are the examples from Optomaps

7.5 Conclusion

In this chapter we proposed the new *Weighted Point Edge and Region Classification Model* (WPERCM) model for optic cup segmentation method which has been tested on different datasets. In contrast to PERCM the PEM determines the force field using the weighted feature maps whose weights are calculated by the RCM. The weighting of the feature maps is performed due to weak gradient between optic cup and rim area. The model has been tested for optic cup segmentation on Drishti-GS dataset and Optomaps and the segmentation accuracy compared to clinical annotations is 87% and 81% respectively. The proposed method outperformed its counterparts in terms of segmentation accuracy. This shows that if we weight the ONH area according to its membership of being the part of either optic cup or rim area, we can have significantly better performance in terms of optic cup modeling. The accurate segmentation of optic disc and optic cup is necessary for determination of CDR used for glaucoma diagnosis.

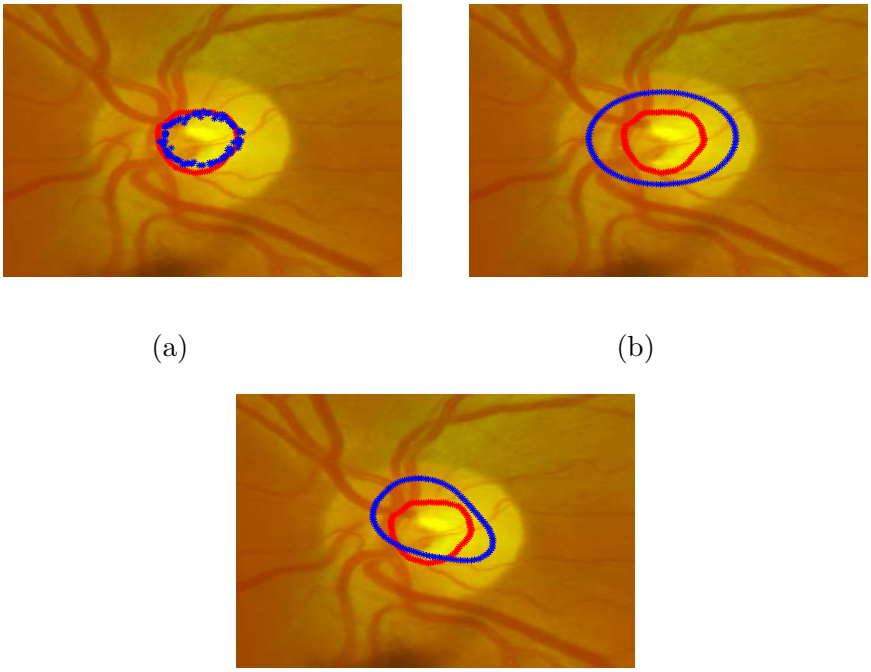

(a) (b)

(c)

Figure 7.5: Visual comparison of WPERCM with other models which were applied for optic cup segmentation. The images show the result of (a) WPERCM, (b) Chan-Vese model and (c) ASM. Red outline is the benchmark and blue outline is the automatic annotation

Chapter 8

Regional Image Features Model for Glaucoma Detection

8.1 Introduction

Glaucoma is normally associated with structural changes such as a slowly diminishing neuroretinal rim in the ONH [92] or the degeneration of the retinal layer in the region surrounding the ONH (also called the Peripapillary Atrophy (PPA)). This can be indicated by geometrical measures such as higher Cup to Disc Ratio (CDR) or the detection of rough texture around optic disc as shown in Figure. 8.1. It has been challenging task to classify between normal and glaucoma images since any of the geometrical or textural indication is itself not a guaranteed sign of glaucoma [65]. Also, the automatic calculation of geometrical indications require accurate segmentation of glaucoma related retinal structures such as optic disc and optic cup.

There are certain efforts which reflect the classification between normal and glaucoma images without any segmentation. These methods have been discussed in Section 3.3. These methods determine global features of the retinal image which can be used to classify between normal and glaucoma images. However, their accuracy and robustness is still questionable since they have been applied on a limited set of images. Our hypothesis is that the classification between normal and glaucoma images can be improved if the image-based features are calculated for different regions of the ONH centred image.

In this chapter, we will present our *Regional Image Features Model* (RIFM) for

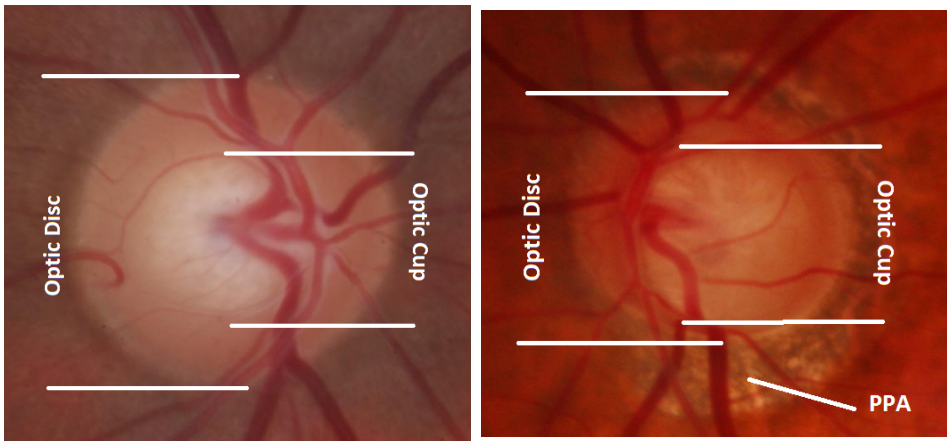

(a) Normal (b) glaucoma

Figure 8.1: Comparison of the ONH area of the (a) normal and (b) glaucomatous image. The difference is in terms of higher CDR and PPA indication

classification between normal and glaucoma images. This method is in contrast to previous methods in which the image features were calculated for the whole image [16, 24, 39]. In our proposed method, we divide the ONH cropped image into different regions i.e. the ONH area, inferior (I), superior(S), nasal(N) and temporal(T). These regions are usually observed by the clinicians for the diagnosis of glaucoma. The PPA has usually a larger area in T and I regions in case of glaucoma and the global image features such as wavelet energy, textural information etc. for these regions can be used to classify between normal and glaucoma images. Also, a large size of optic cup in the ONH area often has a higher mean grayscale value. The results of the model can also represent the presence of the PPA due to glaucoma. Since we have developed accurate method of optic disc segmentation (Chapter 6), this can be quite helpful in determining different regions of the ONH cropped image so as to calculate regional features for distinguishing between normal and glaucoma images.

8.2 Ground Truth

For experimental evaluation, we have one dataset for each of fundus and SLO images. Each of the dataset has been divided into normal and glaucomatous images.

Fundus Images: We have RIM-ONE dataset which has 118 normal and 40 glaucoma ONH cropped images. Each image has been automatically segmented out optic

disc by our proposed method in Chapter 6. For training and cross validation, we randomly selected 55 normal and 40 glaucoma images while other 63 normal images have been used for testing.

SLO images We have 51 normal images and 51 images obtained from diabetes patient with a suspect of glaucoma. Each image has been automatically ONH localized, ONH cropped and segmented around optic disc by our proposed PERCM model.

8.3 Regional Image Features

Regional Image Features (RIF) represent the global representation of the region. As stated earlier, we have divided the ONH centered image into five different regions i.e. the ONH area, inferior (I), superior(S), nasal(N) and temporal(T) as shown in Figure 8.2 for the right eye. For the left eye, N and T regions will be reversed. For generating these regions, we initially segmented out the ONH area (Chapter 6).

We then divide the image into four different quadrants i.e. I,S,N and T. These regions are adaptable for each image depending upon ONH segmentation. For elaborating the procedure, consider the Figure 8.2. The example is from the ONH centred image. The ONH boundary and its centroid can be shown in Figure 8.2(b). For the determination of quadrants, we connect the centroid to each of the corner of the image. As far as naming of the regions are concerned, I and S regions are fixed for each image. However, the N and T regions interchange their positions depending upon the left eye or the right eye. In order to determine whether the image is from the right eye or left eye, we draw a vertical line on the centroid as shown in Figure 8.2(c). Then we determine the area covered by the vasculature area within the ONH on either side. The vasculature area is maximum number of pixels within the ONH. In this case, the vaculature area is higher on the left so this image is considered as left eye image. Therefore, N and T regions will be on left side and right side respectively. For right eye image, these regions will interchange their positions. After determining the regions and the quadrants, we generate the mask excluding the ONH area as the ONH area is itself the fifth region of the image as shown in Figure 8.2(d). We have calculated the features of these five features as well as for the whole ONH centered image. The feature generation and selection procedure is discussed as follows.

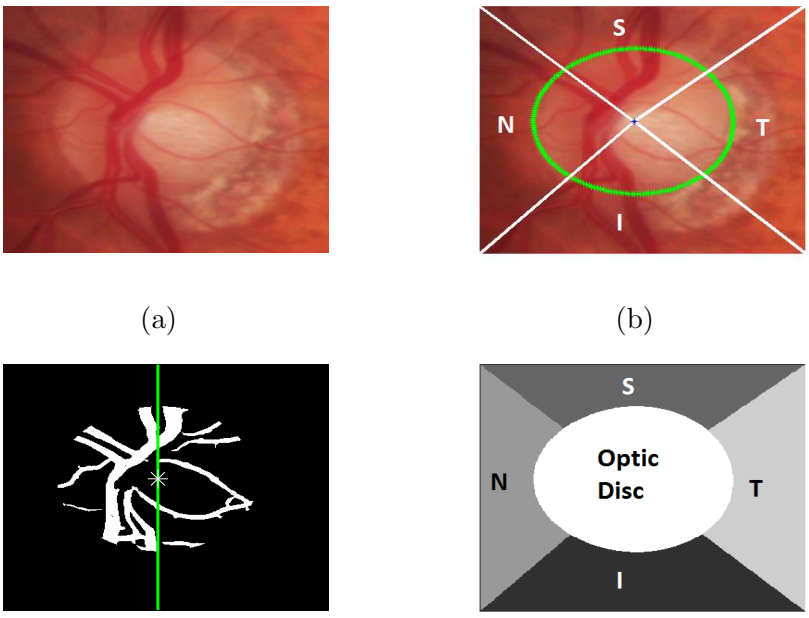

Figure 8.2: Different regions of the ONH centred image with (a) image of a left eye (b) image divided into different quadrants with the ONH boundary represented with green and centroid with blue colour, (c) vasculature area within the ONH with higher area on the left side (d) ONH centred image divided into different regions

8.3.1 Feature Generation and Selection

Particularly in the case of the RIF, the regions are larger than compared to superpixels generated by retinal area detection method (Section 5.2). Therefore, we have decided to calculate textural features with different offset values ranging from 1 to 10. Apart from features mentioned in Section 4.4.1, we have also calculated Discrete Wavelet Transform (DWT) features denoted by ψ [29]. The DWT has been quite effective in determining global features for classification between normal and glaucoma images [39] . The DWT features captures both spatial and frequency information of the image. DWT analyzes the image by decomposing it into a coarse approximation via low-pass filtering and into detail information via high-pass filtering. Such decomposition is performed recursively on low-pass approximation coefficients obtained at each level. The image is divided into four bands i.e. A(Top left (LL)), H (Top Right (LH)), V(Bottom Left (HL)) and D(Bottom Right (HH)). As an example, LH means rows and columns are filtered with low pass and high pass filter respectively. DWT decomposition is

calculated using different wavelet families such as db3, rbio3.3 etc [29]. For a particular region in the ONH centered image, we can calculate two types of features using these bands i.e. average value of the coefficients (ψ_{Avg}) and energy of the coefficients (ψ_{Energy}). As an example, the average value and average energy of D band are derived from the wavelet coefficients, as shown below:

$$\psi^{D}_{Avg} = \frac{1}{p\,q}\sum_{x=p}\sum_{y=q}|D_{band}(x,y)| \tag{8.1}$$

$$\psi^{D}_{Energy} = \frac{1}{p^2\,q^2}\sum_{x=p}\sum_{y=q}(D_{band}(x,y))^2 \tag{8.2}$$

where p and q represents width and height in pixels of the region respectively.

The feature matrix can be given as:

$$FM = \begin{bmatrix} A^{wav}_{RG} & A^{bif}_{RG} & A^{texoff}_{RG} & A^{texscale}_{RG} & A^{g}_{RG} \\ \\ B^{wav}_{RG} & B^{bif}_{RG} & B^{texoff}_{RG} & B^{texscale}_{RG} & B^{g}_{RG} \end{bmatrix} \tag{8.3}$$

where *RG* represents red and green channel respectively, *texoff* represents textural features with variable offset values, *texscale* represent textural features with variable scale, *bif* and *g* represent biologically inspired features and gradient features respectively. These features are calculated for different regions and for the whole ONH cropped image. Therefore they are assigned different columns in the feature matrix.

The RIF has been selected using the SFS approach. From the available set of features, the feature with the best classification performance (AUC) are selected. The performance of the feature set has been compared with global information of the image in terms of wavelet, texture, and gradient features. The global features of each feature group has been calculated for the whole image for comparing with the RIFs. As an example, in Table 8.2, 'Global Features' represent the global information in terms of all groups of features whereas 'Global Wavelet Features' represent the global information in terms of wavelet features only. In all of the global feature sets, the features most relevant to the classification are used.

The different models has been trained and tested on the fundus and the SLO images. The AUC of the selected feature set for both fundus images and the SLO images and feature selection procedure are shown in Figure 8.3. For generating the ROCs in

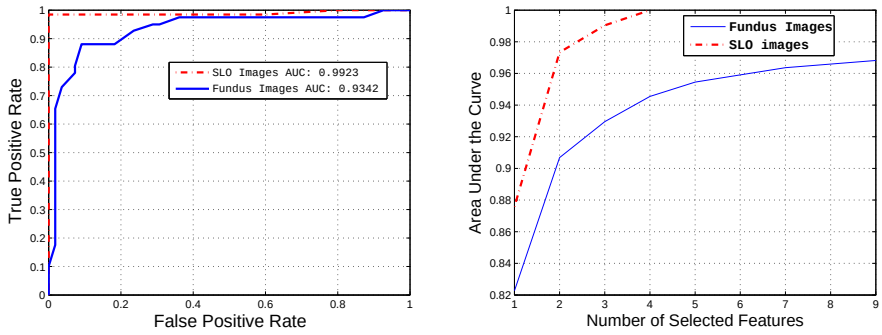

(a) (b)

Figure 8.3: Results of regional image feature selection procedures for classification between normal and glaucomatous images with (a) ROC curves of both fundus and the SLO images for selected features using the SFS and (b) feature selection process using the SFS

Figure 8.4, the cross-validation has been performed using 5-fold cross validation. Table 8.1 represents variables along x-axis of Figure 8.3(b). The explanation of variables related to Haralick features are presented in Table 4.4. As an example, $\psi(db3)^{OD_A}_{GEnergy}$ means wavelet of family db3; OD and A in the superscript represent optic disc region and A band of wavelet; G and $Energy$ represent the Green channel and Energy of wavelet coefficients respectively. Also in subscript of $acorr^{OD}_{R1}$, 1 represent the offset value and in $IM^{I}_{2G}(8)$, 8 in the bracket represents the scale. The features shown in Table 8.1 support our hypothesis that there is an obvious difference between normal and glaucomatous images in terms of texture and energy of I and T regions as well as optic disc.

Table 8.1: Feature sets obtained using the SFS approach for classification between normal and glaucomatous images

Datasets	Feature Symbols
fundus Images	μ^{I}_{sumR1}, $H^{S}_{G}(1)$, $acorr^{OD}_{R1}$, $\psi(db3)^{OD_A}_{GEnergy}$, con^{S}_{R2}, $diss^{N}_{R1}$, $\mathcal{N}^{N}_{xG}(2)$, IDN^{N}_{R4}, $IM^{I}_{2G}(8)$
SLO Images	$\sigma^{OD}_{sumG}(16)$, $C^{N}_{shadeR}(1)$, $C^{T}_{promR}(1)$, $\psi(db3)^{I_H}_{RAvg}$

8.4 Experimental Evaluation

We have constructed the classifier of *Regional Image Feature Model* (RIFM) using ANN. For hidden layer, we have selected 10 neurons. The performance of the classifier

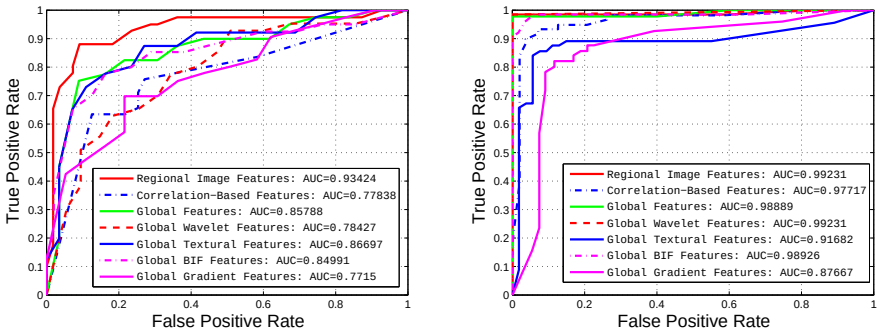

(a) (b)

Figure 8.4: Comparison of ROC curves of different feature sets in fundus and the SLO images

on the RIF has been compared with different classifiers such as Support Vector Machines (SVM) and k Nearest Neighbours (kNN). We used both linear as well as kernel based SVM [61]. For kernel based SVM, we used Radial-based Function with default parameter of $(numberoffeatures)^{-1}$. For kNN we have selected k=maximum number of features in the feature set.

The comparison of the different feature sets has been shown in Table 8.2. According to the Table, the RIFs outperformed significantly especially in case of fundus images. It is also evident by comparison of the *Receiver Operating Characteristics* (ROC) curves in Figure 8.4. This shows that classification based of features calculated for different regions has better classification performance compared to the feature sets providing the global information for the whole image.

As far as feature selection is concerned, we have performed the SFS on both RIFs and global features. From the superscript of feature symbols shown Table 8.1, it is evident that neither of the features representing the global information have been selected in our final feature set. Also the comparison of 'Global Features' with other global feature sets calculated for individual feature group make it evident that combination of features of different feature groups can have better classification performance as compared to features calculated for individual group. By observing the Tables 8.1 and 8.2, we deduce that textural features are more dominant compared to other groups due to their higher sensitivity. However, wavelet features can perform better in terms of specificity. Therefore the combination of selected features of all groups can have higher classification power which has been further improved by calculating features

for different regions i.e. the RIFs.

Table 8.3 which shows the performance of the ANN compared to other classifier models. According to the Table, the linear SVM is the only classifier which is able to perform closely to the ANN. However, the ANN performed significantly better as compared to other classifiers. As far as Optomaps are concerned, the retinal changes associated with diabetes might be more prominent which possibly can be the result of higher classification performance with little difference across different feature sets and across different classifiers.

Table 8.2: Comparison of the results of regional image feature set with other feature sets

Feature Set	RIMONE			Optomaps		
	Sensitivity	Specificity	Overall Accuracy	Sensitivity	Specificity	Overall Accuracy
Regional Image Features	90.00%	93.22%	92.4%	98.03%	98.03%	98.03%
Global Features	65.00%	88.13%	82.27%	98.03%	98.03%	98.03%
Global Wavelet Features	65.00%	81.35%	77.21%	96.07%	96.07%	96.07%
Global Textural Features	77.5%	70.33%	72.15%	96.07%	90.19%	93.13%
Global Biologically Inspired Features	65.00%	76.27%	73.41%	94.11%	98.03%	96.07%
Global Gradient Features	62.50%	75.42%	72.15%	92.15%	84.31%	88.23%

Table 8.3: Comparison of the results of different classifiers on the RIF set

Classifier	RIMONE			Optomaps		
	Sensitivity	Specificity	Overall Accuracy	Sensitivity	Specificity	Overall Accuracy
ANN	90.00%	93.22%	92.4%	98.03%	96.07%	97.05%
Linear SVM	90.00%	83.89%	85.44%	94.11%	98.03%	96.07%
Kernel SVM	85.00%	77.11%	79.11%	94.11%	98.03%	96.07%
kNN	75.00%	81.35%	79.74	88.23%	98.03%	93.13%

8.5 Conclusion

In this chapter, we have proposed the *Regional Image Features Model* (RIFM) for classification between normal and glaucomatous images. Previously, these features have been calculated for the whole ONH centered image. In the proposed approach, we have divided the image into different regions for feature calculation. These regions are usually analyzed by the clinicians for the diagnosis of glaucoma. The selected features are then used for classification between normal and glaucoma images. The classification accuracy on RIM-ONE and Optomaps is 92.4% and 97.05% respectively. The result

suggests significantly better performance compared to the features calculated for an ONH cropped image. Using the classification procedure, we determined classification weights which indicate the degree of membership to either normal or glaucoma images. These classification weights has been accommodated alongwith the geometrical indications calculated using segmentation methods discussed in chapter 5,6 and 7.

Chapter 9

Diagnosis of Glaucoma

9.1 Introduction

In this chapter, we will perform the classification between normal and glaucoma images on the basis of classification results of the RIFM and the clinical indications of glaucoma. Clinical indications for the glaucoma diagnosis include CDR, vasculature shift and ISNT rule. On the other hand, the RIFM classification results include the classification weights which indicate the degree of membership to either normal or glaucoma. In the following sections, we will describe the automatic calculation of the clinical indications using segmentation results obtained in chapter 6 and 7. Then we will describe plain the feature selection procedure, training, testing and evaluation procedure for classification between normal and glaucoma images.

9.2 Automatic Determination of Clinical Indications of Glaucoma

9.2.1 Cup to Disc Ratio

Cup to Disc Ratio (CDR) is one of the most common measures which is usually assessed by the clinicians to diagnose glaucoma (Section 2.5.1). According to clinicians [65], the CDR can be calculated by taking the ratio of diameter of the cup and the disc in either vertical or horizontal direction. The reason of including the CDR is that cup becomes large with respect to optic disc. This can be shown Figure 9.1 in which the size of optic

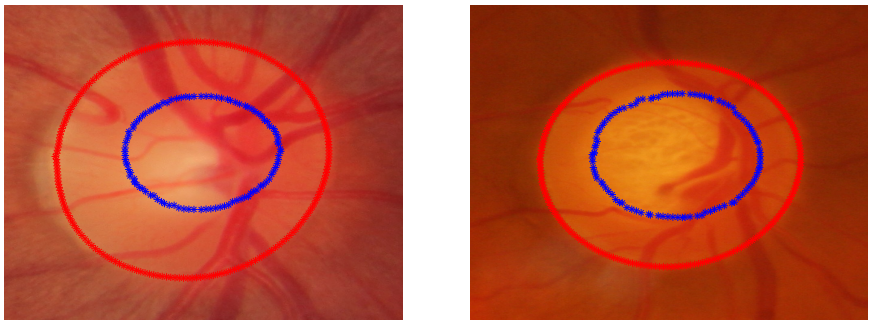

(a) (b)

Figure 9.1: Comparison of the cup size with respect to the disc in (a) normal image and (b) glaucoma image. Both optic disc and optic cup boundaries have been automatically obtained by our proposed methods in Chapter 6 and 7.

cup with respect to optic disc has been compared in normal and glaucoma images. We calculated both CDRs on automatically identified boundaries of optic disc and cup as discussed in Chapter 6 and 7. It can be seen from the figure that with respect to optic disc, the optic cup has larger size in case of glaucoma compared to normal image. Also based on the automatic annotations obtained for optic disc and optic cup, we calculated the vertical as well as horizontal CDR of normal and glaucomatous images in the datasets.

The mean and standard deviation of horizontal and vertical CDR values of both normal and glaucoma images tested on RIM-ONE and Optomaps has been shown in Table 9.1. The mean CDR values between normal and glaucoma images have significant difference especially in the case of RIM-ONE dataset. However by observing the Figure 9.2, we can deduce that any of the vertical or horizontal CDR value is not the only sign of glaucoma since some of the normal images can have high CDR values and vice versa. In case of Optomaps (SLO images), there is not significant difference between normal and diseased images. This might be due to the fact that diseased images have been taken from diabetes patient with suspect of glaucoma. Nevertheless, vertical CDR is one of the authentic geometrical indication associated to glaucoma as observed in Table 9.1 and Figure 9.2.

Table 9.1: Mean(μ) and standard deviation(σ) of horizontal and vertical CDR of both normal and glaucoma images

Images	CDR vertical $\mu \pm \sigma$	CDR horizontal $\mu \pm \sigma$
RIM-ONE		
Normal	0.45 ± 0.09	0.51 ± 0.09
Glaucoma	0.63 ± 0.10	0.60 ± 0.07
Optomaps		
Normal	0.50 ± 0.05	0.52 ± 0.06
Glaucoma	0.55 ± 0.10	0.54 ± 0.10

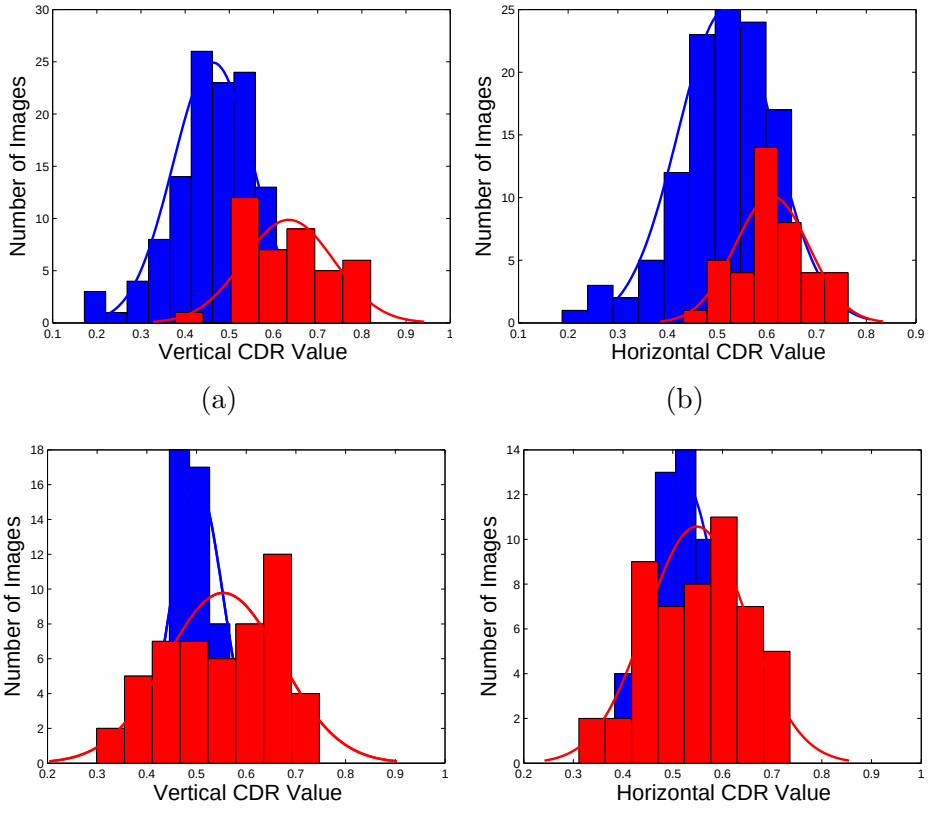

Figure 9.2: Comparison of CDR histogram plots between normal and glaucoma images in RIM-ONE and Optomaps (SLO images) with blue representing normal and red representing glaucoma. (a) Vertical CDR and (b) horizontal CDR comparison on RIM-ONE and (c) vertical CDR and (d) horizontal CDR comparison on Optomaps.

9.2.2 Vasculature Shift

In glaucoma images, the vasculature area with the ONH has a higher vessel density compared to normal images in the nasal(N) area [48]. This phenomenon is known as the vasculature shift. The measurement can be used to classify between normal and glaucoma images. In order to describe the vasculature shift, consider the examples of normal and glaucoma shown in Figure 9.3. Just to demonstrate that nasal(N) and temporal(T) region are swapped for left and right eyes, we have shown the normal image from the right eye and glaucoma image from the left eye. The images are divided into four quadrants i.e. I,S, N and T (see Section 2.8). We then calculate the centroid of the vasculature bundle in I,S and N regions of the ONH area (shown with green asterisks in Figure 9.3). Then the distance from each centroid point is calculated from the border point of optic cup in the T region which is the farthest from the ONH center. The distances are then normalized by dividing them with horizontal diameter of the optic disc which is shown as:

$$D_{vascshift} = \sum_{n=1}^{3} \frac{dcc_n}{ODdia_{hor}} \tag{9.1}$$

where dcc is the distance from centroid to the cup boundary and $ODdia_{hor}$ is horizontal diameter of the optic disc. By comparing both examples, it is illustrated that $D_{vascshift}$ has higher value in case of glaucoma. The mean(μ) and standard deviation(σ) of $D_{vascshift}$ in normal and glaucoma images is shown in Table 9.2.

Like vertical CDR, vasculature shift is another authentic geometrical indication associated with glaucoma but it can not be the only glaucomatous clinical indication since histogram curves of normal and glaucoma shown in Figure 9.4 are not placed clearly further apart.

9.2.3 Neuroretinal Rim Loss (ISNT Rule) Calculation

The ISNT rule states that ONH rim width in I,S,N and T regions usually would be the greatest in I followed by S,N and T. In short, the rim width of the normal images follows (I>S>N>T) rule known as ISNT rule (see Section 2.8). The glaucoma images usually disobeys that rule.

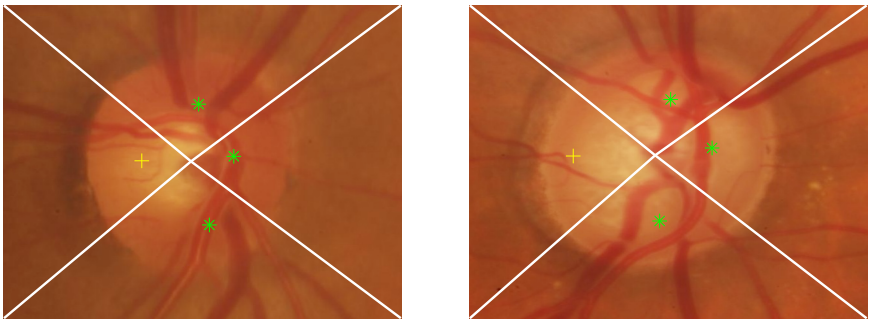

(a)

(b)

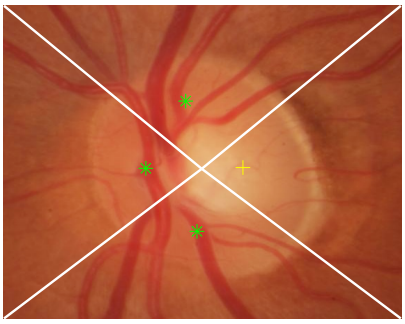

(c)

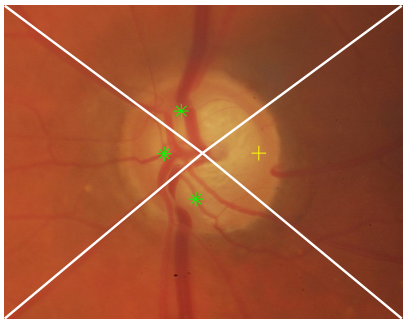

(d)

Figure 9.3: Comparison of the vasculature shift in (a) right eye normal image and (b) right eye glaucoma image (c) left eye normal image and (b) left eye glaucoma image. In glaucoma images, the vasculature bundle is shifted towards the N region. Green asterisks represent the centroid of the vasculatrue bundle in I, S and N regions whereas yellow plus sign represent optic cup border point in T region farthest from the ONH center. Noting that N and T regions are at right and left side respectively in case of right eye image. These regions swap their places in case of left eye.

Table 9.2: Mean(μ) and standard deviation(σ) of vasculature shift of both normal and glaucoma images

Images	Vasculature Shift $\mu \pm \sigma$
RIM-ONE	
Normal	0.42 ± 0.05
Glaucoma	0.49 ± 0.04
Optomaps	
Normal	0.44 ± 0.05
Glaucoma	0.51 ± 0.07

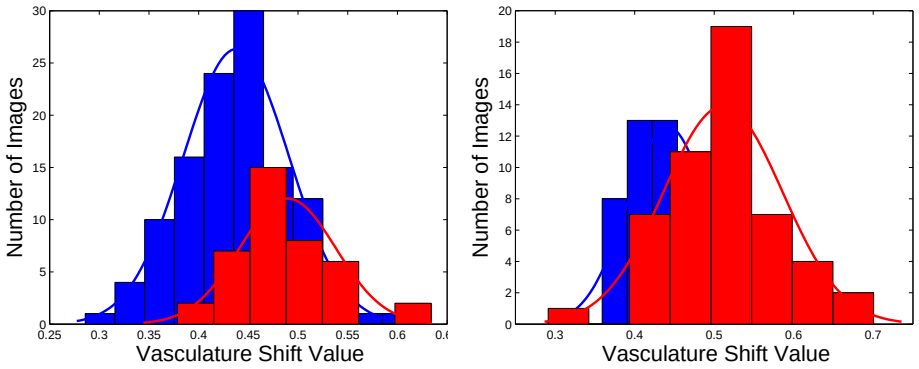

(a) (b)

Figure 9.4: Comparison of vasculature shift histogram plots between normal and glaucoma images in RIM-ONE and Optomaps (SLO images) with blue representing normal and red representing glaucoma. (a) comparison on RIM-ONE and (b) comparison on Optomaps.

9.3 Ground Truth

For experimental evaluation, we have one dataset for each of fundus and SLO images. Each of the dataset has been divided into normal and glaucomatous images.

Fundus Images: We have RIM-ONE dataset which has 118 normal and 40 glaucoma ONH cropped images. For training and cross validation, we have randomly selected 55 normal and 40 glaucoma images while other 63 normal images have been used for testing.

SLO images We have 51 normal images and 51 images obtained from diabetes patient with a suspect of glaucoma.

9.4 Experimental Evaluation

Each of the images have been passed through the ONH localization, optic disc and cup segmentation, ONH area vasculature segmentation as discussed in previous chapters. We have performed a 5-fold cross validation and performed classification using neural networks. The five features obtained in the previous section i.e. (Vertical CDR, Horizontal CDR, Vasculature Shift, ISNT rule and RIF classification weights) have been accommodated to form a feature matrix and then applied the SFS approach for feature selection. The SFS approach selected three features for RIM-ONE and Optomaps i.e. for RIM-ONE = [RIF classification weights, Vertical CDR, Vasculature

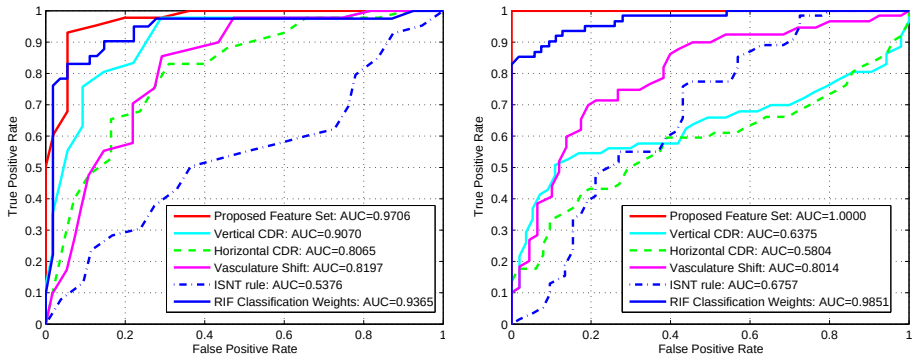

(a) (b)

Figure 9.5: Comparison of proposed feature set with different clinical indications of glaucoma and Regional Image Features (RIF) classification results. The comparison has been performed on (a) RIM-ONE and (b) Optomaps

Shift] and for Optomaps = [RIF classification weights, Vasculature Shift, ISNT rule]. We have then calculated the sensitivity, specificity and overall accuracy (Section 4.4.3) on the feature sets proposed for both datasets and compared the performance with each individual feature as shown in Table 9.3.

The result comparison shows that vertical CDR, vasculature shift and RIF classification can play a significant role in classification between normal and glaucoma images in case of RIM-ONE dataset. As far as SLO images are concerned, we have the diseased images obtained from diabetes patient with the suspect of glaucoma. The higher accuracy in case of SLO images might be due to the reason of diabetes symptoms being classified as glaucoma. This needs further study in terms of clinical annotations.

9.5 Conclusion

In this chapter, we discussed the classification of normal and glaucoma images based on Regional Image Features and clinical indications. The proposed feature set has surpassed all methods on RIM-ONE and Optomaps which used only CDR or vasculature shift for classification between normal and glaucoma images. The classification accuracy achieved on RIM-ONE and Optomaps is 94.93% and 98.03% respectively. The higher accuracy in case of SLO images might be due to the reason of diabetes symptoms being classified as glaucoma. This needs further study in terms of clinical

Table 9.3: Classification power of the features used for glaucoma diagnosis

Features	Sensitivity	Specificity	Overall Accuracy
RIM-ONE Dataset			
RIF Classification Weights	90.00%	93.22%	92.4%
Vertical CDR	80.00%	81.35%	81.01%
Vasculature Shift	75%	86.44%	83.54%
Horizontal CDR	60.00%	83.89%	77.84%
ISNT rule	10.00%	43.22%	34.17%
Proposed Feature Set	92.5%	95.76%	94.93%
Optomaps			
RIF Classification Weights	98.03%	96.07%	97.05%
Vertical CDR	43.13%	92.15%	67.64%
Vasculature Shift	70.58%	78.43%	74.51%
Horizontal CDR	29.41%	88.23%	58.82%
ISNT rule	90.19%	37.25%	63.72%
Proposed Feature Set	98.03%	98.03%	98.03%

annotations.

Chapter 10

Discussion and Conclusion

Glaucoma is a group of eye diseases that have common traits such as, high eye pressure, damage to the Optic Nerve Head (ONH) and gradual vision loss. It affects peripheral vision and eventually leads to blindness if left untreated. The current common methods of pre-diagnosis of glaucoma include measurement of Intra-Ocular Pressure (IOP) using Tonometer, Pachymetry, Gonioscopy; which are performed manually by the clinicians. These tests are usually followed by the ONH appearance examination for the confirmed diagnosis of glaucoma. The diagnoses require regular monitoring, which is costly and time consuming. The accuracy and reliability of diagnosis is limited by the domain knowledge of different ophthalmologists. Therefore automatic diagnosis of symptoms associated with glaucoma attracts a lot of attention. In this thesis we have proposed a novel Glaucoma Detection Framework (GDF) which involves automatic determination of retinal image patterns associated with glaucoma and classification between normal and glaucoma images on the basis of these symptoms.

In this work, several major contributions have been made towards the development of the automatic GDF consisting of the stages of preprocessing, optic disc and cup segmentations and regional image feature methods for classification between glaucoma and normal images. The specific contributions of this project include:

1. Preprocessing Stage

    - Development of a superpixel-based retinal area detector to determine the true retinal area from the SLO images while preserving computational efficiency and avoiding over-segmentation of artefacts.

- Determination of a new weighted feature map approach which can enhance the ONH region for more accurate localization.
- Development of the ONH cropped image based vasculature classification model to segment out vasculature while avoiding misidentification of the ONH boundary being a part of vasculature structure.

2. Development of the models for optic disc and optic cup segmentation including:

   - *Region Classification Model* (RCM) which initially determines the optic disc/cup region using selected feature maps.
   - *Point Edge Model* (PEM) which updates the contour using force fields of the selected feature maps.
   - *Weight Point Edge Model* (WPEM) which determines the force field using the weighted feature maps calculated by the RCM for optic cup in order to enhance the optic cup region compared to rim area in the ONH.

   The combination of RCM and PEM is called *Point Edge and Region Classification Model* (PERCM) for optic disc segmentation whereas the combination of WPEM and RCM is called *Weighted Point Edge and Region Classification Model* (WPERCM) for optic cup segmentation.

3. Development of *Regional Image Features Model* (RIFM) for classification between normal and glaucoma images using image-based information from different regions of the ONH image. These regions are clinically observed for analyzing glaucoma related indications especially the PPA.

4. Accommodation of geometrical indication calculated by optic disc, optic cup and vasculature segmentation (e.g. CDR, vasculature shift) with results of the RIFM to perform classification between normal and glaucoma images.

The proposed methodology starts with preprocessing steps needed for retinal image analysis for diagnosing glaucoma. The pre-processing steps include retinal area detection, ONH localization and vasculature segmentation. Distinguishing true retinal area from artefacts in SLO images is a challenging task, which is also the first important step towards computer-aided disease diagnosis. In this work, we have proposed

a novel framework for automatic detection of true retinal area in SLO images. We have used superpixels to represent different irregular regions in a compact way and reduce the computing cost. Feature selection enables the most significant features to be selected and thus reduces computing cost too. A classifier has been built based on selected features to extract out the retina area. It has been compared with other two classifiers and was compatible while saving the computational time. The experimental evaluation result shows that our proposed framework can achieve an accuracy of 92% in segmentation of the true retinal area from an SLO image. Apart from retinal area detection, we proposed weighted feature map based ONH localization method so as to improve the ONH localization accuracy and robustness. The average ONH localization accuracy on fundus images and SLO images is 100% and 98% respectively. The vasculature segmentation is a key step to determine the vasculature shift which is one of the geometrical indication associated with glaucoma. We proposed the classification model for segmenting out vasculature area from the ONH image. The average segmentation accuracy achieved on fundus images and SLO images is 90.77% and 90.21%.

The GDF is proceeded with segmentation of glaucoma associated retinal structures such as optic disc and optic cup and determination of geometrical measurements used for diagnosing glaucoma such as Cup to Disc Ratio (CDR). We have proposed a novel *Point Edge and Region Classification Model* for the determination of optic disc boundary. The PERCM initially determines the optic disc region on the basis of *Region Classification Model* (RCM) and then updates the optic disc contour using force field based *Point Edge Model* (PEM). The model has been tested against different databases of SLO and fundus images. The average segmentation accuracy achieved by the model on Drishti-GS, RIM-ONE and Optomaps is 97%, 94% and 90% respectively.

For optic cup segmentation, we proposed the new *Weighted Point Edge and Region Classification Model* (WPERCM) model for optic cup segmentation method which has been tested on different datasets. In contrast to PERCM the PEM determines the force field using the weighted feature maps whose weights are calculated by the RCM. The weighting of the feature maps is performed due to weak gradient between optic cup and rim area. The model has been tested for optic cup segmentation on Drishti-GS dataset and Optomaps and the segmentation accuracy compared to clinical annotations is 87% and 81% respectively. This shows that if we weight the ONH area according to its

membership of being the part of either optic cup or rim area, we can have significantly better performance in terms of optic cup modeling. However, the method can be further improved if the vessel kinks at the border of the optic cup are put into account. Moreover, stereo imaging based training can be quite helpful in improvement in optic cup segmentation performance.

The GDF is further proceeded by *Regional Image Features Model* (RIFM) for classification between normal and glaucomatous images. In the proposed approach, we divided the image into different quadrants and the ONH (segmented out by the PERCM discussed in chapter 6) for feature calculation. These regions are usually analyzed by the clinicians for the diagnosis of glaucoma. The selected features are then used for classification between normal and glaucoma images. The classification accuracy on RIM-ONE and Optomaps is 92.4% and 97.05% respectively. The result suggests significantly better performance compared to those whose textural and wavelet features were calculated for a whole ONH image.

Finally, we have developed a classification model for the GDF which can classify between normal and glaucoma images on the basis of geometrical measures and RIFM results. The geometrical measures, such as CDR, I,S,N,T rule, vasculature shift etc. related to glaucoma analysis have been calculated using the segmentation methods discussed in chapter 5,6 and 7. The regional image features classification results have been obtained from chapter 8. For both RIM-ONE and Optomaps, different feature set are proposed. RIM-ONE dataset has normal images and images diagnosed with glaucoma whereas Optomaps has normal images and the images of diabetes with suspected glaucoma. The proposed feature sets of both RIM-ONE and Optomaps has surpassed all methods on RIM-ONE and Optomaps which used only CDR or vasculature shift for classification between normal and glaucoma images. The classification accuracy between normal and glaucoma images is 94.93% and 98.03% respectively. One of the reason of high accuracy of glaucoma classification in case of SLO images might be due to involvement of diabetes related features. This results can be more authenticated if the data is collected from the subjects of similar group of people.

Our GDF software is already under trial for Optos SLO devices to automatically identify patterns associated with glaucoma. This will reduce operational costs for both the industry and healthcare services and increase the medical industry revenue,

and thus the economic growth in UK and across the world. Besides, the software is equally applicable and can be instrumented on fundus cameras as well. Especially in the UK, National Health Services (NHS) practices are overwhelmed with the number of patients that must undergo screening as part of the National Screening Programme. The software has the potential to reduce time which clinicians need to look at the images which can expect more patients to be screened and more consistent diagnoses can be given in a time efficient manner; thereby enable higher throughput in practices.

Future work proposes the multiclass classification among normal and different stages of glaucoma. This can be possible using the large training set of each of the normal and different glaucoma stages. Also the optic cup segmentation accuracy can be improved further by determining the model using a pair of stereo retinal images. The use of stereo retinal images can be used to interpolate the ONH area in 3D.

Appendix A

Publications

1. M.S. Haleem, L. Han, J. Hemert, B. Li and A. Fleming. Retinal Area Detector from Scanning Laser Ophthalmoscope (SLO) Images for Diagnosing Retinal Diseases. *IEEE Journal of Biomedical and Heath Informatics*, (to appear), 2014.

2. M.S. Haleem, L. Han, J. Hemert and B. Li. Automatic Extraction of Retinal Features from Colour Retinal Images for Glaucoma Diagnosis: A review. *Computerized Medical Imaging and Graphics*, vol. 37, no. 7, pp. 581 596, 2013.

3. M.S. Haleem, L. Han, J. Hemert, B. Li and A. Fleming. Glaucoma Classification using Regional Wavelet Features of the ONH and its Surroundings. *37th Annual Conference of the IEEE Engineering in Medicine and Biological Society (EMBS)*, (to appear), 2015.

4. L.Han, M.S. Haleem and M. Taylor. A Novel Computer Vision-based Approach to Automatic Detection and Severity Assessment of Crop Diseases. *IEEE Technically Co-Sponsored Science And Information Conference*, (to appear), 2015.

5. M.S. Haleem, L. Han, J. Hemert, B. Li and A. Fleming. Superpixel based Retinal Area Detection in SLO Images. *Lecture Notes in Computer Science*, 8671: pp. 254 261. 2014.

6. M.S. Haleem, L. Han, B. Li, A. Nisbet, J. Hemert and M. Verhoek. Automatic Extraction of the Optic Disc Boundary for Detecting Retinal Diseases. *Computer Graphics and Imaging-IASTED*, 2013, pp. 40-47.

7. M.S. Haleem, M.A. Haider and I.S. Yetik. A Task-Based Approach to Parametric Imaging with Dynamic Contrast-Enhanced MRI. *International Symposium of Biomedical Imaging-IEEE*, 2011, pp. 746-749.

8. M. S. Haleem. Voice Controlled Automation System. *International Multitopic Conference-IEEE*, 2008, pp. 508-512.

9. Regional Image Features Model for Classification between Normal and Glaucoma Images in Fundus and SLO Images. *in preparation.*

10. Point Edge and Region Classification Model for segmenting Optic Disc and Optic Cup on fundus and SLO images. *in preparation.*

Appendix B

Academic Activities

This project is sponsored by Engineering and Physical Sciences Research Council-Dorothy Hodgkin Postgraduate Award (EPSRC-DHPA). For this project I have applied for UK ICT pioneer which is an exciting competition for doctoral students to communicate and demonstrate the excellence and exploitation potential of their research topic. Till date, I have cleared the first stage of the competition which is based on present your research within 500 words. Now I am preparing for the second stage which is based on 3 minute video preparation of the research.

I have been the student member of IEEE Engineering in Medicine and Biology Society and IEEE Computing Society.

I have presented my research work in various conferences such as:

- IEEE conference on Engineering in Medicine and Biological Society (EMBC). Milan, Italy, August 2015.
- International Conference of Computer Vision and Graphics (ICCVG). Warsaw, Poland, September 2014.
- British Machine Vision Association (BMVA) Summer School
- IASTED conference of Computer Graphics and Imaging (CGIM). Innsbruck, Austria, February 2013.
- IEEE International Symposium of Biomedical Imaging (ISBI). Chicago, USA, April 2011.

- IEEE International Multi Topic Conference (IEEE-INMIC). Karachi, Pakistan, April 2008.

I have been the reviewer of several journals including

- IEEE Transactions of Biomedical Engineering.
- Elsevier Journal of Computer in Biology and Medicine.
- Journal of Optometry.
- IEEE Conference of Systems, Man, and Cybernetics (SMC).
- International Journal of Computer Systems Science and Engineering.
- Biomedical Engineering/Biomedizinische Technik.

I have attended various seminars and summer schools including

- British Machine Vision Association (BMVA) Summer School, 2013
- EPSRC ICT Student Futures Workshop, 2013.
- New to Teaching (NewT) at Manchester Metropolitan University.

Bibliography

[1] Amarilloicare clear vision. [Online]. Available: http://www.amarilloicare.com

[2] The eye clinic surgicenter. [Online]. Available: http://www.theeyesurgicenter.com/canaloplasty/

[3] Glaucoma research foundation. [Online]. Available: http://www.glaucoma.org/glaucoma/diagnostic-tests.php

[4] The most common causes of blindness. [Online]. Available: http://www.livestrong.com/article/92727-common-causes-blindness

[5] National eye institute. [Online]. Available: https://www.nei.nih.gov/

[6] National health services, UK. [Online]. Available: http://www.nhscareers.nhs.uk/features/2011/june/

[7] Ophthalmic photographers society. [Online]. Available: http://www.opsweb.org/?page=fundusimaging

[8] Optos. [Online]. Available: www.optos.com

[9] "Glaucoma diagnosis: The role of optic nerve examination," Rotterdam Eye Hospital, Tech. Rep., 2007.

[10] (2008) (méthodes d'evaluation de systèmes de segmentation et d'indexation dédiées à l'ophtalmologie rétinienne). [Online]. Available: http://messidor.crihan.fr/description-en.php

[11] "Diagnosing and treating glaucoma and raised eye pressure," National Institute of Health and Clinical Excellence (NICE), Tech. Rep., 2009.

[12] "Diagnosis and management of chronic open angle glaucoma and ocular hypertension," National Collaborating Centre for Acute Care, Tech. Rep., 2009.

[13] (2011, May) Types of glaucoma. [Online]. Available: http://www.glaucoma.org/glaucoma/types-of-glaucoma.php

[14] M. Abràmoff, W. Alward, E. Greenlee, L. Shuba, C. Kim, J. Fingert, and Y. Kwon, "Automated segmentation of the optic disc from stereo color photographs using physiologically plausible features," *Investigative Ophthalmology and Visual Science*, vol. 48, no. 4, pp. 1665–1673, 2007.

[15] R. Achanta, A. Shaji, K. Smith, A. Lucchi, P. Fua, and S. Susstrunk, "SLIC superpixels compared to state of the art superpixel methods," *IEEE Transactions on Pattern Analysis and Machine Intelligence*, vol. 34, no. 11, pp. 2274–2282, 2012.

[16] R. Acharya, S. Dua, X. Du, V. Sree, and C. K. Chua, "Automated diagnosis of glaucoma using texture and higher order spectra features," *IEEE Transactions on Information Technology in Biomedicine*, vol. 15, no. 3, pp. 449–455, 2011.

[17] E. H. Adelson, C. H. Anderson, J. R. Bergen, P. J. Burt, and J. M. Ogden, "Pyramid methods in image processing," *RCA Eng*, vol. 29, no. 6, pp. 33–41, 1984.

[18] A. J. Alberg, J. W. Park, B. W. Hager, M. V. Brock, and M. Diener-West, "The use of overall accuracy to evaluate the validity of screening or diagnostic tests," *Journal of General Internal Medicine*, vol. 19, no. 1, pp. 460–465, 2004.

[19] A. Aquino, M. Gegúndez-Arias, and D. Marín, "Detecting the optic disc boundary in digital fundus images using morphological, edge detection, and feature extraction techniques," *IEEE Transactions on Medical Imaging*, vol. 29, no. 11, pp. 1860–1869, 2010.

[20] T. R. G. Babu and S. Shenbagadevi, "Automatic detection of glaucoma using fundus image," *European Journal of Scientific Research*, vol. 59, no. 1, pp. 22–32, 2011.

[21] T. Barnett. (2000, September) Goldmann applanation tonometry. [Online]. Available: webeye.ophth.uiowa.edu

[22] K. Bartz-Schmidt, T. G., and J.-C. C.P., "Quantitative morphologic and functional evaluation of the optic nerve head in chronic open-angle glaucoma." *Survey of Ophthalmology*, vol. 44, pp. S41–53, 1999.

[23] R. Bock, J. Meier, G. Michelson, L. Nyúl, and J. Hornegger, "Classifying glaucoma with image-based features from fundus photographs," in *Proceedings of the 29th DAGM (German Conference on Pattern Recognition) conference on Pattern recognition*, vol. 4713, 2007, pp. 355–364.

[24] R. Bock, J. Meier, L. Nyúl, J. Hornegger, and G. Michelson, "Glaucoma risk index:automated glaucoma detection from color fundus images," *Medical Image Analysis*, vol. 14, no. 3, pp. 471–481, 2010.

[25] L. Breiman, "Random forests," University of California, Berkeley, Tech. Rep., 2001.

[26] J. Caprioli, "Clinical evaluation of the optic nerve in glaucoma," *Transactions of American Ophthalmological Society*, vol. 92, p. 589641, 1994.

[27] E. Carmona, M. Rincón, J. García-Feijoo, and J. Martínez-de-la Casa, "Identification of the optic nerve head with genetic algorithms," *Artificial Intelligence in Medicine*, vol. 43, no. 3, pp. 243–259, 2008.

[28] T. F. Chan and L. A. Vese, "Active contours without edges," *IEEE Transactions on Image Processing*, vol. 10, no. 2, pp. 266–277, 2001.

[29] W.-l. Chao, "Gabor wavelet transform and its application," Tech. Rep., 2010.

[30] S. Chatterjee, N. Katz, M. Nelson, and M. Goldbaum, "Detection of blood vessels in retinal images using two-dimensional matched filters." *IEEE Transactions of Medical Imaging*, vol. 8, no. 3, pp. 263–269, 1989.

[31] S. Chaudhuri, S. Chatterjee, N. Katz, M. Nelson, and M. Goldbaum, "Automatic detection of the optic nerve head in retinal images," in *Proceedings of the IEEE International Conference on Image Processing*, vol. 1, 1989.

[32] J. Cheng, J. Liu, Y. Xu, F. Yin, D. Wong, N.-M. Tan, D. Tao, C.-Y. Cheng, T. Aung, and T. Y. Wong, "Superpixel classification based optic disc and optic cup segmentation for glaucoma screening," *IEEE Transactions on Medical Imaging*, vol. 32, no. 6, pp. 1019–1032, 2013.

[33] T. Cootes and C. Taylor, "Statistical models of appearance for computer vision," University of Manchester, Tech. Rep., 2004.

[34] J. Daughman, "Complete discrete 2-d gabor transforms by neural networks for image analysis and compression," *IEEE Transactions on Acoustics, Speech and Signal Processing*, vol. 36, no. 7, pp. 1169–1179, 1988.

[35] H. Davis, S. Russell, E. Barriga, M. Abramoff, and P. Soliz, "Vision-based, real-time retinal image quality assessment," in *22nd IEEE International Symposium on Computer-Based Medical Systems*, 2009, pp. 1–6.

[36] J. a. M. P. Dias, C. M. Oliveira, and L. A. d. S. Cruz, "Retinal image quality assessment using generic image quality indicators," *Information Fusion*, vol. 13, no. 0, pp. 1–18, 2012.

[37] L. R. Dice, "Measures of the amount of ecologic association between species," *Ecology*, vol. 26, no. 3, pp. 297–302, 1945.

[38] M. V. Drake. (2011, April) The importance of corneal thickness. [Online]. Available: http://www.glaucoma.org

[39] S. Dua, U. R. Acharya, P. Chowriappa, and S. V. Sree, "Wavelet-based energy features for glaucomatous image classification," *IEEE Transactions on Information Technology in Biomedicine*, vol. 16, no. 1, pp. 80–87, 2012.

[40] R. O. Duda, P. E. Hart, and D. G. Stork, Eds., *Pattern Classification*. New York: Wiley-Interscience, 2000.

[41] J. R. Ehrlich and N. M. Radcliffe, "The role of clinical parapapillary atrophy evaluation in the diagnosis of open angle glaucoma," *Clinical Ophthalmology*, vol. 4, pp. 971–976, 2010.

[42] U. Fasih, A. Shaikh, N. Shaikh, M. Fehmi, A. R. Jafri, and A. Rahman, "Measurement error of visual field tests in glaucoma," *Pakistan Journal of Ophthalmology*, vol. 25, no. 3, pp. 145–151, 2009.

[43] Y. Fengshou, "Extraction of features from fundus images for glaucoma assessment," Master's thesis, National University of Singapore, 2011.

[44] M. Fischler and R. Bolles, "Random sample consensus: A paradigm for model fitting with applications to image analysis and automated cartography," *Communications of the ACM*, vol. 24, no. 6, pp. 381–395, 1981.

[45] M. Foracchia, E. Grisan, and A. Ruggeri, "Detection of optic disc in retinal images by means of a geometrical model of vessel structure," *IEEE Transactions on Medical Imaging*, vol. 23, no. 10, pp. 1189–1195, 2004.

[46] J. V. Forrester, A. D. Dick, and R. L. William, Eds., *The Eye, Basis sciences in practice 2nd edition.* Saunders Ltd, 2001.

[47] A. Frangi, W. J. Niessen, K. Vincken, and M. Viergever, "Multiscale vessel enhancement filtering," in *Proceedings 1st Medical Image Computing and Computer Assisted Intervention (MICCAI)*, 1998, pp. 130–137.

[48] J. A. d. l. Fuente-Arriagaa, E. M. Felipe-Riverón, and E. Garduño Calderónc, "Application of vascular bundle displacement in the optic disc for glaucoma detection using fundus images," *Computers in Biology and Medicine*, vol. 47, no. 1, pp. 27–35, 2014.

[49] F. Fumero, S. Alayon, J. Sanchez, J. Sigut, and M. Gonzalez-Hernandez, "Rim-one: An open retinal image database for optic nerve evaluation," in *Proceedings of the 24th International Symposium on Computer-Based Medical Systems (CBMS 2011), 2011.*, 2011.

[50] T. G.J., N. Reus, and H. Lemij, "Estimating the clinical usefulness of optic disc biometry for detecting glaucomatous change over time," *Eye*, vol. 20, no. 7, pp. 755–763, 2006.

[51] M. Goldbaum. (2000) Structured analysis of the retina (stare). [Online]. Available: http://www.ces.clemson.edu/~ahoover/stare/

[52] R. C. Gonzalez and R. E. Woods, Eds., *Digital Image Processing (3rd Edition)*. Prentice Hall, 2006.

[53] A. C. Gyuton and J. E. Hall, Eds., *Textbook of medical physiology 9th edition*. W.B. Saunders Company, 1996.

[54] F. t. Haar, "Automatic localization of the optic disc in digital colour images of the human retina," Master's thesis, Utrecht University, 2005.

[55] M. S. Haleem, L. Han, J. v. Hemert, and B. Li, "Automatic extraction of retinal features from colour retinal images for glaucoma diagnosis: A review," *Computerized Medical Imaging and Graphics*, vol. 37, no. 7-8, pp. 581–596, 2013.

[56] M. S. Haleem, L. Han, B. Li, A. Nisbet, J. v. Hemert, and M. Verhoek, "Automatic extraction of optic disc boundary for detecting retinal diseases," in *14th IASTED International Conference on Computer Graphics and Imaging (CGIM)*, 2013.

[57] R. Haralick and L. Shapiro, Eds., *Computer and Robot Vision*. Addison Wesley Longman Publishing Co., Inc, 1991.

[58] R. M. Haralick, K. Shanmugam, and I. Dinstein, "Textural features for image classification," *IEEE Transactions on Systems, Man and Cybernetics*, vol. 3, no. 6, pp. 610–621, 1973.

[59] N. Harizman, C. Oliveira, A. Chiang, C. Tello, M. Marmor, R. Ritch, and J. Liebmann, "The isnt rule and differentiation of normal from glaucomatous eyes," *Ophthalmology*, vol. 124, no. 11, pp. 1579–1583, 2006.

[60] A. Hoover and M. Goldbaum, "Locating the optic nerve in a retinal image using the fuzzy convergence of the blood vessels," *IEEE Transactions on Medical Imaging*, vol. 22, no. 8, pp. 951–958, 2003.

[61] C.-W. Hsu, C.-C. Chang, and C.-J. Lin, "A practical guide to support vector classifcation," 2010.

[62] L. Itti, C. Koch, and E. Niebur, "A model of saliency-based visual attention for rapid scene analysis," *IEEE Transactions on Pattern Analysis and Machine Intelligence*, vol. 20, no. 11, pp. 1254–1259, 1998.

[63] H. Jelinek and M. Cree, Eds., *Automated Image Detection of Retinal Pathology*. Taylor & Francis Group, 2010.

[64] J. Jonas, "Clinical implications of peripapillary atrophy in glaucoma," *Current Opinion in Ophthalmology*, vol. 16, no. 2, pp. 84–88, 2005.

[65] J. Jonas, W. Budde, and S. Jonas, "Ophthalmoscopic evaluation of optic nerve head," *Survey of Ophthalmology*, vol. 43, no. 4, pp. 293–320, 1999.

[66] J. Jonas, M. Fernández, and G. O. H. Naumann, "Glaucomatous parapapillary atrophy-occurrence and correlations," *Ophthalmology*, vol. 110, no. 2, pp. 214–222, 1992.

[67] J. Jonas, M. Fernández, and J. Stürmer, "Pattern of glaucomatous neuroretinal rim loss," *Ophthalmology*, vol. 100, no. 1, pp. 63–68, 1993.

[68] G. Joshi, J. Sivaswamy, and S. Krishnadas, "Optic disk and cup segmentation from monocular color retinal images for glaucoma assessment," *IEEE Transactions on Medical Imaging*, vol. 30, no. 6, pp. 1192–1205, 2011.

[69] G. Kande, P. Subbaiah, and T. Savithri, "Feature extraction in digital fundus images," *Medical Image Analysis*, vol. 29, no. 3, pp. 122–130, 2009.

[70] M. Kass, A. Witkin, and D. Terzopoulos, "Snakes: Active contour models," *International Journal of Computer Vision*, vol. 1, no. 4, pp. 321–331, 1987.

[71] S. Keerthi, S. Shevade, C. Bhattacharyya, and K. Murthy, "Improvements to Platt's SMO algorithm for SVM classifier design," National University of Singapore, Tech. Rep., 1998.

[72] S. K. Kim, H.-J. Kong, J.-M. Seo, B. J. Cho, K. H. Park, J. M. Hwang, D.-M. Kim, H. Chung, and H. C. Kim, "Segmentation of optic nerve head using warping and ransac," in *Proceedings of the 29th Annual International Conference of the IEEE EMBS*, 2007, pp. 900–903.

[73] T. Köhler, A. Budai, M. Kraus, J. Odstrcilik, G. Michelson, and J. Hornegger, "Automatic no-reference quality assessment for retinal fundus images using vessel segmentation," in *26th IEEE Internatioal Symposium on Computer-Based Medical Systems 2013*, 2013.

[74] T. Kohler, A. Budai, M. Kraus, J. Odstrcilik, G. Michelson, and J. Hornegger, "Automatic no-reference quality assessment for retinal fundus images using vessel segmentation," in *IEEE Internatioal Symposium on Computer-Based Medical Systems 2013*, 2013, pp. 95–100.

[75] C. Kose and C. Ikibas, "Statistical techniques for detection of optic disc and macula and parameters measurement in retinal fundus images," *Journal of Medical and Biological Engineering*, vol. 31, no. 6, pp. 395–404, 2010.

[76] M. Lalonde, M. Beaulieu, and L. Gagnon, "Fast and robust optic disc detection using pyramidal decomposition and hausdorff-based template matching," *IEEE Transactions on Medical Imaging*, vol. 20, no. 11, pp. 1193–1200, 2001.

[77] B. Lee, D. Wong, N. Tan, Z. Zhang, J. Lim, H. Li, F. Yin, J. Liu, W. Huang, S. Saw, L. Tong, and T. Wong, "Fusion of pixel and texture features to detect pathological myopia," in *5th IEEE Conference on Industrial Electronics and Applications (ICIEA)*, 2010, pp. 2039–2042.

[78] B. Li and S. T. Action, "Active contour external force using vector field convolution for image segmentation," *IEEE Transactions on Image Processing*, vol. 16, no. 8, pp. 2096–2106, 2007.

[79] H. Li and O. Chutatape, "Automatic location of optic disk in retinal images," in *Proceedings of International Conference on Image Processing*, 2001, pp. 837–840.

[80] ——, "Boundary detection of optic disk by a modified asm method," *Pattern Recognition*, vol. 36, no. 9, pp. 2093–2104, 2003.

[81] T. Lindeberg, "edge detection and ridge detection with automatic scale selection," *International Journal of Computer Vision*, vol. 30, pp. 117–156, 1998.

[82] H. Liu and H. Motoda, Eds., *Feature Selection for Knowledge Discovery and Data Mining*. Kluwer Academic Publishers Norwell, MA, USA, 1998.

[83] J. Liu, J. H. Lim, W. K. Wong, H. Li, and T. Y. Wong, "Automatic cup to disc ratio measurement system," Patent 20 110 091 083, 04 21, 2011. [Online]. Available: http://www.faqs.org/patents/app/20110091083

[84] J. Liu, Z. Zhang, D. W. K. Wong, Y. Xu, F. Yin, J. Cheng, N. M. Tan, C. K. Kwoh, D. Xu, Y. C. Tham, T. Aung, and T. Y. Wong, "Automatic glaucoma diagnosis through medical imaging informatics," *Journal of American Medical Information Association*, vol. 20, pp. 1021–2017, 2013.

[85] J. Lowell, A. Hunter, D. Steel, A. Basu, R. Ryder, E. Fletcher, and L. Kennedy, "Optic nerve head segmentation," *IEEE Transactions on Biomedical Engineering*, vol. 23, no. 2, pp. 256–264, 2004.

[86] C.-K. Lu, T. B. Tang, A. Laude, I. J. Deary, B. Dhillon, and A. F. Murray, "Quantification of parapapillary atrophy and optic disc," *Multidisciplinary Ophthalmic Imaging*, vol. 52, no. 7, pp. 4671–4677, 2011.

[87] C. A. Lupas, D. Tegolo, and E. Trucco, "FABC: Retinal vessel segmentation using adaboost," *IEEE Transactions on Information Technology in Biomedicine*, vol. 14, no. 5, pp. 1267–1274, 2010.

[88] A. Mahfouz and A. S. Fahmy, "Fast localization of the optic disc using projection of image features," *IEEE Transactions on Image Processing*, vol. 19, no. 12, pp. 3285–3289, 2010.

[89] J. Meier, R. Bock, G. Michelson, L. Nyúl, and J. Hornegger, "Effects of preprocessing eye fundus images on appearance based glaucoma classification," in *Proceedings of the 12th international conference on Computer analysis of images and patterns*, vol. 4673, 2007, pp. 165–172.

[90] F. Mendels, C. Heneghan, P. Harper, R. Reilly, and J. Thiran, "Extraction of the optic disk boundary in digital fundus images," in *Proceedings of the First BMES / EMBS Conference*, 1999, p. 1139.

[91] F. Mendels, C. Heneghan, and J. Thiran, "Identification of the optic disk boundary in retinal images using active contours," in *Proceedings of Irish Machine Vision and Image Processing Conference (IMVIP)*, 1999, pp. 103–115.

[92] G. Michelson, J. Hornegger, S. Wärntges, and B. Lausen, "The papilla as screening parameter for early diagnosis of glaucoma," *Deutsches Arzteblatt International*, vol. 105, no. 34-35, pp. 583–589, 2008.

[93] A. Mitiche and I. B. Ayed, Eds., *Variational and Level Set Methods in Image Segmentation*. Springer, 2011.

[94] M. R. K. Mookiah, U. R. Acharya, C. K. Chua, L. C. Min, E. Y. K. Ng, M. M. Mushrif, and A. Laude, "Automated detection of optic disk in retinal fundus images using intuitionistic fuzzy histon segmentation," *Journal of Engineering in Medicine*, vol. 227, no. 1, pp. 37–49, 2012.

[95] A. Moore, S. Prince, J. Warrell, U. Mohammed, and G. Jones, "Superpixel lattices," in *Computer Vision and Pattern Recognition*, 2008, pp. 1–8.

[96] H. E. Moss, G. Treadwell, J. Wanek, S. DeLeon, and M. Shahidi, "Retinal vessel diameter assessment in papilledema by semi automated analysis of slo images: Feasibility and reliability," *Investigative Ophthalmology and Visual Science (IOVS)*, vol. 55, no. 4, pp. 2049–2054, 2014.

[97] C. Muramatsu, T. Nakagawa, A. Sawada, Y. Hatanaka, T. Hara, T. Yamamoto, and H. Fujita, "Automated segmentation of optic disc region on retinal fundus photographs: Comparison of contour modeling and pixel classification methods." *IEEE Transactions on Medical Imaging*, vol. 101, no. 1, pp. 23–32, 2011.

[98] C. Muramatsu, Y. Hatanaka, A. Sawada, T. Yamamoto, and H. Fujita, "Computerized detection of peripapillary chorioretinal atrophy by texture analysis," in *Conference Proceedings IEEE Engineering in Medicine and Biology Society*, 2011, pp. 5947–5950.

[99] J. Nayak, R. Acharya, P. Bhat, N. Shetty, and T.-C. Lim, "Automated diagnosis of glaucoma using digital fundus images," *Journal of Medical Systems*, vol. 33, no. 5, pp. 337–346, 2009.

[100] A. Osareh, M. Mirmehdi, B. Thomas, and R. Markham, "Comparison of colour spaces for optic disc localisation in retinal images," in *Proceedings of the 16th International Conference on Pattern Recognition*, 2002, pp. 743–746.

[101] A. Osareh, M. Mirmehdi, B. T. Thomas, and R. Markham, "Classification and localisation of diabetic-related eye disease," in *Proceedings of 7th European Conference on Computer Vision-Part IV*, vol. 2, 2002, pp. 1625–1629.

[102] J. Park, N. T. Kien, and G. Lee, "Optic disc detection in retinal images using tensor voting and adaptive mean-shift," in *IEEE International Conference on Intelligent Computer Communication and Processing*, 2007, pp. 237–241.

[103] N. Patton, T. M. Aslam, T. MacGillivray, I. J. Deary, B. Dhillon, R. H. Eikelboom, K. Yogesan, and I. Constabl, "Retinal image analysis: Concepts, applications and potential," *Progress in Retinal and Eye Research*, vol. 25, no. 1, p. 99 127, 2005.

[104] E. Pellegrini, G. Robertson, E. Trucco, T. J. MacGillivray, C. Lupascu, J. van Hemert, M. C. Williams, D. E. Newby, E. J. van Beek, and G. Houston, "Blood vessel segmentation and width estimation in ultra-wide field scanning laser ophthalmoscopy," *Biomedical Optics Express*, vol. 5, no. 12, pp. 4329–4337, 2014.

[105] R. Pires, H. Jelinek, J. Wainer, and A. Rocha, "Retinal image quality analysis for automatic diabetic retinopathy detection," in *25th SIBGRAPI Conference on Graphics, Patterns and Images (SIBGRAPI)*, 2012, pp. 229–236.

[106] L. Ricco, "Lipschitz functions," Tech. Rep., 2004.

[107] M. Rizon, H. Yazid, P. Saad, A. Y. M. Shakaff, and A. R. Saad, "Object detection using circular hough transform," *American Journal of Applied Sciences*, vol. 2, no. 12, 2005.

[108] G. Robertson, E. Pellegrini, C. Gray, E. Trucco, and T. J. MacGillivray, "Investigating post processing of scanning laser ophthalmoscope images for unsupervised retinal blood vessel detection," in *International Symposium on Computer-Based Medical Systems*, 2013, pp. 441–444.

[109] J. B. T. M. Roerdink and A. Meijster, "The watershed transform: Definitions, algorithms and parallelization strategies," *Fundamenta Informaticae*, vol. 41, pp. 187–228, 2001.

[110] J. Roodhooft, "Leading causes of blindness worldwide," *Bull Soc Belge Ophtalmol*, vol. 283, pp. 19–25, 2002.

[111] S.-M. Saw, A. Shankar, S.-B. Tan, H. Taylor, D. T. H. Tan, R. A. Stone, and T.-Y. Wong, "A cohort study of incident myopia in singaporean children," *Investigative Ophthalmology and Visual Science*, vol. 47, no. 5, pp. 1839–1844, 2006.

[112] S. Sekhar, W. Al-Nuaimy, and A. Nandi, "Automated localisation of retinal optic disk using hough transform," in *Proceedings of 5th IEEE International Symposium on Biomedical Imaging: From Nano to Macro*, 2008, pp. 1577 – 1580.

[113] A. J. Serrano, E. Soria, J. D. Martin, R. Magdalena, and J. Gomez, "Feature selection using roc curves on classification problems," in *The International Joint Conference on Neural Networks (IJCNN)*, 2010, pp. 1–6.

[114] C. Sinthanayothin, J. Boyce, H. Cook, and T. Williamson, "Automated localisation of the optic disc, fovea, and retinal blood vessels from digital colour fundus images," *British Journal of Ophthalmology*, vol. 83, no. 8, pp. 902–910, 1999.

[115] J. Sivaswamy, S. Krishnadas, G. D. Joshi, M. J. Ujjwal, and S. Tabish, "Drishti-gs: Retinal image dataset for optic nerve head(onh) segmentation," in *IEEE 11th International Symposium on Biomedical Imaging (ISBI), 2014.*, 2014.

[116] A. Smola and S. Vishwanathan, *Introduction to Machine Learning.* Cambridge University Press, 2008.

[117] P. Spry, C. Johnson, A. McKendrick, and A. Turpin, "Measurement error of visual field tests in glaucoma," *British Journal of Ophthalmology*, vol. 87, pp. 107–112, 2003.

[118] J. Staal, M. Abramoff, M. Niemeijer, M. Viergever, and B. v. Ginneken, "Ridge based vessel segmentation in color images of the retina," *IEEE Transactions on Medical Imaging*, vol. 23, no. 4, pp. 501–509, 2004.

[119] M. Stegmann and D. Gomez, "A brief introduction to statistical shape analysis," Tech. Rep., 2002.

[120] F. M. Sukno, S. Ordas, C. Butakoff, S. Cruz, and A. F. Frangi, "Active shape models with invariant optimal features: Application to facial analysis," *IEEE Transactions on Pattern Analysis and Machine Intelligence*, vol. 29, no. 7, pp. 1105–1117, 2007.

[121] S. G. Sun and D. M. Kwak, "Automatic detection of targets using center-surround difference and local thresholding," *Journal of Multimedia*, vol. 1, no. 1, pp. 16–23, 2006.

[122] K. Takayamaa, S. Ootoa, M. Hangaia, N. Ueda-Arakawaa, S. Yoshidaa, T. Akagia, H. O. Ikedaa, A. Nonakaa, M. Hanebuchib, T. Inouec, and N. Yoshimuraa, "High resolution imaging of retinal nerve fiber bundles in glaucoma using adaptive optics scanning laser ophthalmoscopy," *Americal Journal of Ophthalmology*, vol. 155, no. 5, pp. 870–881, 2013.

[123] N. Tan, J. Liu, W. D.W.K., J. Lim, Z. Zhang, S. Lu, H. Li, S. Saw, L. Tong, and T. Wong, "Automatic detection of pathological myopia using variational level set," in *31st Annual International Conference of the IEEE Engineering in Medicine and Biology Society*, 2009, pp. 3609–3612.

[124] L. Tang, M. Niemeijer, J. Reinhardt, and M. Garvin, "Splat feature classification with application to retinal hemorrhage detection in fundus images," *IEEE Transactions on Medical Imaging*, vol. 32, no. 2, pp. 364–375, 2013.

[125] C. C. Teng, C. G. V. D. Moraes, v. S. Prata, C. Tello, R. Ritch, and J. M. Liebmann, "β-zone parapapillary atrophy and the velocity of glaucoma progression," *Ophthalmology*, vol. 117, no. 5, pp. 909–915, 2010.

[126] B. van Ginneken, A. F. Frangi, J. J. Staal, B. M. t. H. Romeny, and M. A. Viergever, "Active shape model segmentation with optimal features," *IEEE Transactions on Medical Imaging*, vol. 21, no. 8, pp. 924–933, 2002.

[127] M. J. M. Vasconcelos and J. M. R. S. Tavares, "Methods to automatically build point distribution models for objects like hand palms and faces represented in images," *Computer Modeling in Engineering and Sciences*, vol. 36, no. 3, pp. 213–241, 2008.

[128] O. Veksler, Y. Boykov, and P. Mehrani, "Superpixels and supervoxels in an energy optimization framework," in *11th European Conference on Computer Vision*, 2010, pp. 211–224.

[129] L. Vincent and P. Soille, "Watersheds in digital spaces: an efficient algorithm based on immersion simulations," *IEEE Transactions on Pattern Analysis and Machine Learning*, vol. 13, no. 6, pp. 583–598, 1991.

[130] N. J. Wade, "Image, eye, and retina (invited review)," *Journal of the Optical Society of America. A, Optics, image science, and vision*, vol. 24, no. 5, pp. 1229–1249, 2007.

[131] T. Walter and J.-C. Klein, "Segmentation of color fundus images of the human retina: Detection of the optic disc and the vascular tree using morphological techniques," in *Proceedings of the Second International Symposium on Medical Data Analysis*, 2001, pp. 282–287.

[132] R. N. Weinreb and P. T. Khaw, "Primary open-angle glaucoma," *The Lancet*, vol. 363, pp. 1711–1720, 2004.

[133] G. Williams, I. Scott, J. Haller, A. Maquire, D. Marcus, and H. McDonald, "Single-field fundus photography for diabetic retinopathy screening: a report by the American Academy of Ophthalmology." *Ophthamology*, vol. 111, pp. 1055–1062, 2004.

[134] D. Wong, J. Liu, J. Lim, X. Jia, F. Yin, H. Li, and T. Wong, "Level-set based automatic cup-to-disc ratio determination using retinal fundus images in argali." in *30th Annual International Conference of the IEEE Engineering in Medicine and Biology Society*, 2008, pp. 2266–2269.

[135] ——, "Automated detection of kinks from blood vessels for optic cup segmentation in retinal images," in *Proceedings of the SPIE Medical Imaging*, 2009, pp. 1–8.

[136] C. Xu and J. Prince, "Snakes, shapes, and gradient vector flow," *IEEE Transactions on Image Processing*, vol. 7, no. 3, pp. 359–369, 1998.

[137] J. Xu, O. Chutatape, E. Sung, C. Zheng, and P. C. T. Kuan, "Optic disk feature extraction via modied deformable model technique for glaucoma analysis," *Pattern Recognition*, vol. 40, no. 7, pp. 2063–2076, 2005.

[138] T. Xua, M. Mandal, R. Long, I. Cheng, and A. Basu, "An edge-region force guided active shape approach for automatic lung field detection in chest radiographs," *Computerized Medical Imaging and Graphics*, vol. 36, no. 6, p. 452463, 2012.

[139] H. Ying, M. Zhang, and J.-C. Liu, "Fractal-based automatic localization and segmentation of optic disc in retinal images," in *Proceedings of the 29th Annual International Conference of the IEEE EMBS*, 2007, pp. 4139–4141.

[140] A. A.-H. A.-R. Youssif, A. Z. Ghalwash, and A. A. S. A.-R. Ghoneim, "Optic disc detection from normalized digital fundus images by means of a vessels direction matched filter," *IEEE Transactions on Medical Imaging*, vol. 27, no. 1, pp. 11–18, 2008.

[141] H. Yu, S. Barriga, C. Agurto, S. Echegaray, M. Pattichis, G. Zamora, W. Bauman, and P. Soliz, "Fast localization of optic disc and fovea in retinal images for eye disease screening," in *Proceedings of SPIE Conference on Medical Imaging 2011: Computer-Aided Diagnosis*, 2011.

[142] H. Yu, C. Agurto, S. Barriga, S. C. Nemeth, P. Soliz, and G. Zamora, "Automated image quality evaluation of retinal fundus photographs in diabetic retinopathy screening," in *IEEE Southwest Symposium on Image Analysis and Interpretation (SSIAI)*, 2012, pp. 125–128.

[143] X. Yuan, B. Giritharan, and J. Oh, "Gradient vector flow driven active shape for image segmentation," in *IEEE International Conference on Multimedia and Expo*, 2007, pp. 2058 – 2061.

[144] L. G. Zelinsky, "A fast radial symmetry for detecting points of interest." *IEEE Transactions of Pattern Analysis and Machine Intelligence*, vol. 25, pp. 959–973, 2003.

[145] Z. Zhang, F. Yin, J. Liu, W. Wong, N. Tan, B. Lee, J. Cheng, and T. Wong, "Origa(-light): an online retinal fundus image database for glaucoma analysis and research," in *IEEE Annual International Conference of Engineering in Medicine and Biology Society (EMBC)*, 2010, pp. 3065 – 3068.

[146] W. Zhao, R. Chellappa, P. Phillips, and A. Rosenfield, "Face recognition: A literature survey," *ACM Computyer Survey*, vol. 35, no. 4, pp. 399–458, 2003.

[147] X. Zhu, R. M. Rangayyan, and A. L. Ells, "Detection of the optic nerve head in fundus images of the retina using the hough transform for circles," *Journal of Digital Imaging*, vol. 23, no. 3, pp. 332–341, 2010.

[148] K. Zutis, E. Trucco, J. Hubschmant, D. Reed, S. Shah, and J. van Hemert, "Towards automatic detection of abnormal retinal capillaries in ultra-widefield-of-view retinal angiographic exams," in *IEEE EMBS Engineering in Medicine and Biology Society*, 2013, pp. 7372–7375.